BILINGUAL PUBLISHING CO.
Pioneer of Global Academics Since 1984

Journal of Environmental & Earth Sciences

Volume 4 • Issue 2 • October 2022 ISSN 2661-3190(Online)

BILINGUAL PUBLISHING CO.
Pioneer of Global Academics Since 1984

Volume 4 Issue 2 • October 2022 • ISSN 2661-3190 (Online)

Journal of Environmental & Earth Sciences

BILINGUAL PUBLISHING CO.
Pioneer of Global Academics Since 1984

BILINGUAL PUBLISHING CO.
Pioneer of Global Academics Since 1984

Volume 4 | Issue 2 | October 2022 | Page1-64
Journal of Environmental & Earth Sciences

Contents

Articles

BILINGUAL PUBLISHING CO.
Pioneer of Global Academics Since 1984

Journal of Environmental & Earth Sciences
https://ojs.bilpublishing.com/index.php/jees

ARTICLE

Quantum Biophysics of the Atmosphere: Asymmetric Wavelets of the Average Annual Air Temperature of Irkutsk for 1820-2019

Mazurkin Peter Matveevich*

Volga State University of Technology, Yoshkar-Ola, Russia

ARTICLE INFO

Article history
Received: 2 April 2022
Revised: 27 May 2022
Accepted: 30 May 2022
Published Online: 16 June 2022

Keywords:
Average annual temperature
1820-2019
Wavelets
Forecast up to 2220

ABSTRACT

The regularities of the dynamics of the average annual temperature of Irkutsk from 1820 to 2019 were revealed. It is proposed to use the sum of temperatures. However, this indicator requires the continuity of the dynamic series, so for Irkutsk the sum of temperatures could be accepted only from 1873. The first three terms of the general wavelet model gave a very high correlation coefficient of 0.9996. The second indicator is a moving average, calculated as the ratio of the sum of temperatures to the current time. Here the first three wavelets gave a correlation coefficient of 0.9962. In the dynamics of the average annual temperature from 1820 to 2019, 86 wavelets were obtained, of which 47 affect the future. The temperature has a high quantum certainty, and the change in the average annual temperature of Irkutsk is obtained up to a measurement error of 0.05 °C, and the identification process occurs as a full wavelet analysis. The basis of the forecast in 200 years makes it possible to replace the non-linear two-term trend with an oscillatory perturbation. With an increase in the number of terms in the model, the ordinate of the average annual temperature increases: For three terms, the temperature interval is from –2.95 °C to 2.61 °C; for 12 members from –4.06 °C to 4.02 °C; for the forecast for 47 members for 2020-2220, from –4.62 °C to 4.40 °C.

1. Introduction

In the 21st century, global average temperatures are very likely, according to studies by Friedrich T. and others [1], to exceed the maximum levels recovered over the past 784,000 years. Based on temperature data from eight glacial cycles, the results provide an independent validation of current CMIP5 warming projections.

However, if the temperature decreased during the ice ages, then why should the forecasts in different regions of the Earth be the same?

An analysis of the transient 15-year trends presented in "Causes of variability in long-term warming" [2] shows that the rate of warming slowed down between 1999 and 2014. Another article [3] states that global temperature records from 1901 to 2008 refer to natural fluctuations: sometimes they cause warming, sometimes cooling. As noted in the materials "The Modern Temperature Trend" [4], it

*Corresponding Author:
Mazurkin Peter Matveevich,
Volga State University of Technology, Yoshkar-Ola, Russia;
Email: kaf_po@mail.ru

DOI: https://doi.org/10.30564/jees.v4i2.4586

became clear that the cooling effect (mainly in the Northern Hemisphere) was temporary. When the rise continued into the 21st century, penetrating into the depths of the ocean (oceanologists admitted their mistakes and therefore everything is not so obvious in recent years), it signaled a profound change in the climate system. Nothing like it has happened for centuries. The article [5] considers the factors that could influence the slowdowns and the natural causes for each of them.

For example, in an article by Swain D.L. and others [6] data from the California drought in 2012-2015 show that the frequency of the harshest and hottest years has increased, and they are not associated with wet years.

The earth warmed at an unprecedented rate during the 1980s and 1990s, and the rapidity of the warming coincided with a 65-year cycle. However, Wu Z. and others argue [7] that the observed trends in global average surface temperature up to one-third of the warming at the end of the 20th century could be due to natural temperature variability.

The intensity of the heat island of Moscow, as noted in the article [8], has increased, moreover, despite the pause in global warming. It was found that the island can be traced vertically up to a height of 2 km. In summer, the lower part of the heat island represents dryness, while the upper part of the heat island corresponds to humidity. In winter, moisture is released in the lower part of the heat island.

The unprecedented intensification of extreme weather in recent years is motivating research for understanding, as pointed out by Zappalà et al. [9], long-term climate change. But this article uses averaged data, for example, over periods of 10 years. Many studies use converted measurement series. Mathematical methods are limited to linear trends and strong data averaging. As a result, the so-called identification of the climate pattern occurs.

For example, the article [10] shows the dynamics of air temperature on the land surface in the world since 1880, the so-called "linear objective estimate" is given, which immediately casts serious doubt on the interpretation of the results. From the point of view of climate behavior quanta, in the article [10], "a new analysis of the average annual global air temperature on the Earth's surface since 1880 was carried out". However, again, the deepening in the understanding of processes does not go further than linear models.

The comparison of the surface air temperature variability in three coupled integrations of the "ocean-atmosphere" model over 1000 years [11] was also performed using linear trends. But land surface temperature measurements are the longest and most reliable.

However, land surface temperature measurements are known to be the longest and most reliable. Gradually comes the understanding of the invariability of dynamic series according to the primary measurement data and the ban on all sorts of groupings in favor of the linearization method. Gradually comes the realization of the need for wave equations to identify directly primary data without tricks by their groupings and other simplifications.

As a result, the time series of global or regional surface air temperature, according to the conclusions of Li G.X. and Zhou G. [12] are of fundamental importance for climate change research. For example, in the article [13], monthly and annual temperature differences and their changes on the Tibetan plateau and its environs for 1963-2015 were considered.

2. The Concept of Quantum Biophysics of the Atmosphere

The concept of heat movement on the Earth is described in the article [14]. According to A. Chernokulsky, our Sun heats the Earth unevenly: The equator gets more, the poles get less. This temperature gradient is one of the main forces that drive the ocean and atmosphere. In the tropics, the climate system of our planet receives energy, and in temperate and polar latitudes it gives it away. The main transfer of heat from the equator to the pole is carried out in the atmosphere. The ocean is the slow component of the climate system. It does not respond as sharply to external influences as the atmosphere. In heat transfer, it acts as a battery: Taking heat from the Sun and heating up, the ocean then shares it with the air.

But with the bifurcations of the atmosphere and climate, many natural landscapes do not change for millennia, for example, as shown in our articles [15,16], the grass cover of the steppes. Grass appeared on land about 100 million years ago. Maybe she, as the strongest type of vegetation, has such values of the parameters of oscillatory adaptation that she will survive in any climatic changes in the future. What are the limits of the life of this grass cover? For example, the Eurasian steppe 8000 km long from Hungary to Inner Mongolia China?

To answer such questions, it is necessary not only to develop weather forecasts, but also to identify the behavioral quanta of the surface air layer at different points on the Earth according to weather stations, but the time series must be at least 175 years old. Then, for example, for the Eurasian steppe, there will be differences (distinguishing features) in temperature dynamics and opportunities for the synthesis of quantum biophysics of soil and parameters of the surface air layer at various points in the range of steppe grass.

While climatology is trying to develop independently.

The choice of informative criteria and objective classification methods remains an urgent task of climatology. For example, the article [17] studies temperature changes

according to the data of 818 stations in the Northern Hemisphere for 1955-2011. The results of climatic clustering for different time periods corresponding to the main trends in global temperature changes are given.

Summer hot temperatures affect health, the economy (agriculture, energy and transport) and ecosystems in many ways. In Western Europe, the summers of 2003 and 2015 were exceptionally warm. The events of the last decades [18] were associated with the anticyclonic circulation of the atmosphere and the deficit of spring precipitation in Southern Europe. Such results were obtained for the second half of the 20th century.

The role and mechanisms of climatic impact on plant productivity are multifaceted. Research by Babushkina and others [19] found that among the meteorological variables, the humidity index had the maximum effect on plants.

Climate, such as air temperature and rainfall, varies greatly between urban core and peripheral areas [20], resulting in different growing conditions for trees.

The measurement results showed that soil moisture is decreasing and CO_2 emissions from the soil are increasing. It is known from the article [21] that this will reduce the sensitivity to the soil respiration temperature in the ecosystem of alpine meadows in the area of permafrost in the Tibetan Plateau, especially for short and medium periods.

In the article [22] Zharkova V. proved that solar activity has a strong influence on the climate dynamics on Earth.

The authors of the article [23] concluded: "There is reason to believe that global warming is now almost over and we should expect a slow decrease in the period 2014-2040, primarily in the Northern Hemisphere over land".

Therefore, when modeling for heuristic identification of the essence of infinite-dimensional wavelet signals, we used various cycles of solar activity. However, the parameters of the atmosphere are highly dynamic due to synoptic phenomena and processes, so the cycles of solar activity become, as it were, just starting, after a short time, fluctuations in temperature and other meteorological parameters receive variables, as a rule, increasing, amplitudes and periods.

The purpose of the study is to identify asymmetric wavelet signals of the dynamics of the sum of temperatures and the moving average annual temperature from 1873 to 2019, as well as a set of infinite-dimensional and finite-dimensional wavelets for predicting up to 2220 on the dynamic series of the average annual temperature of the surface air layer, using the identification method [24-26] in Irkutsk from 1820 to 2019.

3. Initial Data of the Irkutsk Weather Station

For the possibility of modeling the dynamics of the average annual temperature by a set of wave equations, the initial time is taken for 1820. For modeling the dynamics, a series of average annual temperatures are taken with discontinuities (lack of data for some years). Gaps in the time series according to the data do not give an accurate division of the dynamics into a set of wavelets (quanta of behavior).

Figure 1 shows the landscape along the meridian from the Arctic Ocean to Irkutsk (URL: https://cs11.pikabu.ru/post_img/big/2020/11/27/4/1606456328111940732.jpg).

The location of Irkutsk is conventionally shown as a white square. From the side of the Arctic Ocean, cold winds pass unhindered to the city. And the mountain range interferes with warm winds from the south. Therefore, Irkutsk is located in a unique place in Asia.

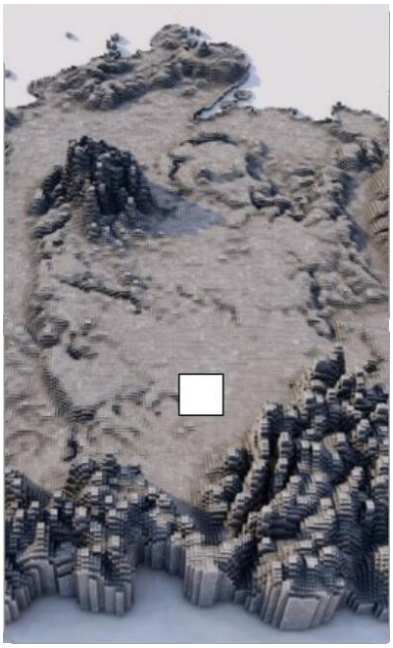

Figure 1. Landscape of Irkutsk.

To calculate the sum of temperatures and the moving average over years of temperature, breaks in the time series are not allowed, therefore, for these parameters, the series starts from 1873. For some years (1820, 1832, 1841, 1844-1857, 1860, 1861, 1863, 1867-1872) there are also no data on average annual measurements. For the missing value of the average annual temperature for 1881, interpolation was adopted, then the calculated average annual temperature is ((–1.3) (1880) + (–1) (1882)) / 2 = –1.1 °C.

Irkutsk is a complex object of climatic geomorphology.

The article [27] analyzes the changes in the extremeness of the winter thermal regime in the Cis-Baikal region. An estimate of the temporal variability in the frequency of daily minimum air temperatures below –30 °C, –35 °C, –40 °C, –45 °C and –50 °C for the period 1943-2012 is given. Winter conditions become thermally milder over

the years, although periods with abnormally low temperatures are not ruled out.

On the basis of data on the concentrations of pollutants indexed at the posts of observation of atmospheric pollution, the dynamics of their change in the period from 2000 to 2012 are presented [28]. Now the main weather station is located inside Irkutsk, so the influence of the heat island from the growing city, apparently, increases over the years. Therefore, the temperature forecast for Irkutsk becomes conditional, since it is necessary to take into account the growing influence of the urban environment on the heat island.

The article [29] presents the materials of a continuous study of the chemical composition of atmospheric aerosols and precipitation (rain, snow) at the Irkutsk monitoring station, which is part of the Southeast Asia atmospheric fallout monitoring network (EANET) for the period 2000-2012. In the last five years, there has been an increase in the mineralization of atmospheric precipitation, especially in winter. The number of gaseous impurities in the air of the city increased against the background of a low total content of ions in aerosols.

The series of the surface average annual temperature for Irkutsk were taken from the website http://www.pogodaiklimat.ru/history.php?id=ru (Accessed 07/07/2020).

Table 1 gives a fragment of the data array of the average annual temperature of the surface air layer at a height of 2 m according to measurements at the meteorological station in Irkutsk.

Table 1. Average annual air temperatures (°C) of Irkutsk for 1820-2019.

Year	Temperature		Sum of temperatures		Moving average	
	Time τ	t	Time τ_1	$\sum t$	Time τ_2	$\tilde{t}$
1820	0	-	-	-	-	-
1821	1	0.6	-	-	-	-
1822	2	0.3	-	-	-	-
…	…	…	…	…	…	…
1873	53	–0.7	0	–0.7	1	–0.70
1874	54	0.2	1	–0.5	2	–0.25
1875	55	–1.1	2	–1.6	3	–0.53
…	…	…	…	…	…	…
2017	197	2.6	144	–57.4	145	–0.40
2018	198	1.3	145	–56.1	146	–0.38
2019	199	2.1	146	–54.0	147	–0.37

The year 1820 was taken as the beginning of the countdown of time (years) according to the dynamic series of temperature. Then, 200 years have passed from the beginning of 1820 to the end of 2019, so the indicative forecast can be made for the forecast horizon equal to the forecast base, that is, until 2020 + 200 = 2220. For the sum of temperatures and the moving average temperature, 1873 is taken as the beginning of the series. , therefore, these parameters are needed only to understand the picture of the dynamics of the average annual temperature from 1820 to 2220.

Table 1 contains 2019 – 1819 = 200 years in total, and for the sum of temperatures and the moving average annual temperature 2019 – 1872 = 147 years.

4. Generalized Asymmetric Wavelet and Sum of Quantums of Behavior

Success in physics is largely determined by the use of mathematics. Physicists often create the necessary mathematical apparatus themselves [30].

We have developed a method for identifying successively a set of regularities in the form of asymmetric wavelet signals. This set is essentially an algebraic equation according to René Descartes.

Oscillations (asymmetric wavelet signals) are generally written by the wave formula [24-26] of the form.

$$y = \sum_{i=1}^{m} y_i,\ y_i = A_i \cos(\pi x / p_i - a_{8i}),$$

$$A_i = a_{1i} x^{a_{2i}} \exp(-a_{3i} x^{a_{4i}}),\ p_i = a_{5i} + a_{6i} x^{a_{7i}}, \quad (1)$$

where y is the indicator (dependent factor), i is the number of the component of the model (1), m is the number of members in the model (1), x is the explanatory variable (influencing factor), $a_1 ... a_8$ are the parameters of the model (1) that take numerical values during structural and parametric identification in program environment CurveExpert-1.40 (URL: http://www.curveexpert.net/) according to statistical data, A_i is the amplitude (half) of the wavelet (axis y), p_i is the half-period of oscillation (axis x).

This article refers to quantum meteorology [26], which makes it possible to isolate the quanta of the behavior of the surface layer of the atmosphere in the form of asymmetric wavelets (1) for three types of temperature in Irkutsk. According to these selected quanta of the behavior of the average annual temperature, the signals are unknown, therefore, each wavelet needs to be analyzed by specialists using heuristic methods to find out the reasons for the occurrence of fluctuations. This will reveal the mechanisms of oscillatory climate adaptation.

5. Research Results

5.1 Dynamics of the Sum of Temperatures in Irkutsk Since 1873

Temperature is a physical quantity that is a measure of

the average kinetic energy of the translational motion of molecules, in our case, air molecules in the surface layer of air at a height of 2 m above the land surface in Irkutsk.

Over time, energy accumulates, so we can estimate this accumulation by the sum of temperatures according to Table 1 using the calculation formula:

$$\sum t_{\tau_1} = \sum_{\tau_1=0}^{\tau_1=146} t_{\tau_1} \quad (2)$$

Then the sum of temperatures will show an aligned series.

Table 2 shows the parameters of the general model (1) and the adequacy in terms of the correlation coefficient, and Figure 2 shows the graphs of the components.

After the five components of the model (1), the identification can be continued. However, over time, the relative error of the formula in the form of a sum of five terms in Table 2 decreases sharply for the interval 2009-2019 and becomes less than 1.17%.

Table 2. Parameters of the sum of average annual temperatures in Irkutsk for 1873-2019.

i	**Asymmetric wavelet** $y_i = a_{1i}x^{a_{2i}}\exp(-a_{3i}x^{a_{4i}})\cos(\pi x/(a_{5i}+a_{6i}x^{a_{7i}})-a_{8i})$								**Coef. correl. r**
	Amplitude (half) oscillation				**Half cycle oscillation**			**Shift**	
	a_{1i}	a_{2i}	a_{3i}	a_{4i}	a_{5i}	a_{6i}	a_{7i}	a_{8i}	
1	41.28078	0	0.00044829	1	0	0	0	0	
2	–0.011685	2.35352	0.00061386	1.68579	0	0	0	0	0.9996
3	–335.5300	0	0.066596	0.92114	813.6061	–435.5187	0.11863	1.44577	
4	–0.050041	1.67099	0.80452	0.38283	12.28539	–0.0010573	1.63220	–0.77318	0.7439
5	0.0019846	2.00250	0.27280	0.57517	29.74132	–0.035096	1.16942	1.25137	0.4434

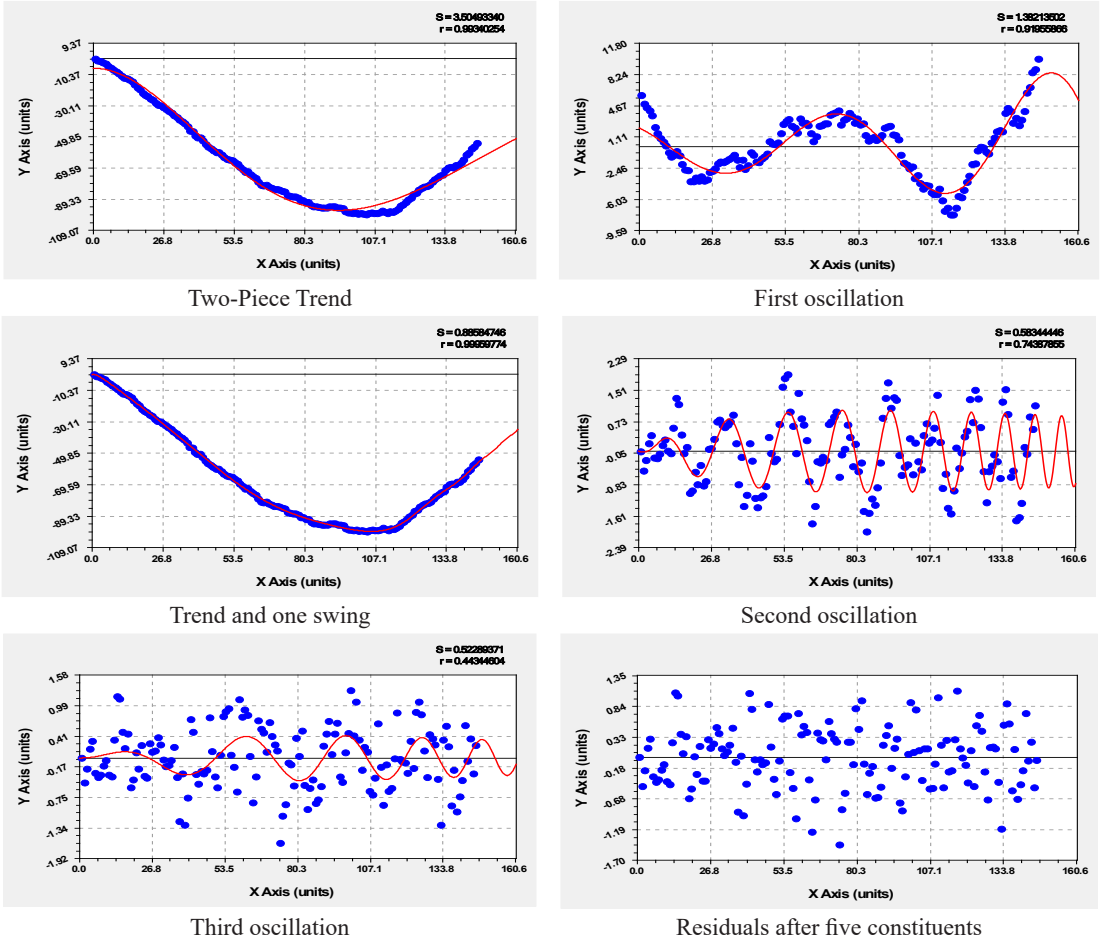

Two-Piece Trend | First oscillation

Trend and one swing | Second oscillation

Third oscillation | Residuals after five constituents

Figure 2. Graphs of changes in the sum of temperatures in Irkutsk for 1873-2019.
(in the upper right corner: *S* - standard deviation; *r* - correlation coefficient)

From the scatter plot in Figure 2, the lowest point of the sum of temperatures is –99.2 °C for 1977. From this moment, the sum of temperatures begins to rise. As a result, as well as throughout the land of the Earth, warming in Irkutsk began in 1977. However, it may turn out that the second term in Table 2 can eventually turn into a fluctuation. In addition, the other three oscillations can also be far from strong disturbances.

The first term of the model in Table 2 is the well-known Laplace law (in mathematics), Mandelbrot (in physics), Zipf-Pearl (in biology) and Pareto (in econometrics). It shows the tendency of the sum of temperatures to decrease. The second component is the biotechnical law [25] and it always shows the convexity of the parameter values. However, the thermodynamics of the atmosphere always has the property of oscillatory adaptation and the biotechnical law cannot indicate a wave in the future, therefore, after the rise, there will be only one transition to a decrease.

The third term from Table 2 (the first oscillation in Figure 1) is an infinite-dimensional wavelet that has no boundaries along the abscissa axis, in which the amplitude changes according to the Mandelbrot law modified by us with the introduction of a degree not equal to 1. The oscillation period for 1873 equals 2 × 813.6061 = 1627 years. Over time, the oscillation period began to decrease sharply, and since 1987 a new wave began with a half-period of about 140 years. The remaining two wavelets are finite-dimensional, having boundaries along the abscissa. Gradually, they will fade in amplitude to zero, but, as can be seen from the graphs, after a very distant time in the future.

By direct calculations in Excel using the formulas from Table 2 (preserving 11 decimal places from the results of parameter identification (1) in the CurveExpert-1.40 software environment), we obtain an approximate forecast up to 2165 (Figure 3).

The forecast graph in Figure 2 shows that in 2064 the sum of temperatures will become above zero, and by 2165 it can reach 35.6 °C. But it may turn out that after the year 2165 the sum of temperatures can decrease again.

5.2 Dynamics of Moving Average Annual Temperature Since 1873

This parameter, which smoothes the time series, is calculated by the formula:

$$\widetilde{t}_{\tau_2} = \sum t_{\tau_1} / \tau_2 = \sum_{\tau_2=1}^{\tau_2=147} \sum_{\tau_1=0}^{\tau_1=146} t_{\tau_1} / \tau_2 \qquad (3)$$

Table 3 gives the values of the parameters of the general model (1) and the adequacy in terms of the correlation coefficient, and Figure 4 shows the graphs of individual wavelets.

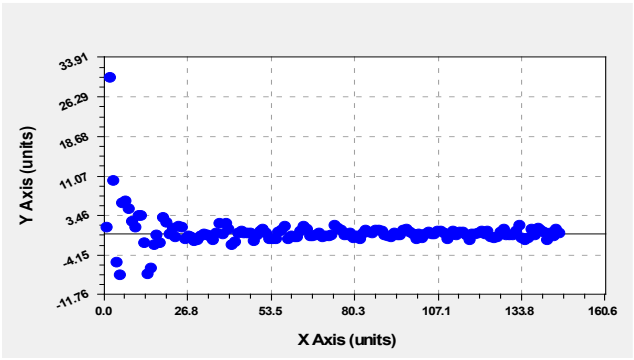

Dynamics of relative error

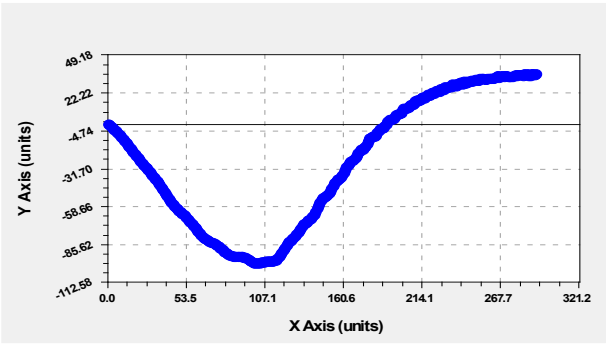

The sum of temperatures for the period 1873-2165

Figure 3. Plots for the five-term model with parameters from Table 2.

Table 3. Parameters (1) of the moving average temperature of Irkutsk for 1873-2019.

i	**Asymmetric wavelet** $y_i = a_{1i}x^{a_{2i}}\exp(-a_{3i}x^{a_{4i}})\cos(\pi x/(a_{5i}+a_{6i}x^{a_{7i}})-a_{8i})$								**Coef. correl. r**
	Amplitude (half) oscillation				**Half cycle oscillation**			**Shift**	
	$\mathbf{a_{1i}}$	$\mathbf{a_{2i}}$	$\mathbf{a_{3i}}$	$\mathbf{a_{4i}}$	$\mathbf{a_{5i}}$	$\mathbf{a_{6i}}$	$\mathbf{a_{7i}}$	$\mathbf{a_{8i}}$	
1	–0.18414	0	–0.8717503	0.27778	0	0	0	0	
2	0.0045055	1.42940	0	0	0	0	0	0	0.9962
3	6.77951	0.18727	2.71511	0.29156	0.912231	–0.043886	1.27041	1.43681	
4	–6.02349e-7	4.75806	0.18717	0.96540	13.42004	–0.016304	1.11774	–1.02747	0.5693
…	…	…	…	…	…	…	…	…	…
19	–1.40196e-6	2.61204	0.056036	0.99096	3.63892	–0.00098656	0.96206	0.61459	0.1869

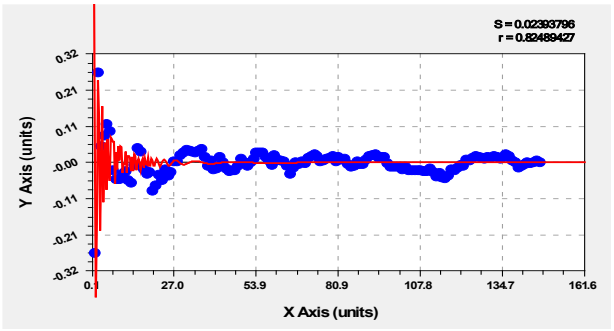

First oscillation

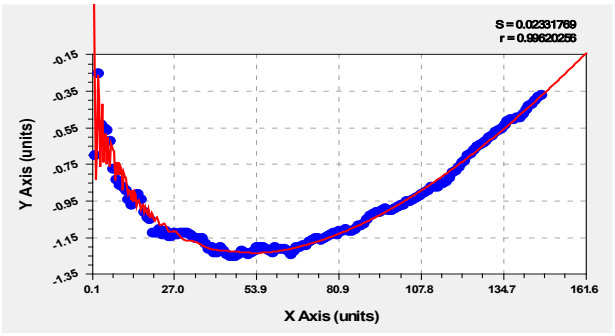

Trend and one swing

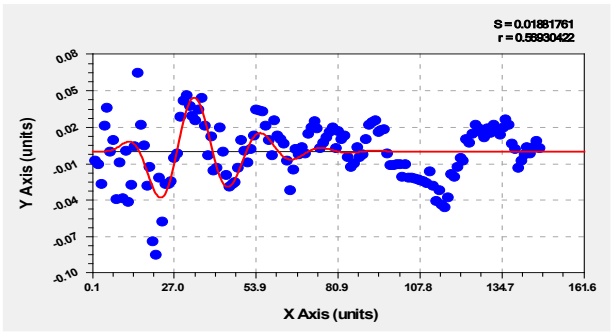

Second oscillation

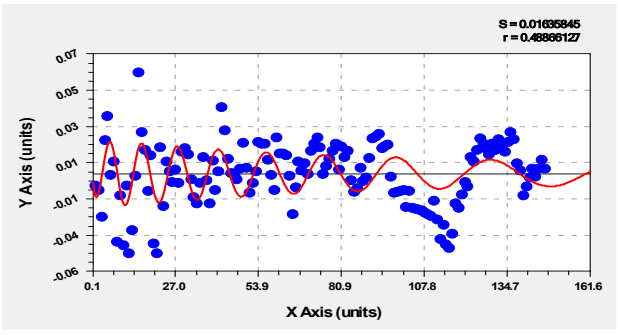

Third oscillation

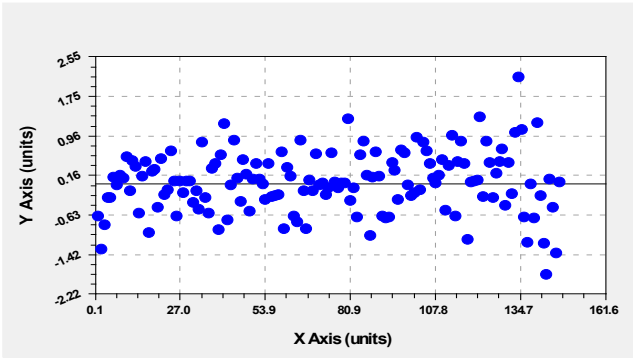

Relative error after the 19th component

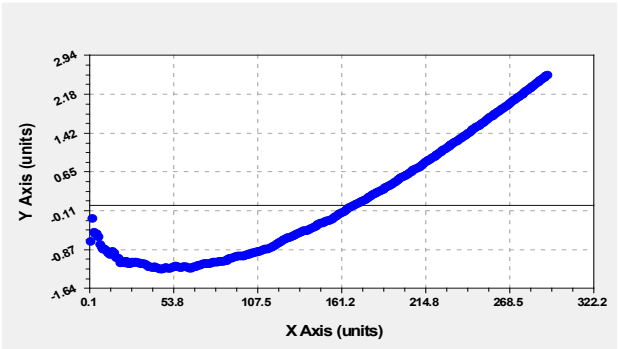

Forecast of the moving average for 1873-2165

Figure 4. Graphs of moving average temperature in Irkutsk for 1873-2019.

Due to the second term of the power law trend, it is impossible to predict this temperature parameter, since according to this simple equation there is a continuous increase in the sliding temperature over the years. Therefore, it is necessary to switch to the identification of the mean annual temperature from 1820.

5.3 Dynamics of the Average Annual Temperature Since 1820

Our research has shown that the duration of 146 years since 1873 is not enough time to identify only non-linear trends. It turned out that to identify the first oscillation (instead of a trend), a series with a length of at least 175 years is needed. In this regard, a series of 200 years for Irkutsk (albeit with gaps at the beginning of the series) made it possible to reveal the first quantum of behavior in the form of an asymmetric wave equation (wavelet). It follows from this that it is impossible to make temperature forecasts with a series length of at least 175 years, that is, the dynamic series of the average annual temperature with any measurement period and for any weather stations should begin no later than 1845.

The two-term trend (Figure 5) is determined by an equation of the form:

$$t = -4.77083 \cdot 10^{-7} \exp(7.36060\tau^{0.18257}) + 1.09883\tau^{3.49994} \quad (4)$$

And the oscillatory perturbation of the average annual temperature in Irkutsk is determined by the first equation of the infinite-dimensional wavelet.

$$t = -0.95369 \exp(0.0032716\tau) \cos(\pi\tau / (879.70973 - 672.03732\tau^{0.020834}) - 2.01653) \quad (5)$$

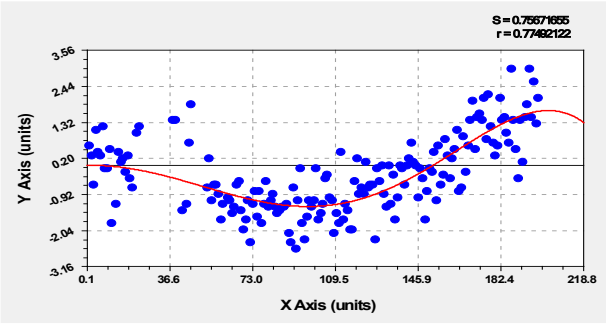

Two term trend (4)

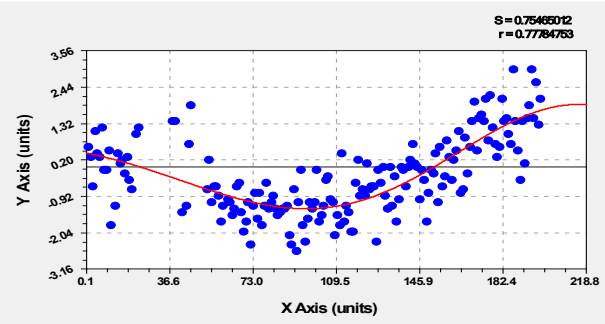

Initial wavelet signal (5)

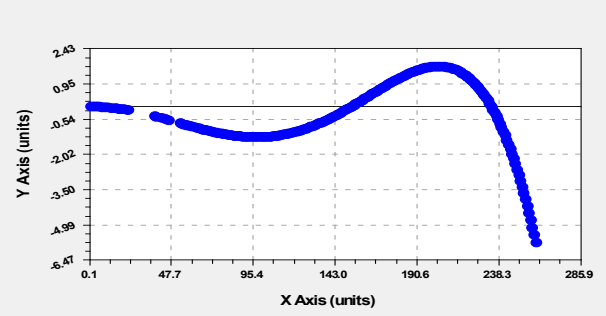

Forecast on a two-component trend until 2080

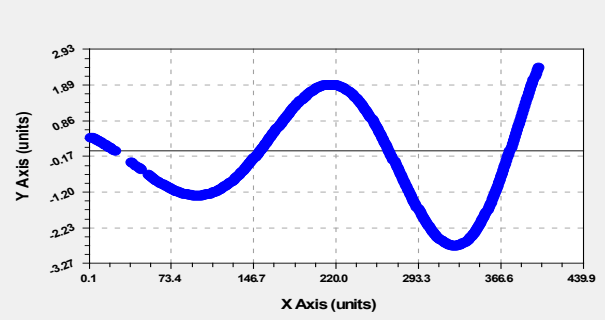

Oscillation forecast (5) until 2220

Figure 5. Graphs of temperature dynamics in Irkutsk for 1820-2019 and forecast until 2220.

The trend correlation coefficient in the form of a wavelet (5) is 0.7778, and in the form of a two-term non-linear trend (4) is 0.7749. Then, in terms of adequacy, the wavelet is more significant than the trend. And it can be taken as the beginning of the oscillatory separation of the climate.

According to Equation (5), we have that the fluctuation period in 1820 for the climate of Irkutsk was equal to 2 × 879.70973 = 1759.4 years. The amplitude, according to the Mandelbrot law, shows the tendency of the average annual temperature to the absolute temperature of –273.15 °C, that is, the separation of the Earth's climate system will lead, as on Mars, to global cooling. Therefore, warmings are only episodes in climate evolution.

According to the trend wave from 1820 to 1916, the average annual temperature at the meteorological station of Irkutsk dropped from +0.40 to –1.29 °C, so this period is characterized as a cooling. Then, from 1916 to 2035, with a time interval of 119 years, there is a warming up to 1.91 °C. The difference in average annual temperatures will be equal to 3.20 °C. After that, from 2035 to 2145, the average annual temperature will again decrease to –2.75 °C. Over a time interval of 110 years, a cooling of 4.66 °C will occur. From 2145 to 2251 in the interval of 106 years, according to the preliminary forecast, there will again be warming from –2.75 °C to +3.88 °C with a difference of 6.63 °C. Thus, the climate near Irkutsk will go into overdrive with increasing amplitude.

According to the initial wave, it turns out that the ecological system at the Irkutsk point tends to increase the amplitude and reduce the half-period of oscillation, thereby gradually approaching an emergency situation, as in a car engine. Moreover, this situation is approaching more and more quickly along the half-period from about 1760 years to the values of 119, 110 and 106 years. Of course, such a strong increase in climate fluctuations depends on the strengthening of anthropogenic influence.

5.4 Full Wavelet Analysis of Mean Annual Temperature

Climate change occurs along a powerful bundle of a large number of wavelets, when up to 200 wavelets can be consistently identified in one bundle in the form of a general model (1) of temperature dynamics [25].

A complete wavelet analysis is possible when all behavior quanta at the end of the identification process will give a modeling error on the residuals from the last asymmetric wavelet less than the measurement error. According to the values of the average annual temperature in Table 1, the division price is 0.1 °C. Then the measurement error of the mean annual temperature will be ± 0.05 °C.

According to the computing capabilities of the CurveExpert-1.40 software environment, joint identification is possible up to 3-4 members. In this case, the parameters of the model change by value and this is similar to the effect

of compaction when the box is shaken. Then it turns out that it is necessary to create a special software environment that allows obtaining up to 200 terms of Equation (1) for the time-temperature pair. They will have up to 1600 simultaneously shaken model parameters. The length of the row by the number of lines should be at least 100 thousand. We have scenarios for the identification process.

Table 4 shows examples of wavelets that continue beyond 2019 and this allows direct prediction in Excel. Of the 86 terms, 47 components have an impact after 2019 (all infinite-dimensional wavelets fall here), and 39 finite-dimensional wavelets have already remained in the past until 2019. Therefore, they can be ignored in forecasting.

In Table 4, together the first three terms gave a correlation coefficient of 0.8126, with the first four oscillations being infinite dimensional wavelets. Of these, terms No. 1 and No. 4, according to the half-amplitude formula, are the Mandelbrot law for $a_{4i}=1$, and terms No. 2 and No. 3 are the Mandelbrot law modified by us under the condition $a_{4i}\neq 1$. With the highest adequacy at a correlation coefficient of 0.6548, oscillation No. 36 belongs to a finite-dimensional wavelet.

Some of the 86 wavelets are shown in Figure 6, and the initial wavelet was shown in Figure 6. The presence of finite-dimensional wavelets with the beginning and end of the oscillation makes forecasting difficult, since after the end of the forecast base, new local (short segments on the x-axis) oscillations may appear.

Together, the three fluctuations give a small temperature tremor since 1996. At the same time, terms #27 and #36 continue into the future, but begin around 1840.

Figure 7 shows graphs of the 86th quantum of the behavior of the average annual temperature of Irkutsk and points from the residuals, which are much less than ± 0.05 °C. Therefore, we can assume that the full wavelet analysis of the dynamic series of the average annual temperature of Irkutsk from 1820 to 2019 was carried out. Then for those components that continue their influence (infinite-dimensional and finite-dimensional wavelets) after 2019, the sum can be calculated with 11 significant digits for the model parameters (1). To verify the forecasts, the formulas should be calculated for 2020 and 2021 and compare the calculated and actual values of the average annual temperature.

Table 4. Parameters (1) of the dynamics of the average annual temperature of Irkutsk for 1820-2019.

i	**Asymmetric wavelet** $y_i = a_{1i}x^{a_{2i}}\exp(-a_{3i}x^{a_{4i}})\cos(\pi x/(a_{5i}+a_{6i}x^{a_{7i}})-a_{8i})$								**Coef. correl. r**
	Amplitude (half) oscillation				**Half cycle oscillation**			**Shift**	
	$\mathbf{a_{1i}}$	$\mathbf{a_{2i}}$	$\mathbf{a_{3i}}$	$\mathbf{a_{4i}}$	$\mathbf{a_{5i}}$	$\mathbf{a_{6i}}$	$\mathbf{a_{7i}}$	$\mathbf{a_{8i}}$	
1	–1.45648	0	–0.00054511	1	–793.72078	796.84232	0.021229	3.52895	
2	3.62339	0	0.16097	0.67805	39.07346	–6.80511	0.13692	–1.66398	0.8126
3	1.88937	0	–7.40020	0.099365	220.28835	–0.66686	1.06022	–3.23605	
4	–0.20304	0	0.0039260	1	12.59928	–0.028013	1.14617	–1.90902	0.1469
…	…	…	…	…	…	…	…	…	…
36	–1.52521e-12	9.08512	2.21324	0.43428	1.80273	0	0	3.10990	0.6548
…	…	…	…	…	…	…	…	…	…
67	0.00069493	1.10961	0.064035	0.74812	1.02341	0	0	–1.65995	0.2400
73	7.62225e-7	2.22007	0.010537	0.99415	175.25799	–0.75130	1.00002	–5.60264	0.1761
75	1.73871e-8	2.76191	0.00099972	0.95693	1.33323	0	0	–5.13988	0.3414
76	–2.38153e-6	1.92272	0.010470	0.99364	1.28797	0	0	–6.01353	0.1609
81	–0.020567	0	0.20097	0.33435	1.76447	0.0076570	0.99933	–0.89750	0.2845
83	–1.97290e-28	14.83049	0.098036	0.99395	4.50669	–0.0017426	1.11121	–3.32612	0.4362
85	3.33419e-6	1.94059	0.010077	0.98363	2.47227	0	0	–0.13150	0.3877
86	–0.0069195	0	–0.00035802	1	4.03746	0.00048849	0.99942	1.46876	0.2806

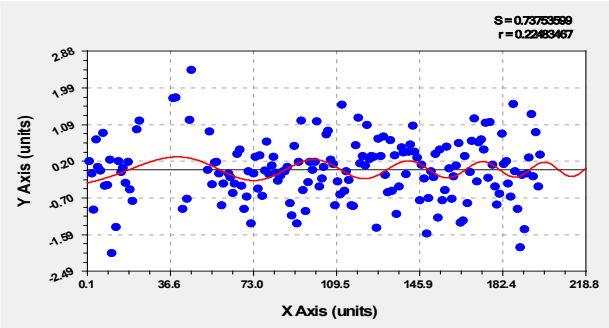

Second oscillation

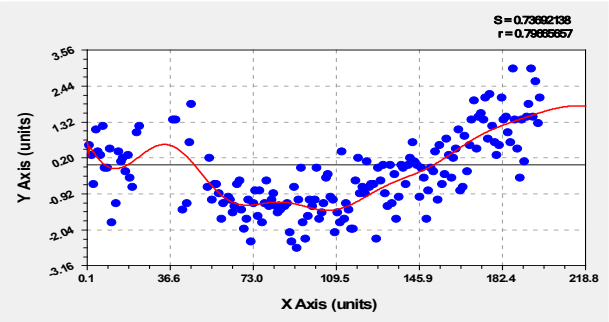

Together, two vibrations

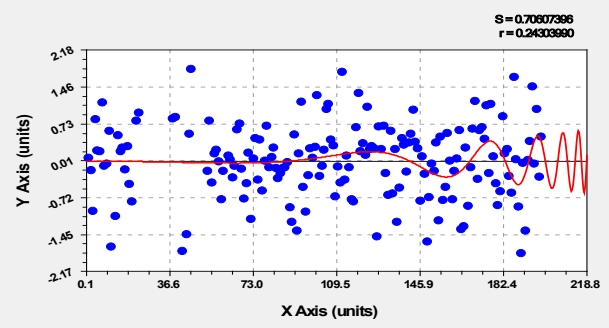

Third oscillation

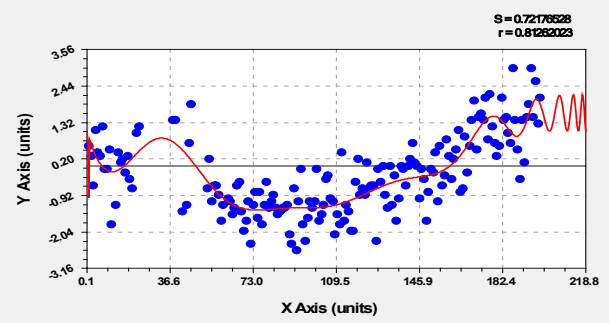

Jointly three vibrations

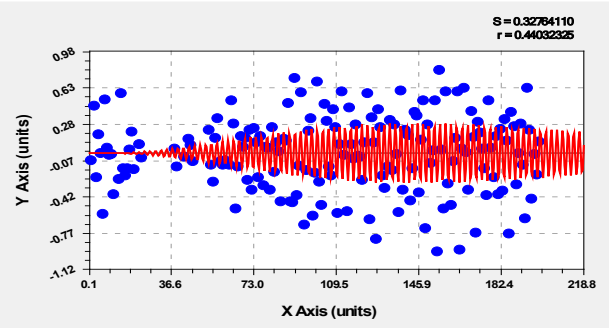

27th model member (1)

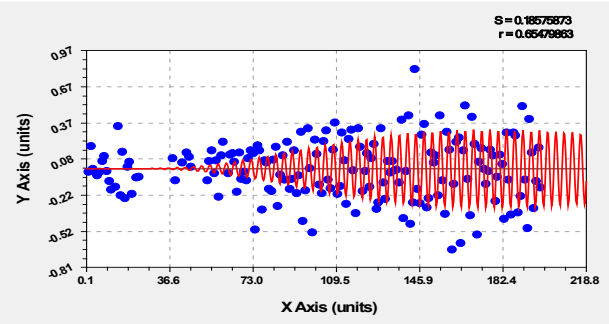

36th model member (1)

Figure 6. Graphs of the dynamics of the average annual temperature in Irkutsk for 1820-2019

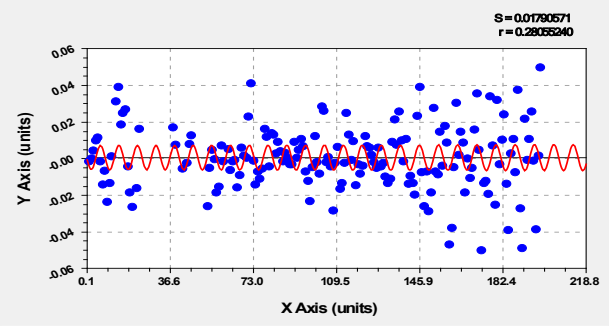

86th model member (1)

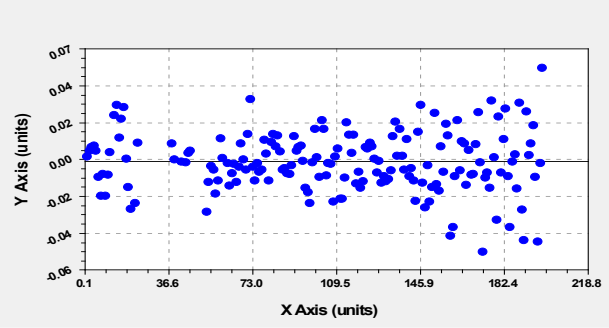

Residuals after the 86th term of the general model

Figure 7. Latest graphs of the average annual temperature in Irkutsk for 1820-2019.

Then it turns out that the dynamic temperature series has a high quantum certainty, since it allows quantizing the change in the average annual temperature of Irkutsk by 86 oscillations up to a measurement error in 47 components.

6. Discussion of Results

6.1 Stages of Climate Behavior in Irkutsk

In a series from 1820 to 1865, a sharp cooling was observed. Moreover, the beginning of this cycle is unknown. Then, around 1966, warming began, which continues to this day. But the forecast will show how long this warming will continue.

The high pollution of urban air makes the forecast of Irkutsk temperature until 2020 conditional and only indicative. But, apparently, only infinite-dimensional wavelets will be preserved for the future, therefore, in forecasts until 2220, we will not take into account those finite-dimensional wavelets that terminate along the right boundary until 2019.

6.2 Fractal Analysis of Wavelets

Standard deviations (shown in the upper right corner) are given in Table 5.

The zero number was given to the arithmetic mean value with a standard deviation of 1.1832 °C. Then the parameter i is the rank of each wavelet (Figure 8).

Table 5. Change in the standard deviation of mean annual temperature wavelets.

i	S, °C	i	S, °C	i	S, °C	i	S, °C	i	S, °C	i	S, °C
0	1.1832	15	0.4681	30	0.2798	45	0.0987	60	0.0483	75	0.0286
1	0.7547	16	0.4597	31	0.2618	46	0.0947	61	0.0467	76	0.0282
2	0.7369	17	0.4546	32	0.2601	47	0.0883	62	0.0450	77	0.0281
3	0.7218	18	0.4380	33	0.2567	48	0.0798	63	0.0428	78	0.0265
4	0.6922	19	0.4260	34	0.2520	49	0.0784	64	0.0420	79	0.0258
5	0.6704	20	0.4084	35	0.2473	50	0.0734	65	0.0407	80	0.0256
6	0.6585	21	0.4054	36	0.1858	51	0.0646	66	0.0398	81	0.0248
7	0.6424	22	0.3914	37	0.1766	52	0.0639	67	0.0384	82	0.0242
8	0.6201	23	0.3865	38	0.1473	53	0.0614	68	0.0383	83	0.0219
9	0.6038	24	0.3824	39	0.1433	54	0.0594	69	0.0367	84	0.0204
10	0.5824	25	0.3783	40	0.1412	55	0.0579	70	0.0365	85	0.0187
11	0.5632	26	0.3649	41	0.1274	56	0.0541	71	0.0356	86	0.0179
12	0.5438	27	0.3276	42	0.1178	57	0.0532	72	0.0352		
13	0.5166	28	0.3032	43	0.1094	58	0.0524	73	0.0348		
14	0.4980	29	0.2920	44	0.0990	59	0.0519	74	0.0304		

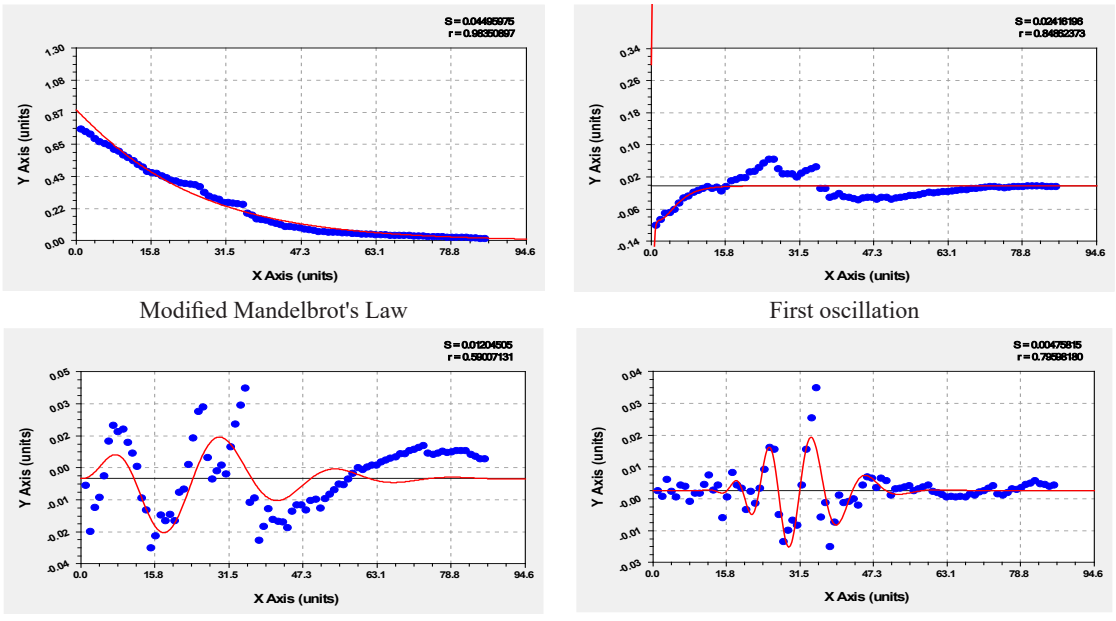

Figure 8. Graphs of the standard deviation of temperature in Irkutsk for 1820-2019.

After identification, a four-term formula of the form:

$$S = S_1 + S_2 + S_3 + S_4, \quad (6)$$

$$S_1 = 0.97975\exp(-0.039423i^{1.04953}),$$

$$S_2 = A_1\cos(\pi i / p_1 + 0.72450),$$

$$A_1 = 0.26945\exp(-0.052207i),$$

$$p_1 = -63.22677 + 642.19439i^{0.061051},$$

$$S_3 = A_2\cos(\pi i / p_2 + 1.90902),$$

$$A_2 = -0.0057598i^{2.51939}\exp(-0.28579i),$$

$$p_2 = 17.58283,\ S_4 = A_3\cos(\pi i / p_3 - 1.50203),$$

$$A_3 = -4.66337\cdot10^{-17}i^{13.79035}\exp(-0.40072i^{1.02706}),$$

$$p_3 = 1.68217 + 0.036085i^{1.01190}.$$

The first term is modified by us subject $c \neq 1$ to the Mandelbrot law in the form $y = a\exp(-bx^c)$. Then it turns out that the quanta of behavior themselves are distributed fractally, but, unlike Mandelbrot, not multiple and with fluctuations.

6.3 Distribution of Residuals after the 86th Component of the Model

The number of points n_ε (pieces) in one interval after 0.01 °C of the absolute error $[\varepsilon]$ (°C) changes according to the Gauss law (Figure 9) in the form of an equation:

$$n_\varepsilon = 1 + 40.33057\exp(-1774.700([\varepsilon] + 0.0044307)^2) \quad (7)$$

The normal distribution law is observed with an adequacy of 0.9703.

6.4 Relative Error Distribution of Residuals

A formula was obtained (Figure 9) of the form:

$$n_\Delta = 1 + 42.08733\exp(-0.18650([\Delta] - 0.0091613)^2) \quad (8)$$

Due to zero temperature, the relative error is equal to infinity, and there were five such points in total. Then, out of 200 points, there are no measurements at 27 points, so the representativeness of the statistical sample for the residuals will be 86.5%, and for the relative error (173 – 5) / 200 = 84.0%.

6.5 Influence of Solar Activity Cycles on Temperature Dynamics

Let us briefly consider the relationship of the model parameter (1) a_{5i} with solar cycles (the cycle of revolution of the Sun's core around itself is on average 22.6 years and the cycle of solar activity according to Wolf numbers is on average 11.3 years).

The first three fluctuations, according to Table 4, apparently have cosmic influences outside the solar system. And the fourth term has an initial cycle in 1820 equal to $2 \times 12.59928 \approx 25.2$ years, which corresponds to the revolution cycle of the Sun's core. Then it turns out that over time, the Earth's atmosphere, due to the high plasticity of sliding, and the influence of eddies, reduces this initial cycle.

The fifth component has a cycle of $2 \times 6.54983 \approx 13.1$ years, but with a negative sign. This initial value corresponds to the cycle of solar activity according to Wolf numbers. The next wavelet has half the cycle of solar activity.

The seventh wavelet at the beginning in 1820 had a one and a half year cycle. But the eighth term received a constant period of oscillation of four years. The next term has a three-year constant period. There are several wavelets No. 10, 12, 26, 43, 63 and 67 around the two-year constant biological cycle of the productivity of fruit trees and shrubs. The rest of the cycles, apparently, depend on the behavior of the Earth's atmosphere.

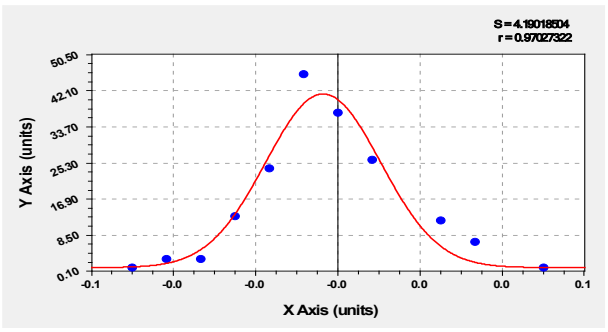

Absolute error (residuals)

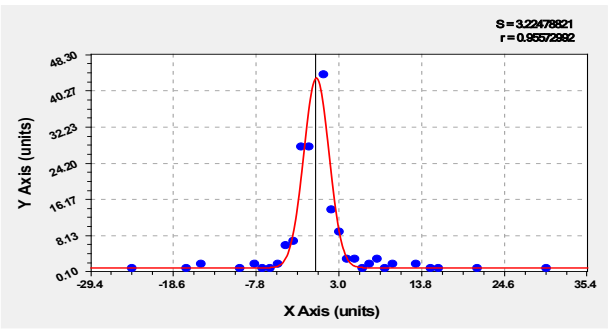

Relative error, %

Figure 9. Graphs of the distribution of statistical indicators of temperature for 1820-2019.

7. Forecast of the Average Annual Temperature of Irkutsk

7.1 Calculation Example in Excel Taking into Account Significant Figures

The parameters of the model with five significant figures given in Table 4 turned out to be insufficient in direct calculations.

In this regard, all 11 significant figures were accepted, for example, the fourth term:

User-Defined Model: y=–a*exp(–b*x)*cos(pi*x/(c–d*x^e)+f)

Coefficient Data:

a = 2.03039345976E – 001

b = 3.92600098388E – 003

c = 1.25992844772E + 001

d = 2.80126347775E – 003

e = 1.14616905207E + 000

f = 1.90902374656E + 000

The calculation in Excel was performed on 3, 12 and 47 components of the general model (1).

7.2 Base and Forecast Horizon Charts 1820-2260

First, for the first three fluctuations from Table 4 with a correlation coefficient of 0.8126 (the level of adequacy is "a strong factorial relationship" with a correlation coefficient of at least 0.7), a graph was plotted in the range from 1820 to 2260, which is shown in Figure 10. Then the graph is built on the first 12 components of the general model (1).

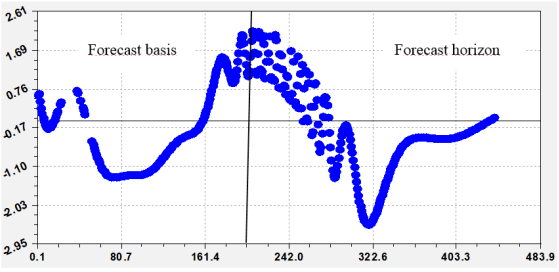

a) by the first three wave components

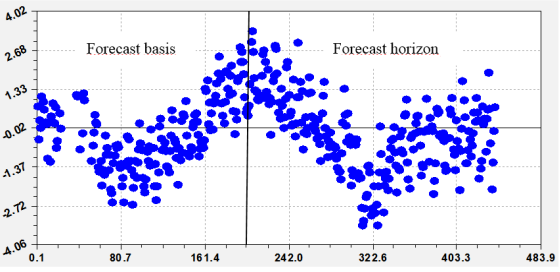

b) by 12 first wave components

Figure 10. Graphs of the dynamics of the average annual temperature of Irkutsk for 1820-2260.

And Figure 11 shows a graph of the forecast for all 47 members for 2020-2220. At the same time, due to the exclusion of past finite-dimensional wavelets, it is impossible to build a graph for all members to base the forecast 1820-2019. For a complete graph, it is necessary to build according to the calculation of all 86 members of the general model (1).

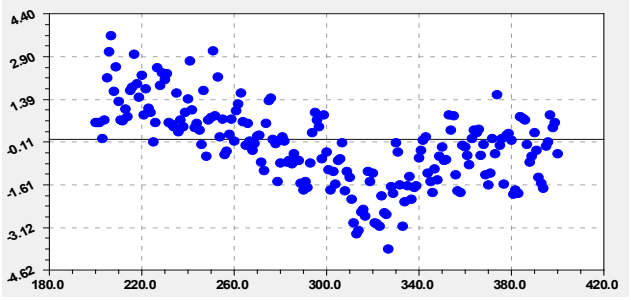

Figure 11. Graph of the forecast horizon for the average annual temperature of Irkutsk for 2020-2220.

It can be seen from the three graphs that with an increase in the number of terms (1), the spread of the average annual temperature ordinate increases: for three terms, the temperature interval along the ordinate axis is from –2.95 °C to 2.61 °C; for 12 members from –4.06 °C to 4.02 °C; for the forecast for the period 2020-2220 from –4.62 °C to 4.40 °C.

As can be seen from the three-term graph, from 2020 to 2080, there will be a strong decrease in temperature with a very strong tremor. The average temperature in Irkutsk has been above zero since 1980. At the same time, 12 components already give an interval forecast. According to 47 wavelets from Figure 11, it can be seen that until 2040 there will be a wave of oscillatory climate disturbance with a strong amplitude according to the data of the Irkutsk meteorological station.

7.3 Verification of the Average Annual Temperature Forecast

Due to strong climate fluctuations and the possibility of more and more fluctuations from factors influencing the average annual temperature (accordingly, new finite-dimensional fluctuations appear), the forecasting process can only be iterative, for example, after the data for each year become available. To do this, it is possible to annually re-identify all 86 members of the general model (1). In this case, additional fluctuations may appear.

To what extent can we trust the forecast data up to 2220? Of course, with the distance from 2019, the probability of a good forecast will significantly decrease.

Such differences in the average annual temperature in Irkutsk are formed with periodicity: –0.10 °C (2045);

–2.53 °C (2047); –0.26 °C (2056). Then there will be differences: 3.11 °C (2071); –0.54 °C (2076); 1.63 °C (2083). From 2120, global cooling will begin in Irkutsk, as it was in the period 1870-1980 (the cycle is 110 years).

Thus, the current global warming will be replaced by global cooling. The climate system on the example of Irkutsk is undergoing oscillatory adaptation to changing external influences. For such short cycles of 2040 – 1980 = 60 years of warming, the vegetation cover will not have time to undergo fundamental changes even in the species composition of plants. This requires millennium cycles, but trees have adapted to such cycles for 400 million years of evolution, and grass for more than 100 million years of development. Then it turns out that the vegetation on the territory is quickly changed by man with his predatory activity and the indefatigable doctrine of the conquest of nature.

7.4 Relative Forecast Error for 2020-2021

Table 6 shows the actual and calculated according to the forecasts by three, 12 and 47 components of the average annual temperature in Irkutsk.

Table 6. Verification of the average annual temperature of Irkutsk for 1820-2021.

Year	Time τ, year	Fact t, °C	Design temperature 3	12	47	Fact - calculation 3	12	47	Error Δ, % 3	12	47
2019	199	2.1	1.73	1.86	2.02	0.37	0.24	0.08	17.62	11.43	3.81
2020	200	2.8	1.75	1.06	0.58	1.05	1.74	2.22	37.50	62.14	79.3
2021	201	1.6	1.77	0.52	0.60	-0.17	1.08	1.00	-10.63	67.50	62.5

Three quantum powers (3, 12 and 47 components) of modeling the dynamics of the average annual temperature of Irkutsk by the model identification method (1) show different relative errors. For a model with 47 members in the last year of the time series, 2019, a relative error was obtained. But the next two years, due to the high sensitivity of the model, give a high error of 79.3%. Then a large number of wavelets are redundant. For a model with 12 terms, the maximum error is 67.50% for 2021. For outlooks, a simple three-term model is possible. The modeling error, as in ecological studies, here is mainly within 30%.

8. Conclusions

In the biophysics of the atmosphere, according to long-term data since 1820, it has been proven that the dynamic series of the average annual temperature, using the example of Irkutsk, is decomposed into 86 asymmetric wavelets up to the measurement error. As a result, the fractality of the decomposition of the temperature of the surface air layer over 200 years into individual behavior quanta is clearly visible. At the same time, the frequency of fluctuations will not be able to cause serious changes in the species composition of the vegetation cover. In addition, for an approximate forecast, a model containing only the first three terms of the quantum expansion turned out to be sufficient.

The revealed patterns of the average annual temperature of Irkutsk from 1820 to 2019 made it possible to positively answer the statement that the IPCC reports cannot provide a complete and detailed picture of regional assessments of climate change. Of all the weather stations in Russia, it is necessary to select those that have a temperature series length of at least 175 years, that is, the first temperature measurements were made no later than 1845. Then such series should be identified for other regions of the world with different classes of soil cover according to the UN classification.

A criterion is proposed in dynamics—the sum of temperatures, which is a measure of the average kinetic energy of the translational motion of molecules in a 2 m layer above the land surface. However, this indicator requires the continuity of the dynamic series, therefore, for Irkutsk, the sum of temperatures could be accepted only from 1873. Then the basis of the forecast is 2019 – 1873 = 146 years. The first three components gave a very high correlation coefficient of 0.9996 and the forecast for the five components until 2165 showed a trend towards a certain limit of the sum of the mean annual temperature.

The second proposed indicator is a moving average, calculated as the ratio of the sum of temperatures to the current time. The first three wavelets gave a correlation coefficient of 0.9962. However, a small forecast base does not make it possible to predict.

In the dynamics from 1820 to 2019, 86 wavelets were received, of which 47 oscillations affect the future. Then it turns out that the dynamic temperature series has a high quantum certainty, and this makes it possible to quantize the change in the average annual temperature of Irkutsk by 86 oscillations up to a measurement error of ± 0.05 °C. The identification process occurs as a complete wavelet analysis. The basis of the forecast in 200 years made it possible to replace the non-linear two-term trend with an oscillatory temperature perturbation. As a result, the first three fluctuations gave the level of adequacy "strong relationship" with a correlation coefficient of 0.8126, which is much higher than the required level of 0.7 strong adequacy.

With an increase in the number of model members (1), the ordinate of the average annual temperature increases: for three members, the temperature interval along the ordinate axis is from –2.95 °C to 2.61 °C; for 12 members,

from –4.06 °C to 4.02 °C; for the forecast for the period 2020-2220, from –4.62 °C to 4.40 °C. As can be seen from the three-term graph, from 2020 to 2080, there will be a strong decrease in temperature with a very strong tremor of temperature values. The average annual temperature in Irkutsk has been above zero since 1980. At the same time, 12 components already give an interval forecast. According to 47 wavelets from Figure 10, it can be seen that until 2040 there will be a wave of oscillatory climate disturbance with a strong amplitude.

Thus, the current global warming will be replaced by global cooling. The climate system, using the example of Irkutsk, undergoes oscillatory adaptation to changing external influences. For such short cycles of 2040 – 1980 = 60 years of warming, the vegetation cover will not have time to undergo fundamental changes in the species composition of plants.

Conflict of Interest

There is no conflict of interest.

References

[1] Friedrich, T., Timmermann, A., Tigchelaar, M., et al., 2016. Nonlinear climate sensitivity and its implications for future greenhouse warming. Science Advances. 2(11), e1501923.
DOI: https://doi.org/https://doi.org/10.1126/sciadv.1501923

[2] Causes of variability in long-term warming. Available from: https://www.metoffice.gov.uk/research/news/2018/causes-of-variability-in-long-term-warming-since-the-late-19th-century

[3] Jenkins, A., 2009. The Ups and Downs of Global Warming. NASA Global Climate Change [Internet]. Available from: https://climate.nasa.gov/news/175/the-ups-and-downs-of-global-warming/#:~:text=The%20warming%20trend%20over%20the,1980s%20over%20land%20and%20ocean

[4] Weart, S., 2019. The Modern Temperature Trend. The Discovery of Global Warning [Internet]. Available from: https://history.aip.org/climate/20ctrend.htm

[5] Yirka, B., 2018. Study Suggests Three Periods of Global Warming Slowdown Since 1891 due to Natural Temporary Causes [Internet]. Available from: Https://phys.org/news/2018-06-periods-global-slowdown-due-natural.html

[6] Swain, D.L., Horton, D.E., Singh, D., et al., 2016. Trends in atmospheric patterns conducive to seasonal precipitation and temperature extremes in California. Science Advances. 2, e1501344.

[7] Wu, Z., Huang, N.E., Wallace, J.M., et al., 2011. On the time-varying trend in global-mean surface temperature. Climate Dynamics. 37, 759.
DOI: https://doi.org/10.1007/s00382-011-1128-8

[8] Kislov, A.V., Varentsov, M.I., Gorlach, I.A., et al., 2017. Heat island of the Moscow agglomeration and the urban-induced amplification of of global warming. Vestnik Moskovskogo universiteta. Seriia V, Geografiia. (5), 12-19. Available from: https://www.researchgate.net/publication/320057275

[9] Zappalà, D.A., Barreiro, M., Masoller, C., 2018. Quantifying changes in spatial patterns of surface air temperature dynamics over several decades. Earth System Dynamics. 9, 383-391.
DOI: https://doi.org/10.5194/esd-9-383-2018

[10] Wang, J.F., Xu, Ch.D., Hu, M.G., et al., 2017. Global land surface air temperature dynamics since 1880. International Journal of Climatology. 38(S1), e466-e474.
DOI: https://doi.org/10.1002/joc.5384

[11] Stouffer, R.J., Hegerl, G., Tett, S., 1999. A comparison of surface air temperature variability in three 1000-yr coupled ocean-atmosphere model integrations. Journal of Climate. 13, 513-537.

[12] Li, G.X., Zhou, G., 2016. Comparisons of time series of annual mean surface air temperature for china since the 1900s: Observations, model simulations, and extended reanalysis. Bulletin of the American Meteorological Society. 98(4), 699-711.
DOI: https://doi.org/10.1175/bams-d-16-0092.1

[13] Ding, J., Cuo, L., Zhang, Y.X., et al., 2018. Monthly and annual temperature extremes and their changes on the Tibetan Plateau and its surroundings during 1963-2015. Scientific Reports.
DOI: https://doi.org/10.1038/s41598-018-30320-0

[14] Chernokulsky, A., 2022. Will Europe Freeze without the Gulf Stream? [Internet] [cited 2022 Mar 13] Available from: https://zen.yandex.ru/media/nplus1/zamerznet-li-evropa-bez-golfstrima-62028bab5eaa831b62461219?&utm_campaign=dbr& (in Russian)

[15] Mazurkin, P.M., 2021. Bioclimatic regularities of change in the density of organic carbon of the steppe soil in different regions of the World. Journal of Atmospheric Science Research. 4(1), 16-25.
DOI: https://doi.org/10.30564/jasr.v4i1.2521

[16] Mazurkin, P.M., 2021. Factor analysis of the parameters of samples of the steppe soil and grass of Mongolia and Inland Mongolia of China on the eastern transect of the Eurasian steppe. Journal of Geological Research. 3(1), 1-10.
DOI: https://doi.org/10.30564/jgr.v3i1.2520

[17] Cheredko, N.N., Tartakovsky, V.A., Volkova, Yu.V., et al., 2020. Transformation of the spatial structure of the surface temperature field of the northern hemisphere. Izvestiya RAN. Geographic Series. 1, 47-55. (in Russian)
DOI: https://doi.org/10.31857/S2587556620010057

[18] Alvarez-Castro, M.C., Faranda, D., Yiou, P., 2018. Atmospheric dynamics leading to west european summer hot temperatures since 1851. Hindawi Complexity. Article ID 2494509.
DOI: https://doi.org/10.1155/2018/2494509

[19] Babushkina, E.A., Belokopytova, L.V., Shah, S.K., et al., 2018. Past crops yield dynamics reconstruction from tree-ring chronologies in the forest-steppe zone based on low- and high-frequency components. International Journal of Biometeorology. 62, 861-871.
DOI: https://doi.org/10.1007/s00484-017-1488-9

[20] Dahlhausen, J., Rtzer, Th., Biber, P., et al., 2018. Urban climate modifies tree growth in Berlin. International Journal of Biometeorology. 62, 795-808.
DOI: https://doi.org/10.1007/s00484-017-1481-3

[21] Wang, J., Yuan, Z., Wu, O., et al., 2019. Warming changed soil respiration dynamics of alpine meadow ecosystem on the Tibetan Plateau. Journal of Environmental & Earth Sciences. 1(2).
DOI: https://doi.org/10.30564/jees.v1i2.511

[22] Zharkova, V., 2019. The Solar Magnet Field and the Terrestrial Climate [Internet] [cited 2019 Mar 1]. Available from: https://watchers.news/2018/11/11/valentina-zharkova-solar-magnet-field-and-terrestrial-climate-presentation/

[23] Zherebtsov, G.A., Kovalenko, V.A., Molodykh, S.I., et al., 2013. Influence of solar activity on the temperature of the troposphere and ocean surface. Bulletin of the Irkutsk State University. Earth Sciences Series. 6(1), 61-79. (in Russian)

[24] Mazurkin, P.M., 2019. Wavelet analysis of annual dynamics of maximum temperature from 1878 to 2017 And forecast data Hadley center Central England temperature (Hadcet). International Journal of Current Research. 11(09), 7315-7324. Available from: https://www.journalcra.com/article/wavelet-analysis-annual-dynamics-maximum-temperature-1878-2017-and-forecast-data-hadley

[25] Mazurkin, P.M., 2021. Quantum biophysics of the atmosphere: Factor analysis of the annual dynamics of maximum, minimum and average temperatures from 1879 to 2017 to Hadley English Temperature Center (Hadcet). Journal of Environmental & Earth Sciences. 3(1).
DOI: https://doi.org/10.30564/jees.v3i1.2489

[26] Mazurkin, P.M., Kudryashova, A.I., 2019. Quantum meteorology. International Multidisciplinary Scientific GeoConference Surveying Geology and Mining Ecology Management, SGEM. (5.1), 619-627.

[27] Kochugova, E.A., 2015. Variability of winter minimum air temperatures in Cisbaikalia. Bulletin of the Irkutsk State University. Earth Sciences Series. 13, 98-110. (in Russian)

[28] Akhtimankina, A.V., Lopatkina, O.A., 2014. Study of the dynamics of concentrations of pollutants in the atmospheric air of Irkutsk. Bulletin of the Irkutsk State University. Earth Sciences Series. 9, 2-15. (in Russian).

[29] Marinaite, I.I., Golobokova, L.P., Netsvetaeva, O.G., et al., 2013. Long-term studies of atmospheric precipitation in the city of Irkutsk. Bulletin of the Irkutsk State University. Earth Sciences Series. 6(2), 138-147. (in Russian).

[30] Balkhanov, V.K., 2019. Fractal geometry: Axioms, fractal derivative and its geometrical meaning. Journal of Environmental & Earth Sciences. 1(1), 1-5.
DOI: https://doi.org/10.30564/jees.v1i1.475

BILINGUAL PUBLISHING CO.
Pioneer of Global Academics Since 1984

Journal of Environmental & Earth Sciences
https://ojs.bilpublishing.com/index.php/jees

ARTICLE

Vegetation Changes in Alberta Oil Sands, Canada, Based on Remotely Sensed Data from 1995 to 2020

Jinxin He[1] Debo Chen[1*] Ye Zhan[2] Chao Liu[1] Ruichen Liu[1]

1. College of Earth Sciences, Jilin University, Changchun, Jilin, China
2. Aviation University Air Force, Changchun, Jilin, China

ARTICLE INFO

Article history
Received: 20 March 2022
Revised: 2 June 2022
Accepted: 8 June 2022
Published Online: 16 June 2022

Keywords:
Alberta
Oil sands
Vegetation changes
Remote sensing
Landsat

ABSTRACT

There are rich oil and gas resources in Alberta oil sand mining area in Canada. In the 1960s, the Canadian government decided to increase the mining intensity. However, the exploitation will bring many adverse effects. In recent years, more people pay attention to the environmental protection and ecological restoration of mining areas, such as issues related to changes in vegetated lands. Thus, the authors used the Landsat-5 TM and Landsat-8 OLI remote sensing images as the basic data sources, and obtained the land cover classification maps from 1995 to 2020 by ENVI. Based on the NDVI, NDMI and RVI, three images in each period are processed and output to explore the long-term impact of exploitation. The results show that from 1995 to 2020, the proportion of vegetation around mining areas decreased sharply, the scale of construction land in the mining area increased, and the vegetated land was changed to land types such as tailings ponds, oil sand mines and other land types. In addition, three vegetation indexes decreased from 1995 to 2020. Although the exploitation of oil sand mining areas brings great economic benefits, the environmental protection (especially vegetation) in oil sand mining areas should be paid more attention.

1. Introduction

As the world economy grows, so does the population, and energy demand is increasing. In order to meet human needs, the intensity of energy development is also increasing, which will inevitably have many negative impacts on the ecological environment [1]. For example, the impact of oil sands mining on the environment has always been a serious problem, mainly as follows: (1) The mining of oil sands requires removal of surface vegetation to destroy the original forest ecosystem; (2) The hot washing of oil sands requires a lot of water resources; (3) The oil sands mining process has adverse effects on the atmospheric environment.

Oil sands resources in Alberta province are mined mainly by open-air and gas injection mining according to the depth. In the process of gradually opening this, it

*Corresponding Author:
Debo Chen,
College of Earth Sciences, Jilin University, Changchun, Jilin, China;
Email: 591022245@qq.com

DOI: https://doi.org/10.30564/jees.v4i2.4687

has brought many effects to the mining area and its surrounding environment and ecology, such as air pollution, massive damage of vegetation forest, vegetation health damage, and regional temperature rise, etc. Among them, vegetation is an important indicator in ecological environment monitoring [2]. Besides, an important goal of monitoring vegetation status is to provide data to assess and predict the effects of the combined effects of various factors. The long-term impact on an ecosystem is caused not only by mining areas, but also by their combined effects [3]. Remote sensing technology has the advantages of speed, accuracy and economy in obtaining large-scale and periodic land, ocean and atmospheric data, the access to land and high-level technical means to obtain information also play an important role in vegetation research [4,5]. Therefore, in this study, USGS Landsat-5 TM and Landsat-8 OLI remotely sensed images were used as the basic data sources; three vegetation indexes (NDVI, NDMI and RVI) of Alberta oil sand mining area from 1995 to 2020 are processed and output to explore the long-term impact of the vegetation in the mining area and its surrounding areas.

2. Materials and Methods

The time series of this paper spans 25 years from 1995 to 2020. Landsat-5 TM and Landsat-8 OLI/TIRS remote sensing data are used according to the year basic data source. Landsat-8 OLI/TIRS remote sensing data are used for 2015 and 2020 data, and Landsat-5 TM remote sensing data are used for other time nodes. Landsat images covering the study area in summer of 1995, 2000, 2005, 2010, 2015 and 2020 are obtained from these data sources. The spectral values of the images are functions of the current phenological conditions, especially for broad-leaved forest ecosystems. In order to limit the impact, we choose the image time to tilt up in the same season [6]. All image requirements are of high quality and have little cloud or mist to hinder the atmosphere.

This paper selects remote sensing geological images of Alberta province from 1995 to 2020 to understand the changes of the research area and the development and mining process of the mining area in 25 years. Among them, Landsat-5 TM data from 1995, 2000, 2005 and 2010 were used before 2013, while Landsat-8 TM/OLI data could be used in 2015 and 2020. The remote sensing image data involved in this paper are detailed in Table 1. All of the data were preprocessed.

3. Study Area

The northeastern Alberta province has a storage area of about 14,000 square kilometers, the world's second largest oil store in the world after Saudi Arabia. This paper selects the core area of oil sand mining area, and the land area is about 4687 square kilometers. The three main areas of oil sands in Alberta province are Athabasca, Cold Lake and Peace River. About 80% of the available asphalt is located in the Athabasca oil sands mine [7].

3.1 Geographic Settings

The geographical area of the Alberta is located at 57°-58°N, 111°-112°W. As Figure 1 shows, Alberta Province is located in the west of Canada, and the oil sands deposit is the largest around the world [8]. The three main areas of the Alberta oil sands are Athabasca, Cold Lake and Peace River. Athabasca is the largest and most widely developed region in the world [9].

Table 1. Remote sensing image data in the study area.

Satellite name	Date	Time	Cloud	Latitude	Longitude
Landsat-8	20200818	18:34	0.36	57°19'18.62"N	112°18'23.91"W
Landsat-8	20150602	18:33	0	57°19'16.27"N	112°02'23.36"W
Landsat-5	20100722	18:24	9	57°19'24.31"N	111°16'25.33"W
Landsat-5	20050530	18:15	0	57°19'19.81"N	111°14'17.02"W
Landsat-5	20000615	18:06	0	57°19'22.41"N	111°23'34.37"W
Landsat-5	19950804	17:29	0	57°19'19.34"N	111°02'38.12"W

Figure 1. Map of Alberta Province, Canada [10].

3.2 Geologic Settings

The study area is located in the Alberta province of western Canada, and its main oil sands resources are distributed in the Western Canada Basin, occurring in the lower Cretaceous Mannville group McMurray formation Wabisca member, belonging to the typical craton basin. Alberta basin tectonic evolution overall is the passive continental edge stage-early orogenic stage-foreland basin stage-orogenic zone landform formation stage. The mining of oil sand mining area mainly consists of three parts, specifically, Athabasca oil sand mining area, Cold Lake oil sand mining area and Peace River oil sand mining area. Among them, Athabasca oil sand mining area is the largest in scale.

3.3 Oil Sands

Oil sands are oil-soaked rock, because it contains natural asphalt sand or other rock, so also called asphalt sand. It contains two main meanings: one is the mixture of oil in sand and other rock-forming minerals; the other is the crude oil in the blend [11]. When indicating this meaning, oil sands and asphalt sands are the same [12]. The first project in the world was processed by Great Oil Sands Company, which was licensed to operate the oil sands as early as 1964. But because the technology was relatively backward, mining capacity was limited. Until the 1990s as oil sands resources were paid more and more attention [13], conventional oil and gas had not met the needs of human, because of the innovation of oil sands mining technology, Alberta province gradually established a perfect oil sands open pit mining process.

The current more used mature mining methods include open pit mining and in-situ mining [14], which mining method mainly depends on the depth of oil sands deposit. Generally speaking, buried less than 75 meters using open pit mining, buried more than 75 meters of oil sand ore belt needs to peel off the thick cover layer and often use in-situ mining [15].

For Alberta province oil sand mining area, the open-pit mining method is mainly used in the early stage of mining, and the surface oil sand mine is mined in the simplest way. With the mining, to obtain a deep layer of oil sand ore resources, it is necessary to combine the in-situ mining method.

4. Methodology

4.1 Method of Vegetation Change

In order to compare the changes of land vegetation area around Alberta oil sands mining area from 1995 to 2020, we adopted the supervised classification method in ENVI to judge the types of land cover in the study area according to previous research results and prior knowledge, which can be divided into five parts: vegetation, water body, settling ponds, oil sands mine and other land types. Images of vegetation areas circled by Region of Interest (ROI) in Figure 2.

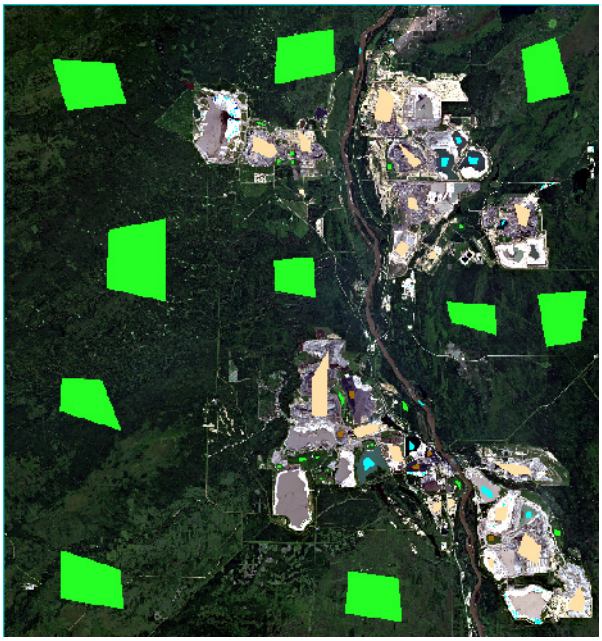

Figure 2. Visual interpretation of the study area.

We used Support Vector Machine (SVM) classification, which is a machine learning method based on Statistical Learning Theory. SVM can automatically find those support vectors that have a large discriminative ability for classification, thus constructing a classifier that can maximize the interval between classes. Therefore, it has good generalization and high classification accuracy.

4.2 Method of Spatiotemporal Variations

The most common method in the application of the vegetation index is to combine the reflectance of the wavelength with the characteristics of the vegetation [16]. The health of vegetation can be assessed by analyzing different vegetation indices, and then assess the environment [17]. Vegetation coverage can be fully reflected by the NDVI and other vegetation indexes inverted by the remotely sensed image, and is positively associated with them. Generally speaking, the better the vegetation coverage, the greater the vegetation index NDVI and RVI values, and then explore the vegetation water changes around the oil sands mining area combined with the NDMI value [18]. To clearly reflect the changes in vegetation cover in the oil sands area, we used the computer statistics tool in ENVI software to derive mean NDVI, NDMI and RVI values.

4.2.1 Normalized Vegetation Index (NDVI)

NDVI is defined as the difference between the reflectance of NIR band and visible red band divided by the sum of the reflectance of the two bands. For Landsat 8 OLI data [19], the calculation formula of NDVI is as follows:

$$NDVI = \frac{b_4 - b_5}{b_4 + b_5} \quad (1)$$

b_4 and b_5 are the reflectance of band 4 and band 5 of Landsat 8 OLI, respectively. The value of NDVI is in the range of [–1, 1]. Generally, the value of NDVI in non-vegetative areas (bare, aquifer, etc.) is low or negative, so is the city. The NDVI value of cultivated land and forest land with high vegetation coverage is higher [20]. NDVI can partially remove or weaken the influence of satellite observation angle, solar elevation angle, topographic relief, a small amount of cloud shadow and atmospheric radiation on the imaging [21]. Therefore, NDVI is widely used in vegetation research based on remote sensing images, and it is the best indicator of plant growth and coverage.

4.2.2 Normalized Vegetation Water Index (NDMI)

Due to the influence of water absorption band in mid-infrared band, vegetation index NDMI is very sensitive to humidity and water content information, and has a strong reflection on vegetation leaves in near infrared band. Therefore, NDMI is highly related to water content of vegetation (especially canopy and stem), which has been widely used in environmental protection and agricultural production, especially in the monitoring of surface humidity and crop growth [22]. The calculation formula of NDMI is as follows:

$$NDMI = \frac{b_5 - b_6}{b_5 + b_6} \quad (2)$$

b_5 and b_6 are the reflectance of band 5 and band 6 of Landsat 8 OLI, namely, the reflectance of near infrared and short wave infrared.

4.2.3 Ratio Vegetation Index (RVI)

As the vegetation coverage in the study area is generally high, RVI is more sensitive to the vegetation coverage area than other vegetation indexes, and has the best correlation with biomass. The RVI is the ratio of near infrared band (NIR) to visible red band (R):

$$RVI = \frac{b_5}{b_4} \quad (3)$$

b_4 and b_5 are the reflectance of band 4 and band 5 of Landsat 8 OLI, respectively. The range of RVI value is 0 - 30, the range of general green vegetation area is 2 - 8, and the RVI value of non-vegetation covered ground (mining land, water body, tailings pond, oil sand mine, etc.) is near 1. RVI has a high correlation with Leaf Area Index (LAI), leaf dry biomass and chlorophyll content, and is often used to analyze and estimate the vegetation coverage. The relationship between RVI and vegetation coverage is as follows: in areas with high vegetation coverage, vegetation has a great influence on RVI; in areas with low vegetation coverage, vegetation has little influence on RVI. In addition to the influence of vegetation coverage, atmospheric conditions also affect the RVI value, hence the remote sensing data can only be solved after atmospheric correction to obtain more accurate RVI value [23].

5. Result and Discussion

5.1 Results of Vegetation Change

The changing analysis of vegetation area is as follows:

(1) 1995

Figure 3 shows the interpretation image of the study area in 1995, and the changes of each type of areas are shown in Table 2. Most of the study area is covered by vegetation, and only Cold Lake oil sand mining area has been developed very much. Vegetation accounts for

95.636% of the whole area, water body accounts for 0.688%, settling ponds accounts for 0.247%, oil sand mine accounts for 0.021%, and other land types account for 3.408% of the total area. The area of vegetation removal in the study area is about 204.54 square kilometers, and the vegetation area is about 4482.46 square kilometers. In summary, the original landform is well preserved, and the impact of oil mining on the environment is limited.

(2) 2000

Figure 4 is the land cover image of the oil sand mining area in 2000, and the data of each type of areas are shown in Table 3. Athabasca oil sand mining area has been preliminarily developed, and Cold Lake oil sand mining area has become a new extended oil mine in the east part of the original mining area. The vegetation area accounts for 93.373% of the total area, water body accounts for 0.910%, settling ponds accounts for 0.713%, oil sand mine accounts for 0.032%, and other land types in the mining area account for 4.972%. The area of vegetation is 4376.39 square kilometers, which is 106.07 square kilometers less than that in 1995; the vegetation coverage rate in the study area is 93.373%, which is 2.263% less than that in 1995. Thus, the exploitation of oil sand mining area in Alberta province increased from 1995 to 2000, and new oil sand mining area was developed.

(3) 2005

Figure 5 is the interpretation image of the study area in 2005, and the data of specific mining area are shown in Table 4. During the period from 2000 to 2005, Athabasca oil sand mining area ushered in the peak period of mining, and Cold Lake oil sand mining area has also been widened very much. The vegetation area decreased from 93.373% in 2000 to 89.597%, the water area decreased from 0.910% in 2000 to 0.721%, the settling ponds increased from 0.713% in 2000 to 0.923%, and the oil sand mine increased from 0.032% in 2000 to 0.123%. During this period, with the development of the oil sand mine, a large number of vegetation continued to be removed, and the area of the oil sand mine doubled.

(4) 2010

Figure 6 is the interpretation image of the study area in 2010, and the changes of each type of areas are shown in Table 5. Compared with 2005, Athabasca has developed a new mining area in the east part of the original mining area, Cold Lake has basically completed the mining work, and Peace River has been opened up in the northwest of the study area. The proportion of vegetation area decreased from 89.597% in 2005 to 85.367%, water area increased from 0.721% to 0.833%, settling ponds increased from 0.923% to 1.459%, and oil sand mine increased from 0.123% to 0.206%.

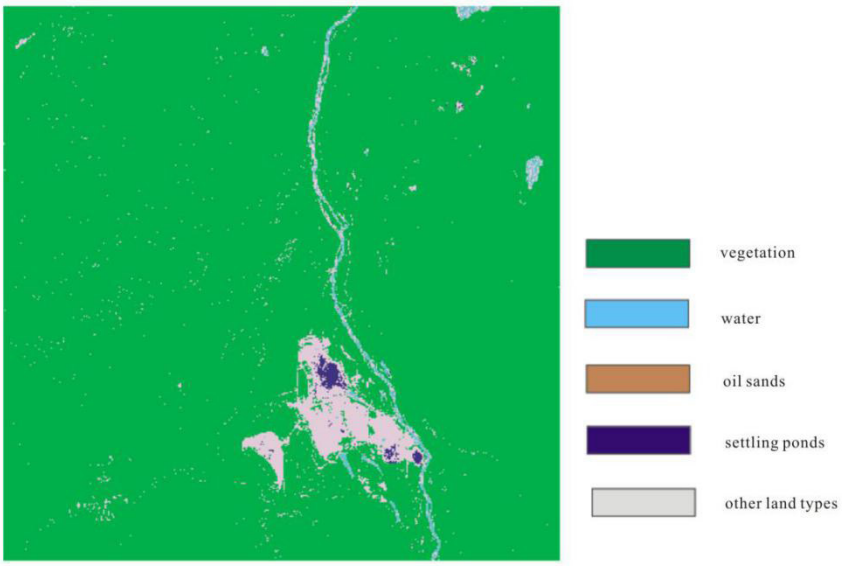

Figure 3. Land cover map of Alberta oil sand mining area in 1995.

Table 2. Areas of each type of Alberta oil sand mining area in 1995.

Land use types	Vegetation	Water	Oil sands	Settling ponds	Other land types	Total
The measure of area/km²	4482.46	32.25	0.98	11.58	159.73	4687
Proportion/%	95.636%	0.688%	0.021%	0.247%	3.408%	100%

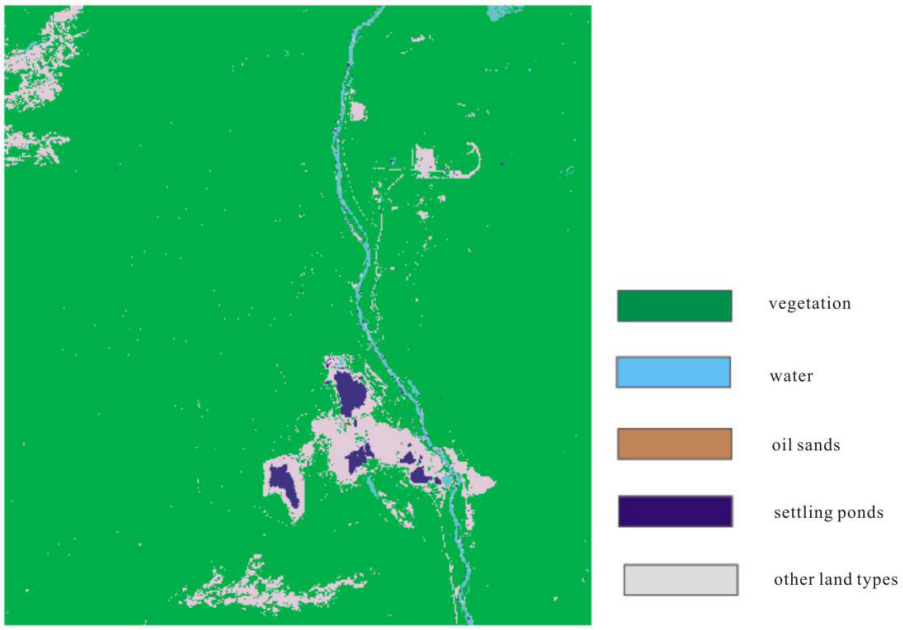

Figure 4. Land cover map of Alberta oil sand mining area in 2000.

Table 3. Areas of each part of Alberta oil sand mining area in 2000.

Land use types	Vegetation	Water	Oil sands	Settling ponds	Other land types	Total
The measure of area/km²	4376.39	42.65	1.50	33.42	233.04	4687
Proportion/%	93.373%	0.910%	0.032%	0.713%	4.972%	100%

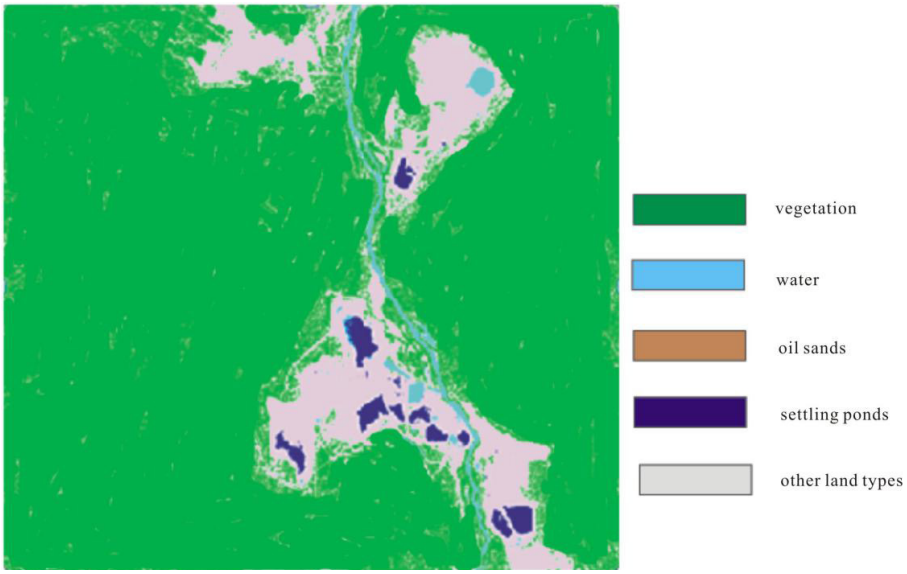

Figure 5. Land cover map of Alberta oil sand mining area in 2005.

Table 4. Area of each type of Alberta oil sand mining area in 2005.

Land use types	Vegetation	Water	Oil sands	Settling ponds	Other land types	Total
The measure of area/km²	4199.41	33.79	5.76	43.26	404.77	4687
Proportion/%	89.597%	0.721%	0.123%	0.923%	8.636%	100%

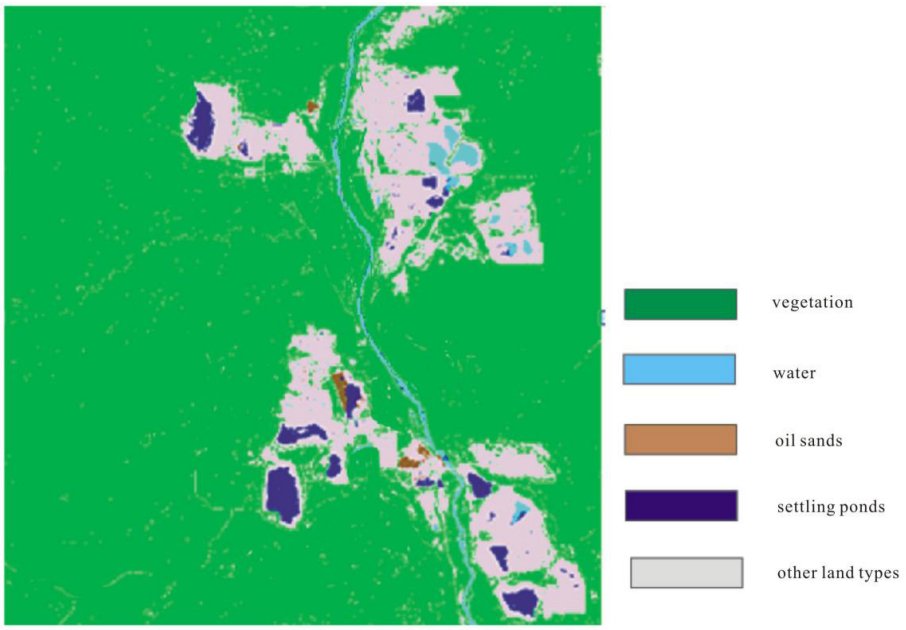

Figure 6. Land cover interpretation map of Alberta oil sand mining area in 2010.

Table 5. Area of each part of Alberta oil sand mining area in 2010.

Land use types	Vegetation	Water	Oil sands	Settling ponds	Other land types	Total
The measure of area/km²	4001.15	39.04	9.66	68.38	568.77	4687
Proportion/%	85.367%	0.833%	0.206%	1.459%	12.135%	100%

(5) 2015

Figure 7 is the interpretation image of the study area in 2015, and the changes of specific mining area are shown in Table 6. Athabasca continued to develop, but the growth rate of Cold Lake slowed down from 2010 to 2015. The proportion of vegetation changed from 85.367% to 82.982%, water area increased from 0.833% to 0.964%, settling ponds increased from 1.459% to 1.513%, and oil sand mine increased from 0.206% to 0.234%.

(6) 2020

Figure 8 is the interpretation image of the study area in 2020, and the changes of each mining area are shown in Table 7. The areas of the three oil sand mining areas tend to be stable from 2015 to 2020, with less mining and less change in other land use areas. The proportion of vegetation in the whole study area decreased from 82.982% to 82.672%, the water area increased from 0.964% to 0.973%, the area of settling ponds increased from 1.513% to 1.521%, and the area of oil sand mine increased from 0.234% to 0.243%. The overall area of each type of the oil sand mining area changes very little and the overall environment of the mining area tends to be stable.

In summary, from 1995 to 2020, the proportion of vegetation decreased from 95.636% to 82.672%; water body increased from 0.688% to 0.973%; settling ponds increased from 0.247% to 1.521%; oil sand mine increased from 0.021% to 0.243%; other land use types increased from 3.408% to 14.591%. Only vegetation was reduced in the whole study area, and the removed vegetation was developed into settling ponds, oil sand mine, and so on. The change of the proportion of each land type in 25 years is shown in Figure 9.

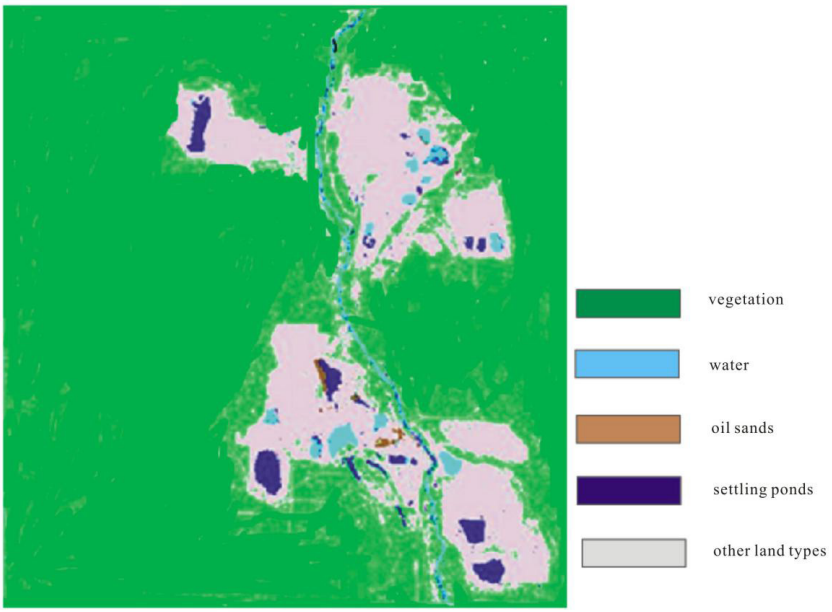

Figure 7. Land cover interpretation map of Alberta oil sand mining area in 2015.

Table 6. Areas of each type of Alberta oil sand mining area in 2015.

Land use types	Vegetation	Water	Oil sands	Settling ponds	Other land types	Total
The measure of area/km²	3889.94	45.18	10.97	70.91	670.57	4687
Proportion/%	82.982%	0.964%	0.234%	1.513%	14.307%	100%

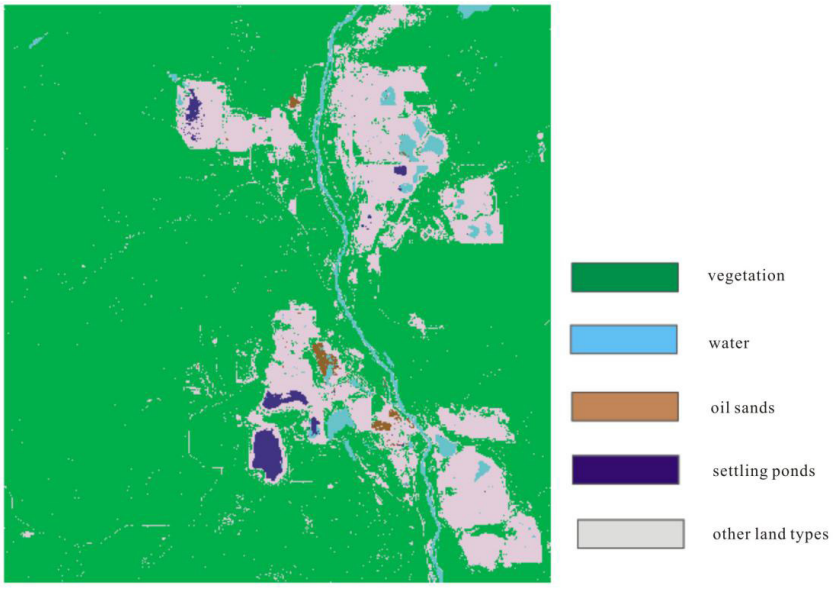

Figure 8. Land cover interpretation map of Alberta oil sand mining area in 2020.

Table 7. Area of each part of Alberta oil sand mining area in 2020.

Land use types	Vegetation	Water	Oil sands	Settling ponds	Other land types	Total
The measure of area/km²	3874.84	45.60	11.39	71.29	683.88	4687
Proportion/%	82.672%	0.973%	0.243%	1.521%	14.591%	100%

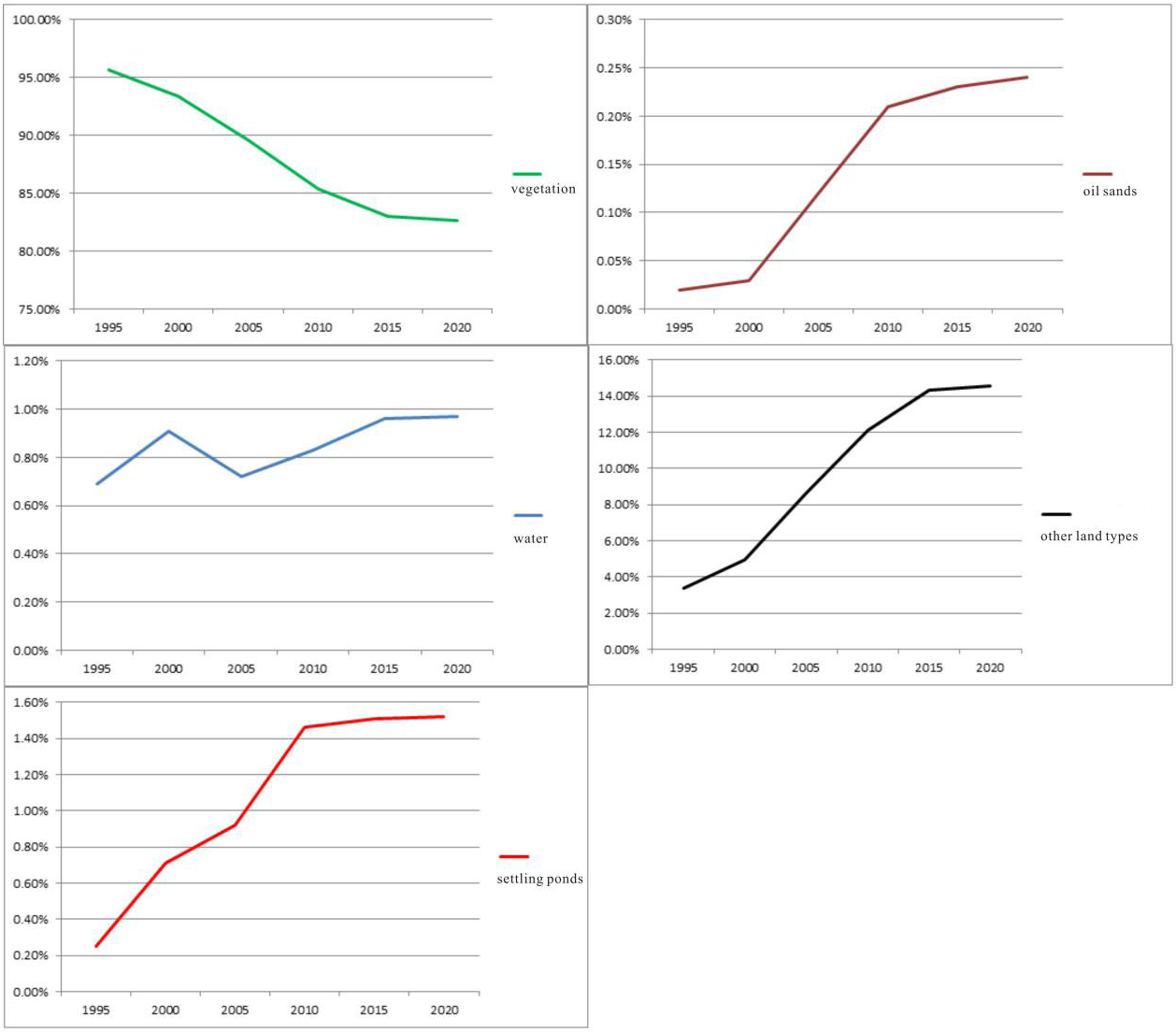

Figure 9. Proportion of different land types from 1995 to 2020.

From Figure 9, it can be seen that the proportion of vegetation in the study area decreases gradually from 1995 to 2020; the proportion of settling ponds, oil sand mine and other land types in the mining area shows an upward trend; the proportion of water body fluctuates up and down. Especially in 2000-2015, the change is particularly obvious, which indicates that the development and mining of oil sand mining area ushered in the peak during this period. In 2015-2020, the change of land cover type in the study area has been basically completed, and the change of land type is smaller than that in previous periods.

In order to show the change of vegetation in the study area from 1995 to 2020 more intuitively, we classify the land except vegetation as the area of oil sand mining area. The vegetation area of the study area was 4482.46 square kilometers in 1995, 4376.39 square kilometers in 2000, 4199.41 square kilometers in 2005, 4001.15 square kilometers in 2010, 3889.94 square kilometers in 2015 and 3874.84 square kilometers in 2020. The proportion of vegetation coverage is from 95.64% in 1995, 93.37% in 2000, 89.60% in 2005, 85.37% in 2010, 82.98% in 2015 to 82.67% in 2020. Figure 10 depicts the change of vegetation proportion in the study area from 1995 to 2020. From the result, it can be observed that the vegetation coverage in the oil sand mining area decreased more from 2000 to 2015, with a total of 375.24 square kilometers less. The vegetation proportion in the study area changed less from 1995 to 2000 and from 2015 to 2020.

From the above, we can obtain the results as follows:

(1) From 1995 to 2000 and from 2015 to 2020, the proportion of vegetation in and around the oil sand mining area changed little; from 2000 to 2015, with the peak period of oil sand mining area development, a large number of vegetation in the study area was removed, and the pro-

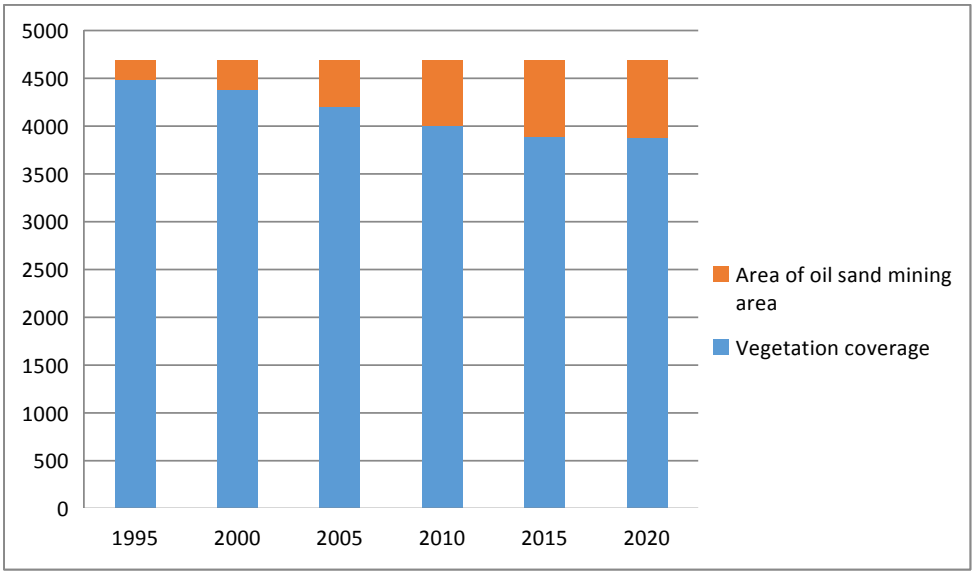

Figure 10. The change of vegetation areas from 1995 to 2020.

portion of vegetation decreased rapidly.

(2) The proportion of vegetation in the study area showed a downward trend; the proportion of settling ponds, oil sand mine and other land types in the mining area showed an upward trend; the proportion of water body fluctuated up and down. Especially in 2000-2015, this change is particularly obvious. During the period of 2015-2020, the development of oil sand mining area is basically completed, and the change of vegetation proportion in the study area is very small.

(3) From 1995 to 2020, only vegetation was reduced in the study area, and the original vegetation land was converted to tailings pond, oil sand mine and other land types in the mining area.

5.2 Results of Spatiotemporal Variations

The followings are the long-time change characteristics and analysis of the three vegetation indexes in the study area from 1995 to 2020.

5.2.1 Normalized Vegetation Index (NDVI)

Six remotely sensed images from 1995 to 2020 in Alberta oil sand mining area were preprocessed, parameter band operation and vegetation index were calculated, and the distribution maps of NDVI and time correlation index of oil sand mining area in 1995, 2000, 2005, 2010, 2015 and 2020 were obtained as shown in Figures 11-16.

According to the image analysis, the NDVI value in the north of the study area generally increased and the vegetation coverage increased from 1995 to 2000, while the NDVI value in the mining area decreased due to the development; with the rapid development of new mining areas from 2000 to 2005, 2005 to 2010 and 2010 to 2015, the NDVI value in the newly developed mining area de-

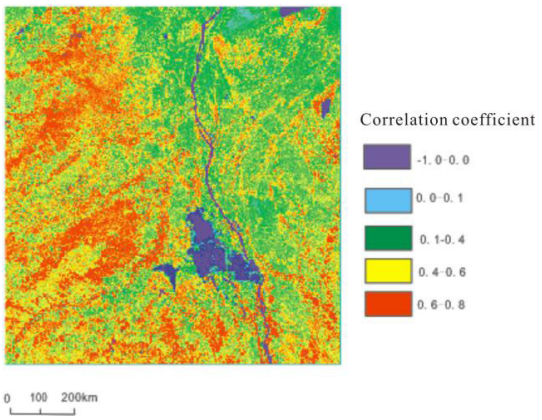

Figure 11. NDVI map in 1995.

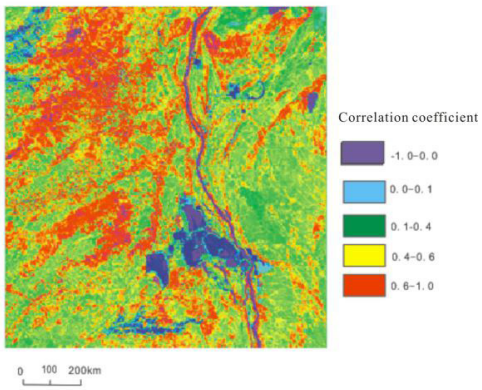

Figure 12. NDVI map in 2000.

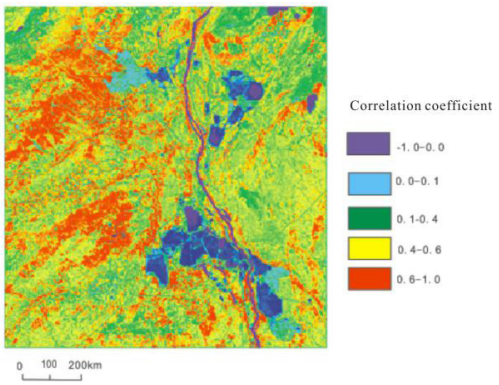

Figure 13. NDVI map in 2005.

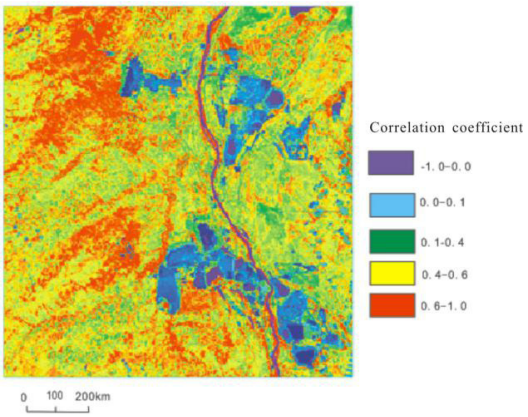

Figure 14. NDVI map in 2010.

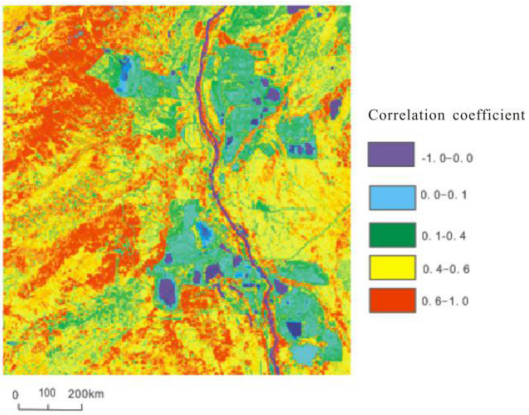

Figure 15. NDVI map in 2015.

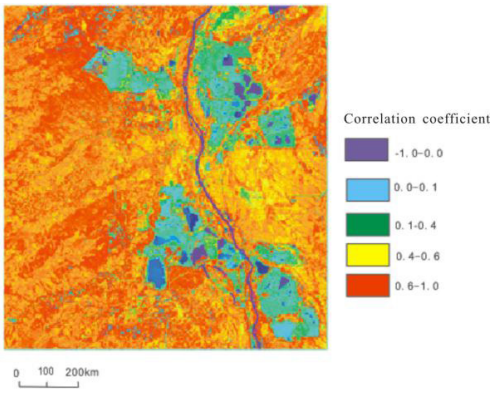

Figure 16. NDVI map in 2020.

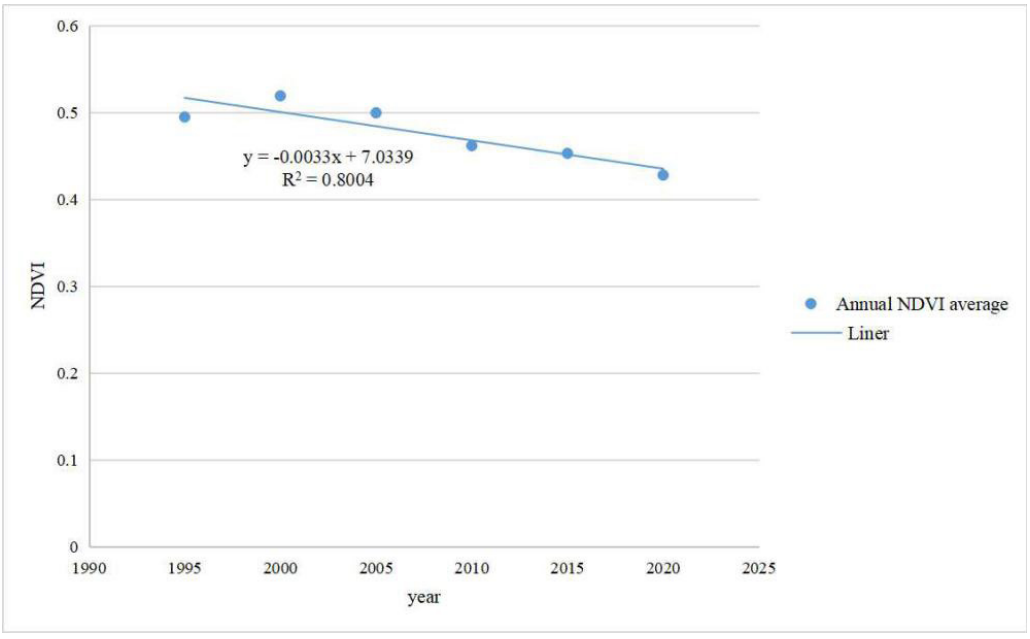

Figure 17. Change of NDVI mean values from 1995 to 2020.

creased and the vegetation was removed; the mining area was basically completed from 2015 to 2020, Combined with the policies of the local government of Canada, the forest around the oil sand mine is effectively protected, and the overall NDVI value around the mining area becomes larger. In order to further study the long-term correlation of NDVI value in the study area from 1995 to 2020, the average NDVI value in the study area is obtained by using the tool of compute statistics in ENVI software, and a long-term trend is observed. Figure 17 is the correlation between NDVI value and the related years. It can be clearly observed that the NDVI average value of the study area is decreasing from 1995 to 2020.

5.2.2 Normalized Vegetation Water Index (NDMI)

The distribution of NDMI and time correlation index in 1995, 2000, 2005, 2010, 2015 and 2020 are obtained by using band math tool after pretreatment and error elimination, which is the same as NDVI part (Figures 18-23).

From the above figures, it can be clearly observed that

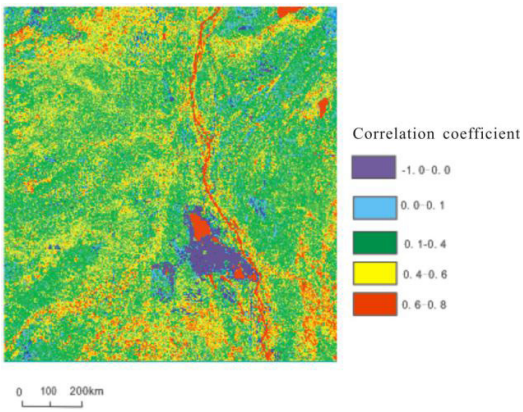

Figure 18. NDMI map in 1995.

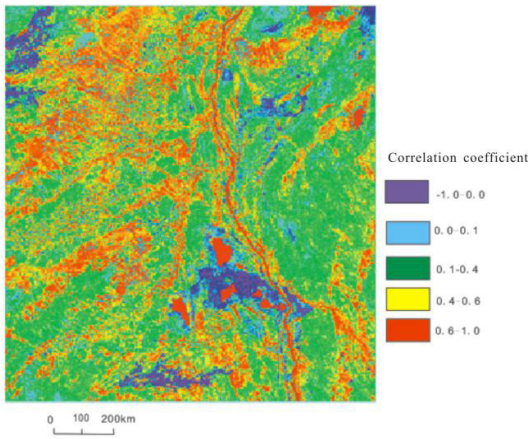

Figure 19. NDMI map in 2000.

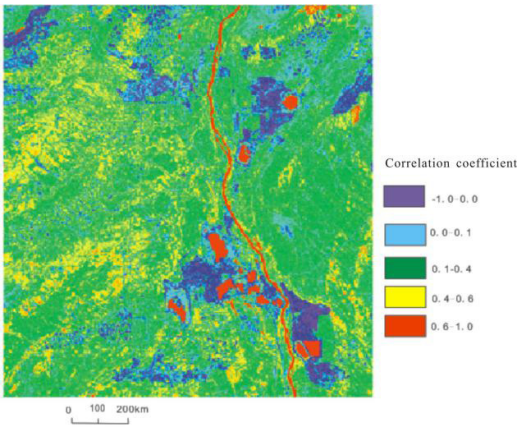

Figure 20. NDMI map in 2005.

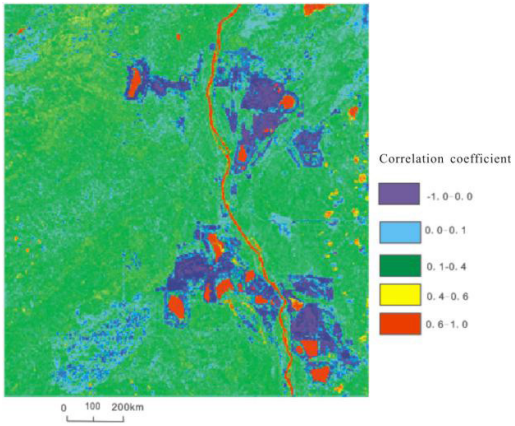

Figure 21. NDMI map in 2010.

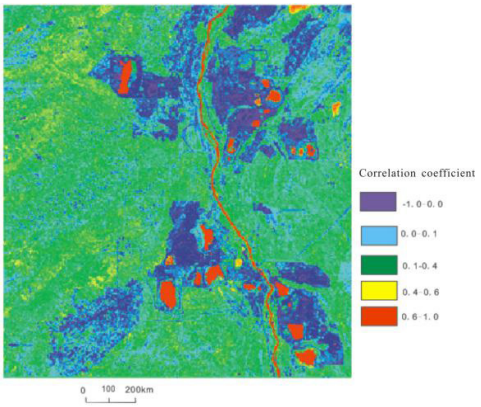

Figure 22. NDMI map in 2015.

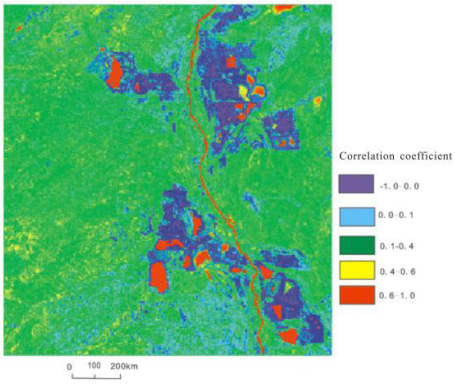

Figure 23. NDMI map in 2020.

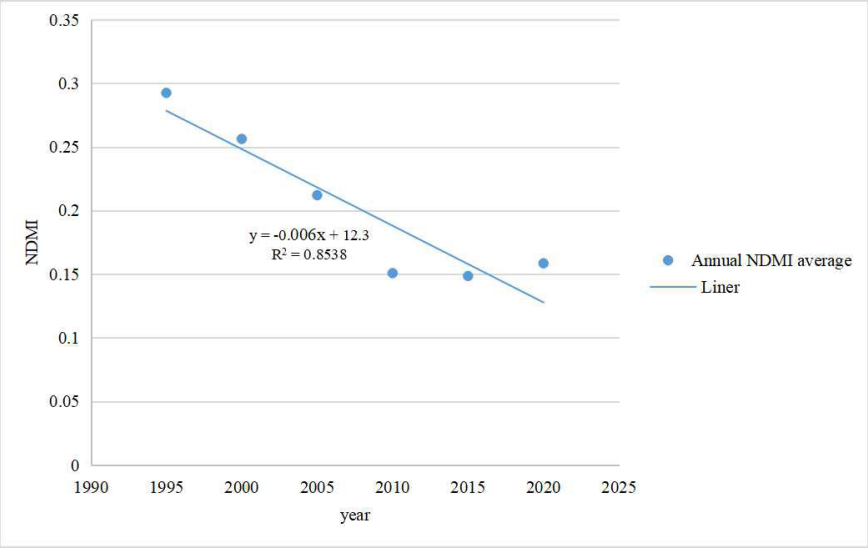

Figure 24. Change of NDMI mean values from 1995 to 2020.

there were more yellow and red in the forest area in 1995 and 2000, which proved that the NDMI value was larger and the water content of vegetation was higher in this period; 2000-2015 was the most rapid stage of the mining area, and in 2005, there were some yellow areas and some green areas in the forest area. In 2010, 2015 and 2020, most of the forest areas are green, and the NDMI value is small. Combined with the change of NDVI value in the previous part, it fully shows that with the development and mining of the mining area, although the vegetation coverage rate outside the mining area is still high, the water content of vegetation decreases seriously, and the health status of vegetation is greatly affected. In addition, because there are sand settling ponds and water bodies in the mining area, there are large red areas in the mining area from the images, and the NDMI value is high.

In order to further study a correlation of long-term changes of NDMI value from 1995 to 2020, the average NDMI value of the study area is obtained by using the tool of compute statistics in ENVI classic, and a long-term trend is observed. Figure 24 is the correlation between NDMI value and the related years. It can be clearly observed from the images that the average NDMI of the study area is decreasing from 1995 to 2020, especially from 1995 to 2010.

5.2.3 Ratio Vegetation Index (RVI)

After preprocessing and error elimination, band math tool is used to calculate the RVI and time correlation index distribution in 1995, 2000, 2005, 2010, 2015 and 2020 (Figures 25-30).

In order to further study the long-term change of RVI

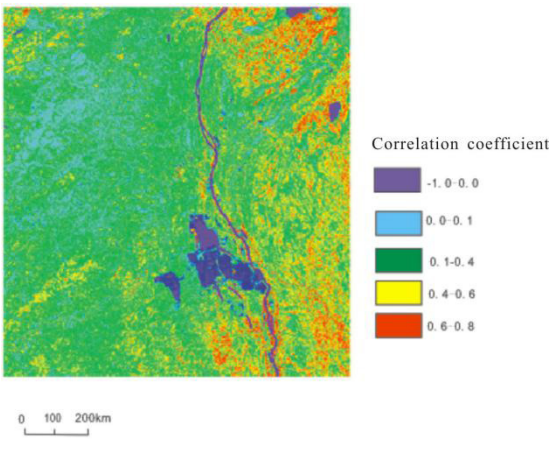

Figure 25. RVI map in 1995.

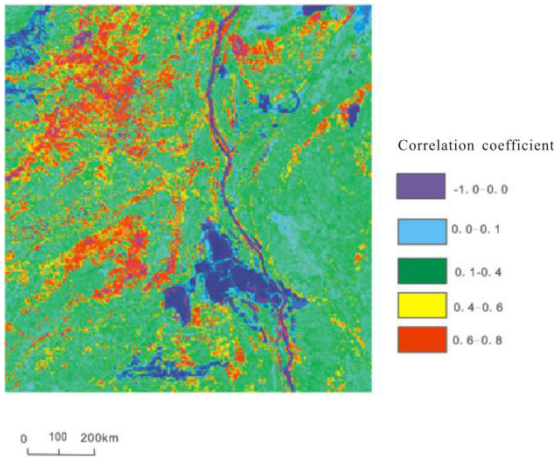

Figure 26. RVI map in 2000.

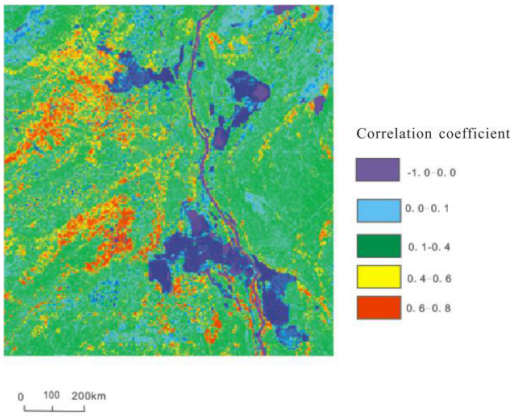

Figure 27. RVI map in 2005.

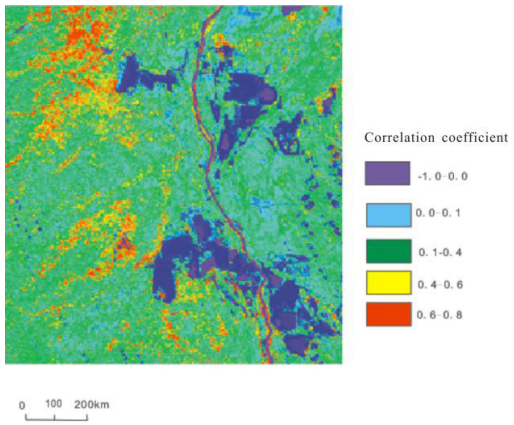

Figure 28. RVI map in 2010.

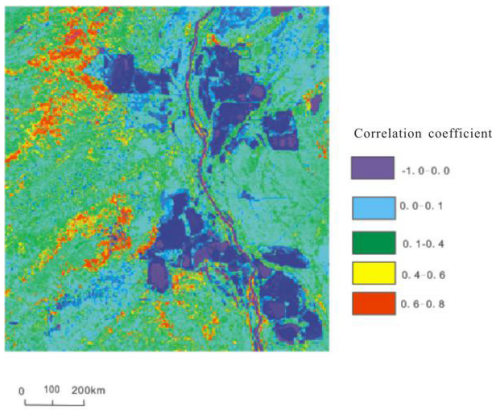

Figure 29. RVI map in 2015.

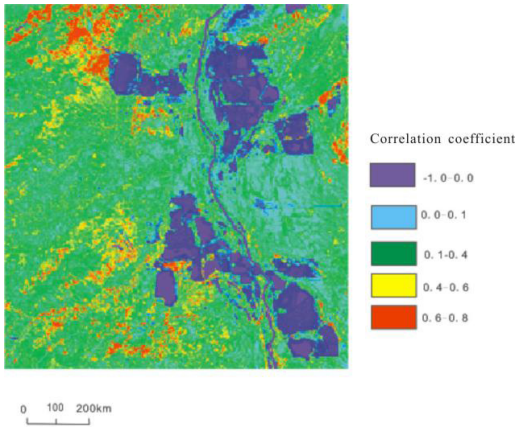

Figure 30. RVI map in 2020.

value in the study area from 1995 to 2020, the average RVI value is obtained by using compute statistics tool in ENVI software and a long-term trend is observed. As shown in Figure 31, the relationship between RVI value and the related years is shown. It can be clearly observed from the images that the RVI mean in the study area is decreasing from 1995 to 2020.

Finally, in order to understand the changes of three indexes in 25 years and the impact of development and exploitation of oil sand mining area on the environment (especially on vegetation), we list the average annual mean of three vegetation indexes (NDVI, NDMI and RVI) in Table 8.

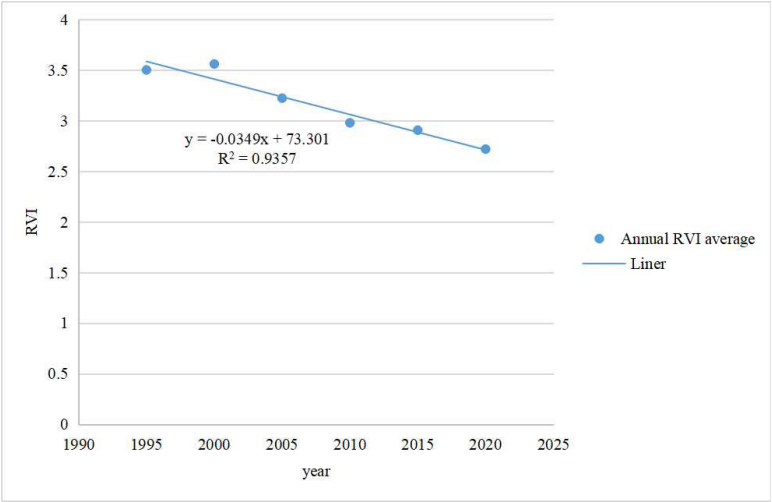

Figure 31. Annual variation of RVI mean values from 1995 to 2020.

Table 8. Corresponding lists of years and vegetation indexes.

Indexes \ Years	1995	2000	2005	2010	2015	2020
NDVI	0.494788	0.519125	0.499578	0.461666	0.452805	0.427828
NDMI	0.292505	0.256337	0.212075	0.150779	0.148542	0.158529
RVI	3.501492	3.559949	3.222617	2.979133	2.9065	2.71917

The results can be obtained from the above:

(1) From 1995 to 2020, with the development and exploitation of oil sand mining area in Alberta, the three vegetation indexes (NDVI, NDMI and RVI) showed a downward trend.

(2) From 2000 to 2010, the development of oil sand mining area is the fastest, and the corresponding vegetation index is also the fastest decline, especially RVI.

(3) From 1995 to 2005, the decrease of NDMI was much faster than that of NDVI, indicating that the development and exploitation of the mining area had a significant impact on the vegetation water content.

(4) The changes of NDVI and RVI are very similar, NDMI decreased significantly from 1995 to 2010, and tended to be stable from 2010 to 2020. It shows that the vegetation coverage decreased in the early mining period from 1995 to 2010, and the vegetation water content also decreased rapidly; after 2010, with the gradual improvement of mining area development, the vegetation coverage decreased slowly, and the change of NDMI tended to be stable.

6. Conclusions and Future Directions

Through the processing of USGS Landsat-5 TM and Landsat-8 OLI remotely sensed images, the distribution of vegetation in and around Alberta oil sand mining area and the long-term changes of three vegetation indexes (NDVI, NDMI and RVI) in 1995, 2000, 2005, 2010, 2015 and 2020 were obtained. Several conclusions and suggestions can be drawn as follows:

(1) The proportion of vegetation in the study area decreased sharply from 1995 to 2020, and the scale of construction land in the mining area increased. The development of the mining area led to the reclamation of vegetation and the proportion of vegetation decreased. Especially in 2000-2015, the period is the fastest stage for oil sand development; from 1995 to 2000, the development of oil sand mining area is slow, while that of Cold Lake oil sand mine increases slightly, and the development of Athabasca oil sand mine is just in the initial stage; from 2015 to 2020, the development of oil sand mining area is basically bound, which mainly involves mining and vegetation protection around the study area.

(2) From 1995 to 2020, with the development and exploitation of oil sands mining area in Alberta, the NDVI, NDMI and RVI are all declining. The period of 2000-2010 is the fastest stage of development of oil sand mining area, and the corresponding vegetation index is also the fastest, especially RVI. The decrease of NDMI in 1995-2005 was much faster than NDVI, which indicated that the development and exploitation of the mining area had a significant impact on vegetation water content. NDVI and RVI are similar in trend, and NDMI has declined significantly from 1995 to 2010, and tends to be stable from 2010 to 2020. It shows that the vegetation coverage decreased in the early mining period from 1995 to 2010, and the vegetation water content also decreased rapidly; after 2010, with the gradual improvement of mining area development, the vegetation coverage decreased slowly, and the change of NDMI tended to be stable.

(3) The Canadian government took some protection measures around 2015. While the oil sand mining area continues to start, the protection of vegetation around the study area is increased. It can be proved from the analysis of vegetation indexes. In 2015-2020, due to the implementation of various environmental protection, the vegetation coverage rate is basically unchanged, and NDMI even rises slightly, thus the vegetation protection has achieved initial results. Although the exploitation of oil sand mining area can bring great economic benefits, the environmental protection (especially vegetation) in and around oil sand mining area should be paid more attention.

Conflict of Interest

Authors declare no conflict of interests.

Acknowledgments

This research work was supported by the National Key Research and Development Program of China (No. 2020YFA0714103), China Scholarship Council (No. CSC201906175002) and the Young Teachers and Stu-

dents' Cutting-edge Funding of Jilin University, China (No. 2020-JCXK-04). We also thank the anonymous reviewers for their helpful suggestions.

References

[1] Salehi, E., Save, S., Almquist, G., et al., 2016. Fueling Alberta Oil Sands Fleets with Natural Gas [Internet]. Available from: https://www.hydrocarbonprocessing.com/magazine/2016/january-2016/special-report-lng-ngl-and-alternative-feedstocks/fueling-alberta-oil-sands-fleets-with-natural-gas

[2] Zheng, Q.Q. Landscape distribution and biomass estimation of caragana intermedia plantation in Yanchi Desert steppe based on remote sensing technology. Ningxia University. (In Chinese)

[3] Crerar, E.E., Arnott, R.W.C., 2007. Facies distribution and stratigraphic architecture of the lower cretaceous McMurray Formation, Lewis Property, northeastern Alberta. Bulletin of Canadian Petroleum Geology. 55(2), 99-124.

[4] Feng, Zh.F., Wang, Zh.X., Yue, J., et al., 2016. Research on the sensitive band selection of discrimination of non-timber product tree species surrounding Tarim Basin in Southern Xinjiang based on hyperion lmage. Forest Engineering. 32(2), 7. (In Chinese)

[5] Natcher, D., Brunet, N., Bogdan, A.M., et al., 2020. Seeking indigenous consensus on the impacts of oil sands development in Alberta, Canada. The Extractive Industries and Society. 7(4).

[6] Han, K.X., 2020. Study on surface temperature change of oil sand mining area in Alberta Province, Canada, 1990-2019. Jilin University. (In Chinese)

[7] Fernie, K.J., Marteinson, S.C., Chen, D., et al., 2018. Elevated exposure, uptake and accumulation of polycyclic aromatic hydrocarbons by nestling tree swallows (Tachycineta bicolor) through multiple exposure routes in active mining-related areas of the Athabasca oil sands region. Science of the Total Environment. 624, 250-261.

[8] Ma, F., Zhang, G.Y., Wang, H.J., et al., 2015. Potential, distribution and exploration trend of global heavy oil and oil sand resources. Journal of Jilin University (Earth Science Edition). (In Chinese)

[9] Walker, A., Waterfield, A., Roberts, S., 2010. Two dimensional ultrasound in clinical practice; a postal survey of consultant pediatric anesthetists in the United Kingdom—A reply. Pediatric Anesthesia. 17(10), 1006-1007.

[10] Willis, C.E., Louis, V.L.S., Kirk, J.L., et al., 2019. Tailings ponds of the Athabasca Oil Sands Region, Alberta, Canada, are likely not significant sources of total mercury and methylmercury to nearby ground and surface waters. Science of the Total Environment. 647, 1604-1610.

[11] Han, Zh.Q., 2011. The actuality and perspective study on the development and utilization of oilsands in Junggar basin, Xinjiang province. Nanjing Agricultural University. (In Chinese)

[12] Shan, X.L., Yang, L., Wang, P.J., 2006. Calculation of ordovician erosion thichness in eastern tarimu basin. Xinjiang Geology. 24(4), 3. (In Chinese)

[13] Verbeke, A., Osiyevskyy, O., Backman, C.A., 2017. Strategic responses to imposed innovation projects: The case of carbon capture and storage in the Alberta oil sands industry. Long Range Planning. 50(5), 684-698.

[14] Li, M.Y., 2014. The organic geochemical characteristics and reservoir forming pattern of palaeogene and neogene oil sands in Western Qaidam Basin. Chang'an University. (In Chinese)

[15] Tao, G.L., Tenger, Cao, T.T., et al., 2016. Resource evaluation method for open-pit mining oil sands in the Western Canada Basin, Canada. Bulletin of Mineralogy, Petrology and Geochemistry. (1), 5. (In Chinese)

[16] Zhang, X., Zhang, J.Q., Jin, W., et al., 2009. Improved method for retrieving remote sensing reflectance of ground targets from a spectral image. Acta Photonica Sinica. 038(005), 1221-1225. (In Chinese)

[17] Donovan, S.D., MacLean, D.A., Zhang, Y., et al., 2021. Evaluating annual spruce budworm defoliation using change detection of vegetation indices calculated from satellite hyperspectral imagery. Remote Sensing of Environment. 253, 112204.

[18] Latifovic, R., Pouliot, D., Olthof, I., 2017. Circa 2010 land cover of Canada: Local optimization methodology and product development. Remote Sensing. 9(11), 1098.

[19] Guo, Y.Ch., 2019. The influence of urban spatial morphology on thermal environment in Zhengzhou. Henan Agricultural University. (In Chinese)

[20] Li, B., Wang, H.M., Qin, M.Zh., et al., 2017. Comparative study on the correlations between NDVI, NDMI and LST. Progress in Geography. 36(05), 585-596. (In Chinese)

[21] Yang, L., Guan, Q., Lin, J., et al., 2021. Evolution of NDVI secular trends and responses to climate change: A perspective from nonlinearity and nonstationarity characteristics. Remote Sensing of Environment. 254, 112247.

[22] Nejad, M.F., Zoratipour, A., 2019. Assessment of LST and NDMI indices using MODIS and Landsat images in Karun riparian forest. Journal of Forest Science. 65(1), 27-32.

[23] Gao, Sh.F. Remote sensing alteration ex traction in Dexing porphyry copper deposits area of Jiangxi Province. Chang'an University. (In Chinese)

BILINGUAL PUBLISHING CO.
Pioneer of Global Academics Since 1984

Journal of Environmental & Earth Sciences
https://ojs.bilpublishing.com/index.php/jees

ARTICLE

Geotechnical Risk Assessment and Geological Origin of Building Fracturation in Agadez City (North Niger)

Baraou Idi Souley[1*] Abdoulwahid Sani[1] Abdoul Wahab Djibo Maïga[2] Moussa Konaté[3]

1. Department of Geology, University of Agadez, Agadez, Niger
2. High Authority for Atomic Energy of Niger (HANEA, Niger), OTICE, Niamey, Niger
3. Department of Geology, University of Niamey, Niamey, Niger

ARTICLE INFO

Article history
Received: 5 May 2022
Revised: 13 July 2022
Accepted: 20 July 2022
Published Online: 5 August 2022

Keywords:
Geotechnical risks
Geological origin
Buildings fracturation
Fractures
Cracks
Faults
Agadez city
Niger

ABSTRACT

The Agadez city is built on the faulted and fractured sandstone formation of the "Agadez Sandstones", which was deposited in unconformity on the Precambrian basement of the Aïr Mountain. The present study focuses on the geotechnical risk assessment and geological origin of building fracturation in Agadez city. A methodological approach integrating measurement of fractures planes affecting the buildings and their statistical analysis has been implemented. Statistical analysis of obtained data showed that in 100 fractured buildings, about 3% of buildings are at risk of collapse (very high risk), 64% of buildings are fractured (medium risk of collapse), and 34% of buildings are cracked (lower risk of collapse). These results showed as well that the nature of the material (rheology) influences the buildings fracturation. Indeed, buildings made from cement are more easily fractured than buildings made from clay materials. Statistical analysis of fracture planes reveals that the geotechnical risk associated with building's fracturation propagates in NW-SE, corresponding to the major directions of risk propagation, mainly dipping in northwest sectors (zones) of the Agadez city. The interpretation of geological and geophysical data combined with those obtained in the case of this study, reveals that the risk associated with buildings fracturation in Agadez city is caused by geological seismic events and or anthropogenic activities (explosive firing on the uranium mining sites like Somaïr and Cominak).

1. Introduction

The Agadez city is built on a fractured sandstone formation, called "Grès d'Agadez" according to the Agadez sandstones nappes map [1], depositing in unconformity on the Aïr Mountains Precambrian basement (Figure 1). Along the western edge of the Aïr Mountains, the sedimentary cover exhibits a succession from Devonian to Lower Cretaceous as revealed by the geological data carried out in the Tim Mersoi basin [2]. According to the previous geological data [1,3-5], all these geological units (basement and basin) are affected by brittle deformations in the

*Corresponding Author:
Baraou Idi Souley,
Department of Geology, University of Agadez, Agadez, Niger;
Email: souleybaraou2@gmail.com

DOI: https://doi.org/10.30564/jees.v4i2.4697

state faults and or fractures with several orientations. Thus the main directions of faults are as follows (Figures 1 and 2):

- At a regional scale, the In-Azaoua-Arlit fault system, N0° trending and the Madaouéla N30° fault system (Figure 1),
- The N130° to N140° trending faults system, affecting the Aïr Mountains, is less frequent in the Tim Mersoï basin,
- The N70°-N80° fault system (farther to the west in the DASA area) has been reactivated in dextral sense during the Upper Cretaceous as indicated by the results of structural study obtained in the Tim Mersoi basin [5,6].
- Another active SSE-NNW system fault was highlighted by the seismic map of African continent [7] on the Eastern edge of Air Mountains and in oriental sedimentary basin of Niger (Figure 2).

On the one hand, these faults and fractures networks would control the setting up of the uranium mineralization in the Tim Mersoï basin as indicated by structural study and mining exploration [5,6,8] and, on the other hand, they present a geotechnical risk in the mining of uranium deposits as suggested by structural study in the Akola uranium ore deposit (Arlit) [9] and on the buildings in the surrounding urban centers.

In the Agadez city, the phenomenon of building fracturation is observed, as well as, on the buildings made from clay materials and those made from cement. The associated risks present in the state of cracks, fractures and faults, often leading to the collapse of buildings resulting in loss of life and property damage. Despite the materials and human damages due to this phenomenon, no significant scientific study has been carried out about the causes and consequences of this geotechnical risk in this town. In addition, the scientific questions in this study involve: what kind of building is more affected by the fracturation? What is the mean direction of the georisk propagation related to this fracturation?

This preliminary study on buildings fracturation aims to assess the geotechnical risks related to the buildings fracturation that occurs in Agadez city. To reach this objective, a methodological approach combining in situ measurements and statistical analyses of obtained data and current state of geological research was implemented.

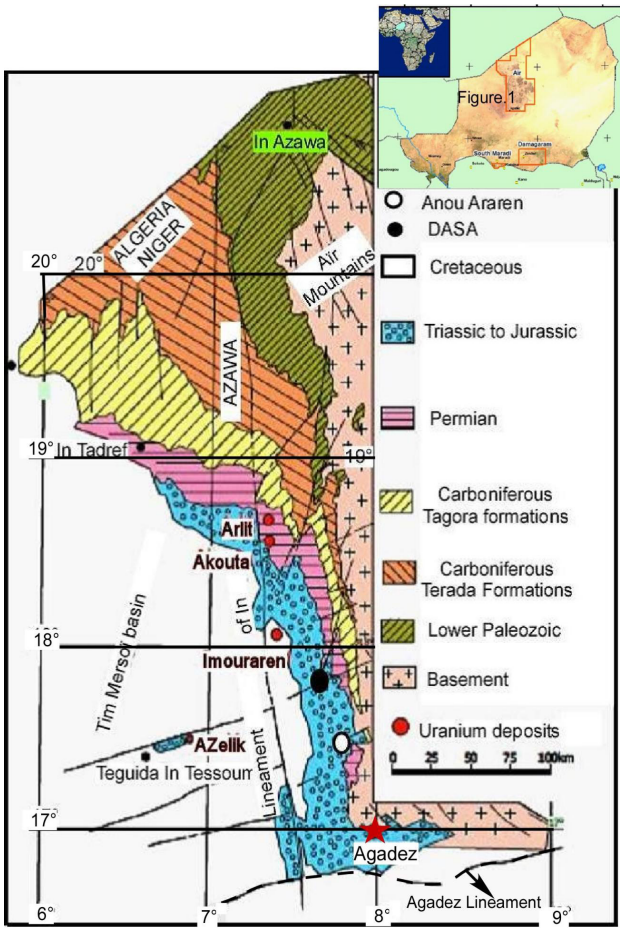

Figure 1. Location of Agadez city on the geological map of the Eastern part of Tim Mersoï Basin, from the previous geological data [1,3-5].

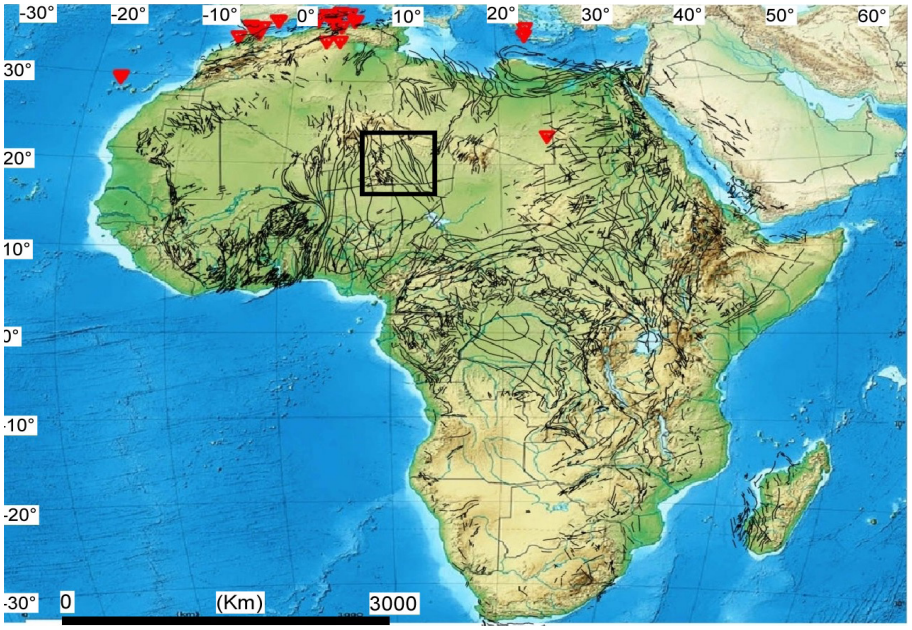

Figure 2. Location of seismic centers (red point) within the tectonic map of Africa seismic, showing the NNW-SSE system fault (black rectangle) on the Eastern edge of Air Mountains and in the oriental sedimentary basin of Niger from OTICE [7].

Note: The original language is French.

2. Materials and Methods

The methodological approach adopted in the case of this study is based on both review literature on the study area, field investigation and processing and statistical analysis of collected data:

1) The review literature focused on bibliographic research of thesis, articles, scientific reports and all other documents relative to the geology of the studied zone,

2) The field investigation consisted of prior identification of the most affected sectors by fracturation and in situ structural measurement of fracture planes. This stage was carried out with material as follows: GPS (for site location), Compass (for direction and dip acquisition of a structure), and acquisition form of structural data, presented in Appendix A1. Data acquisition method was based on the determination of the state structure (crack, fracture fault), its direction and dipping sector and also the type of building affected (from clay material, from cement).

3) Processing and statistical analysis of measured structures was carried out by using the software SPSS.20.0 and MS. Excel 2013, well known for the statistical analysis. Based on risk assessment associated to the building fracturation, this stage consists of:

(1) The classification of collapsing risk according to the opening width of fractures, (2) Risk assessment according to the type of buildings and (3) Risk assessment according to the directions and dip sectors of risk propagation.

3. Results and Discussions

3.1 Identification and Classification of Geotechnical Risks

The obtained data come from the buildings made from cement and those made from clay materials of 10 sites, most affected by the fracturation (Figure 3). The GPS coordinates of different sites are indicated in Appendix A2. The deformation structures identified were classified according to their opening width (Figure 4). The different structures identified are:

- cracks (fine close fractures having a millimetric width Figure 4A) which are considered to be a low-risk structure;
- fractures in the strict sense (the opening of the lips has a millimetric to centimetric width, Figure 4B): these types of structures present a lower risk of building collapse;
- faults planes (these are fractures along which collapse can be observed in buildings, Figure 4C). They present a high geotechnical risk, usually leading to the abandonment or reconstruction of the building.

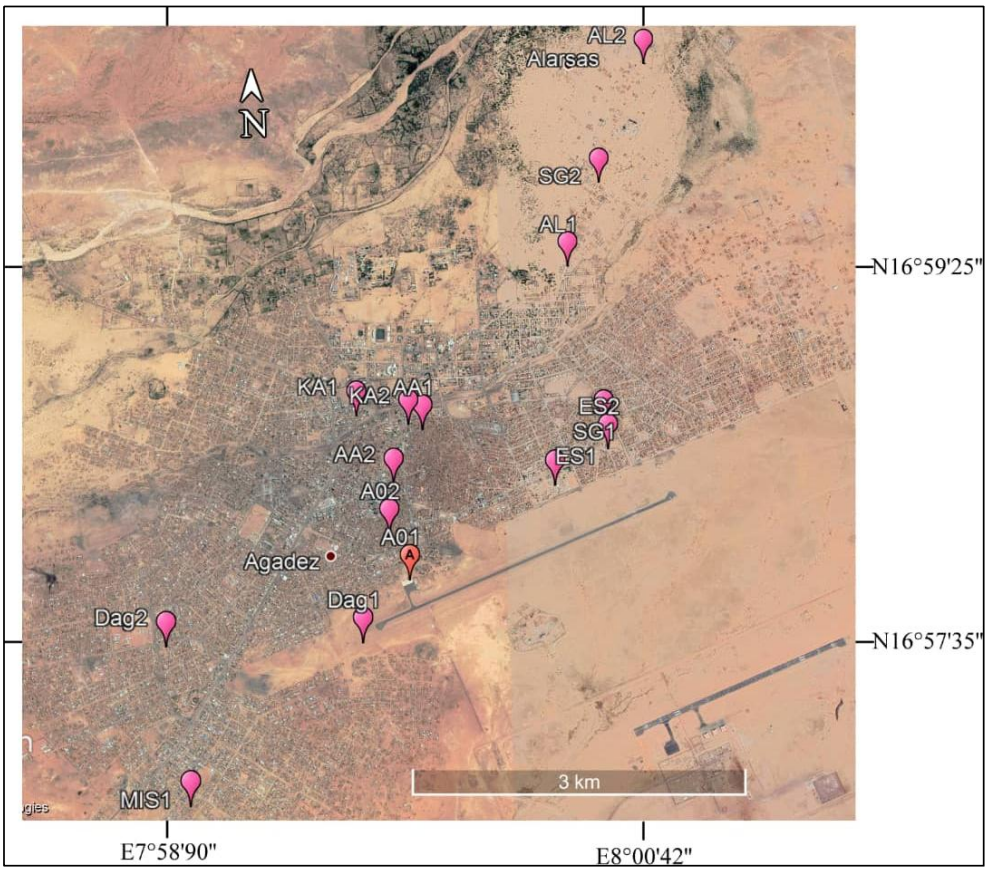

Figure 3. Google Earth location map of the measurement sites for the different fracture planes.

Note: **Sites abbreviations**: **AO**: Airport/Obitara, **ES**: Emair/Sabon Gari, **Mis**: Misrata; **AL**: Tadalanfai/Alaghsass; **KA**: Katanga/Amarewat; **AA**: Amarewat/amdite; **Dag**: Dagmanet; **SG**: Sabon Gari.

3.2 Risks Assessment According to the Type of Buildings

A total of 220 fractures planes affecting the buildings were identified and measured. All of the collected data (structural data and type of buildings studied) are indicated in the Appendix C at the separated excel file. The statistical analysis of measured structures by type of dwelling (Table 1) concerns over 200 structures:

- 74 of measured structures correspond to cracks, i.e. 34%, of which: 40 affected the buildings made from cement and 34 in clay material;
- 140 structures are in the state of fractures , i.e. 64%: 91 affected buildings made from cement and 49 affected the buildings made from clay material;
- 6 structures correspond to the faults, i.e. 3%, of which 2 affected the clay buildings and 4 cement buildings.

Based on percentage of the structural data, out of 100 buildings affected by fractures, about 3% are at risk of faulting, 64% undergo a risk of fracturation, and 34% are affected by simple cracking, which represents a lower risk of collapse.

Data analysis has shown as well that rheology (nature of the material) influences the buildings fracturation. Indeed, the buildings made with cement and reinforced concrete (made from sandstone material) are more easily fractured than buildings made with clay materials. For example, in 220 measured fractures, 135 affect the buildings made from cement, and 85 the buildings made with clay materials (Table 1), or 61.36% against 38.64%.

According to the results obtained by microtectonic study [10], this is due to the difference on rheological behavior between clay which is a plastic and ductile material and sandstone and concrete which are brittle materials.

These observations are in agreement with the results obtained in the Franklinian Basin [11] where, considering the rheology of the materials, the sandstone strata was qualified as a "competent level" for brittle deformation and the clay strata as "incompetent level".

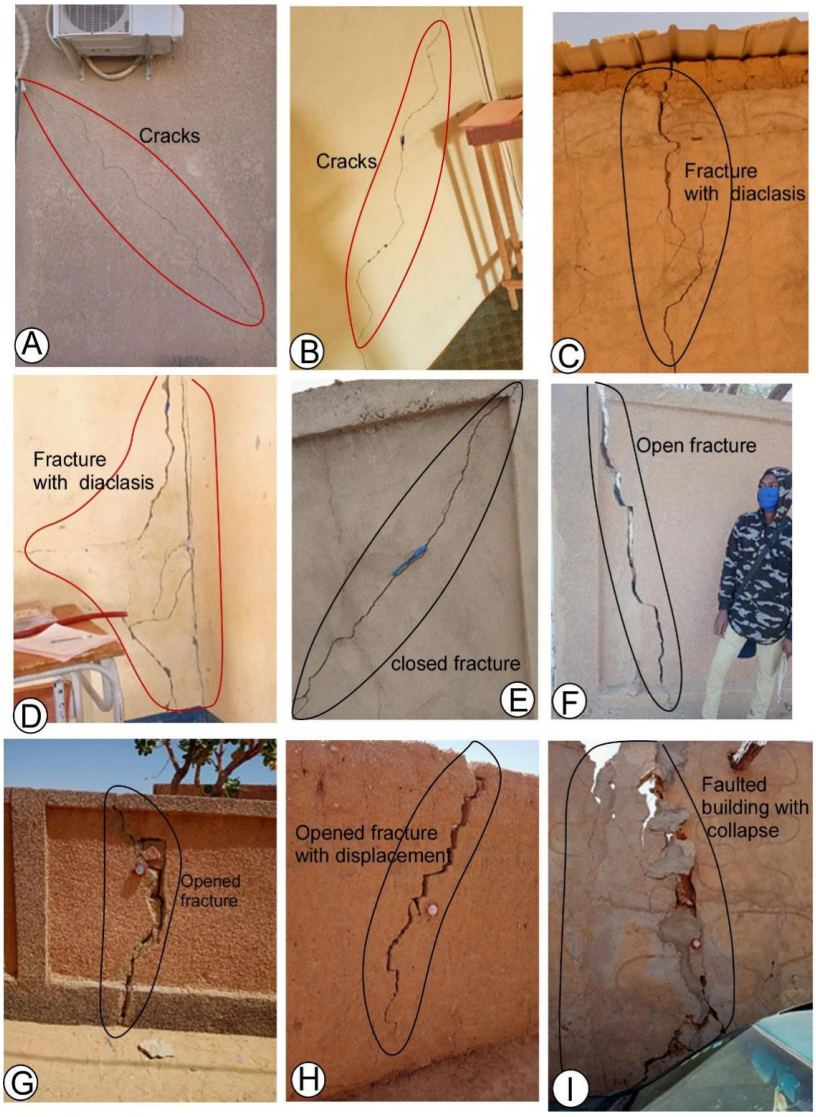

Figure 4. In situ photographs of deformation structures showing the impact of hazards on homes. (A and B) cracked buildings (low risk), (C, D, E, F) fractured buildings (medium risk of collapse), (G, H, I) fractured and faulted buildings (high risk of collapse).

Table 1. Statistic of measured structures in number and by type of material.

State of structures	Number	Percentage (%)	Type of building	
			From cement	from Clay material
Cracks	74	34%	40	34
Fractures	140	64%	91	49
Faults	6	3%	4	2
Total	**220**	**100%**	**135**	**85**

3.3 Risk Assessment According to the Directions and Dip Sectors of Risk

Analysis of geotechnical risks related to fracturation is based on both the determination of direction and dip sectors of fractures planes. Thus, the directions and dip sector of measured fractures (Table 2) were statistically analyzed.

3.3.1 Directional Analysis of Fractures

To determine the major direction of risk propagation, 220 measured planes of fractures are classified by direction interval of 45° from the North (Table 2 and Figure 5). The results of statistical analysis by the percentage of directions are as follows:

- the N0°-N45° directions: 25%,
- N45°-N90° directions: 30%,
- N90°-N135° directions: 12.73%; and

- N135°-N180° directions: 32%.

According to these observations, the directions ranging from SE-NW (N135°) to SSE-NNW (N175°) are the majority with 32%, followed by NE-SW (N45°) to E-W (N90°) directions with 30%. Therefore, the geotechnical risk related to the buildings fracturation has a stronger propagation component according to the mean direction NW-SE (N135°).

Table 2. Directional distribution of measured fractures.

Direction intervals	Effective	Percentage (%)
[N0°-N45°]	55	25.00
[N45°-N90°]	66	30.00
[N90°-N135°]	28	12.73
[N135°-N180°]	71	32.27
Total	220	100.00

3.3.2 Analysis of Fractures According to the Dip Sectors

The risks related to a fracture plane of buildings are not only associated with their propagation directions but also with their dipping sectors. For this, the statistical analysis of 220 fractures planes by their dipping sector was carried out. Thus, among these 220 planes measured:

- 24.55% are dipped toward the Northeast sector,
- 22.27% toward the Southeast,
- 19.09% toward the Southwest, and
- 34.09% toward the Northwest (Table 3 and Figure 6).

This analysis shows that the fracture planes of buildings are dipping mainly (34.09%) in the northwest sectors (zones) of the Agadez city.

Table 3. Statistic of fractures according to their dipping sectors and associated graph.

Dip sectors	Effective	Percentage (%)
North-East	54	24.55
South-East	49	22.27
South-West	42	19.09
North-West	75	34.09
Total	220	100.00

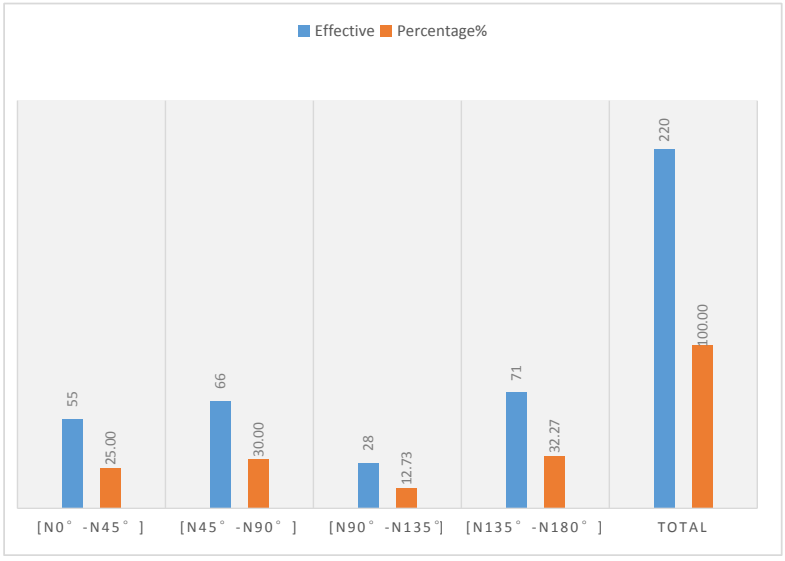

Figure 5. Histogram of 220 measured fractures planes according their directions.

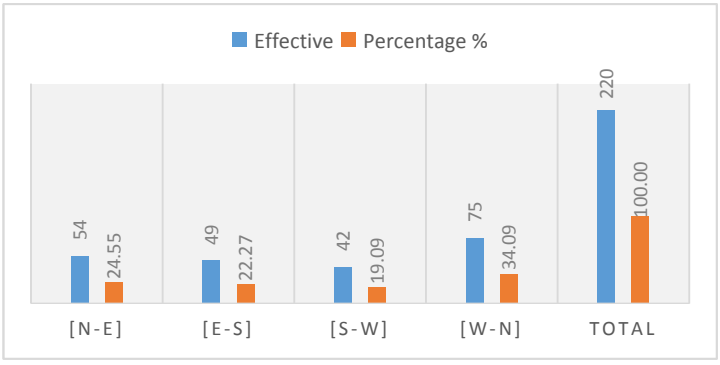

Figure 6. Histogram of 220 measured fracture planes according to the dipping sectors.

Riposte and reducing measures of risks

Despite the damages caused by this geotechnical risk of fracturation, preventive and riposte measures remain still classic. These measures involve the filling of open fractures with cement, which are not yet collapsed (Figures 7A-7B). In some cases, processed fractures continue to widen despite clogging, leading to the definitive abandonment or reconstruction of the building.

This is the case of the buildings of the Regional Direction of Hydraulic (HRD, Agadez, Figure 7C) and some blocks of the Regional Centre of Mother and Child (CRME, Agadez, Figure 7D).

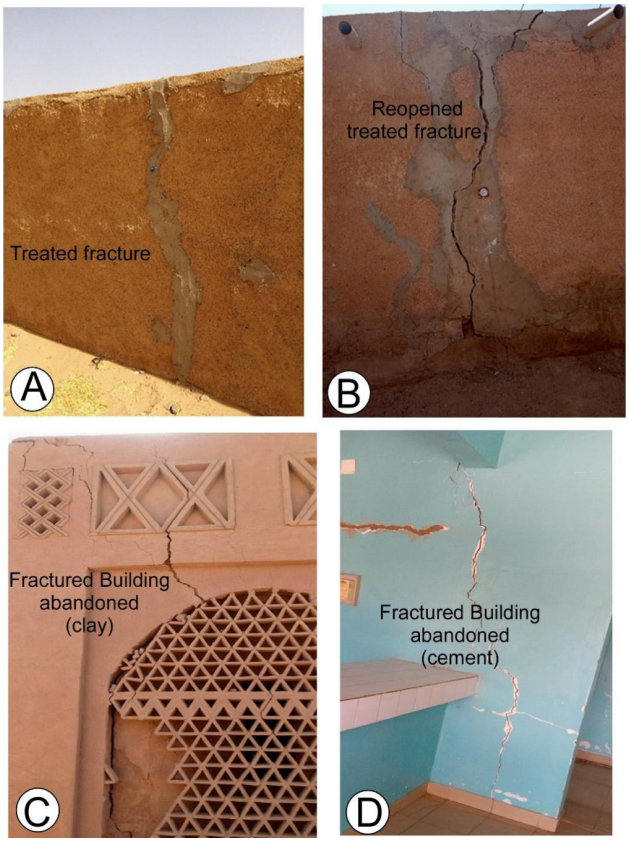

Figure 7. Mitigation and riposte measures against the risk of fracturation of houses in the city of Agadez. (A) Treated fracture, (B) reopened treated fracture (with post-compaction operation), (C) abandoned block in clay material (Dagmanet Town hall, Agadez), (D) abandoned block in final material (Maternity, Agadez).

3.4 Origin of Buildings Fracturation

The phenomenon of buildings fracturation in Agadez city can be interpreted as resulting from the effects of seismic movements occurring within the earth. These seismic movements can be tectonic in origin (natural) or anthropogenic (dynamite blasting at mining sites).

Geological Origin

To better understand and explain the origins of seismic movements causing building fracturation, the investigations focused on: (i) local and regional geological data [4,12-14], (ii) geophysical data (magnetic and seismic) combined with the field observations. The analysis of these data shows that the Agadez city is located on a tectonically active zone corresponding to a major N-S trending lineament belonging to the Arlit In-Azaoua fault system (Figures 1, 2, 8).

According to the geophysics interpretation map [15], the N-S faults affecting the Agadez region (Figure 8) were the focus of three seismic events. The satellite fault of the In Azaoua-Arlit lineament, located to the west of the Agadez city (Figure 8), has been the focus of two seismic events (on May 19, 1967 and on January 18, 2017) according to the African seismic map [7]. In seismology, these three seismic events are considered to be a recurrence phenomenon (in this case every 50 years). Unfortunately, the data did not allow us to know the activity of this fault during the period 1907. If this recurrence is correct, another seismic event should affect this fault in 2067. The Raghane shear system, passing to the eastern part of Agadez city (Figure 8, was the focus of a seismic event on 4th July 1969 from geophysics interpretation map [15]. There is also a potential seismic zone corresponding to a system of strike slip faults oriented ~N75° (Figures 1 and 8), called "Agadez Lineament" [16] or the Guinean-Nubian Lineament (GNL) [17,18] that passed through the southern part of Agadez city [19,20].

A structural study carried out on the Agadez sandstones and the underlying basement (Figure 9), showed that faults and fractures oriented N120° to N165°, affect both the basement of the Aïr Mountains and the sandstone formations on which the city of Agadez is built (Figure 9D**)**. These observations indicate a close relationship between the seismic events affecting the Aïr Mountains and the cracking of buildings in the Agadez city.

These faults and fractures oriented N120° to N165° have been identified on the pseudo-geological map of the southern edge of the Aïr Mountains, produced from the interpretation of Mag/Spectro and Mag/EM airborne geophysical data [15] (Figure 10).

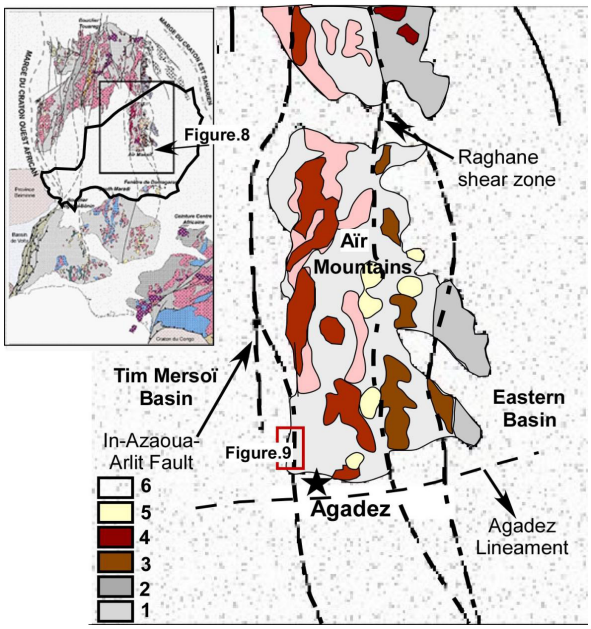

Figure 8. Trans-Saharan regional structures through Aïr Mountains: Raghane shear zone passing to Eastern part of Agadez city and In-Azaoua-Arlit Fault to Western Aïr Mountains [15], modified.

Note: 1. Remobilized Paleoproterozoic Crust, 2. Pan-African Juvenile Crust, 3. Calcaline Granites, 4. Anatectic granites, 5. Younger Granites, 6. Sedimentary Rocks. Original language: French.

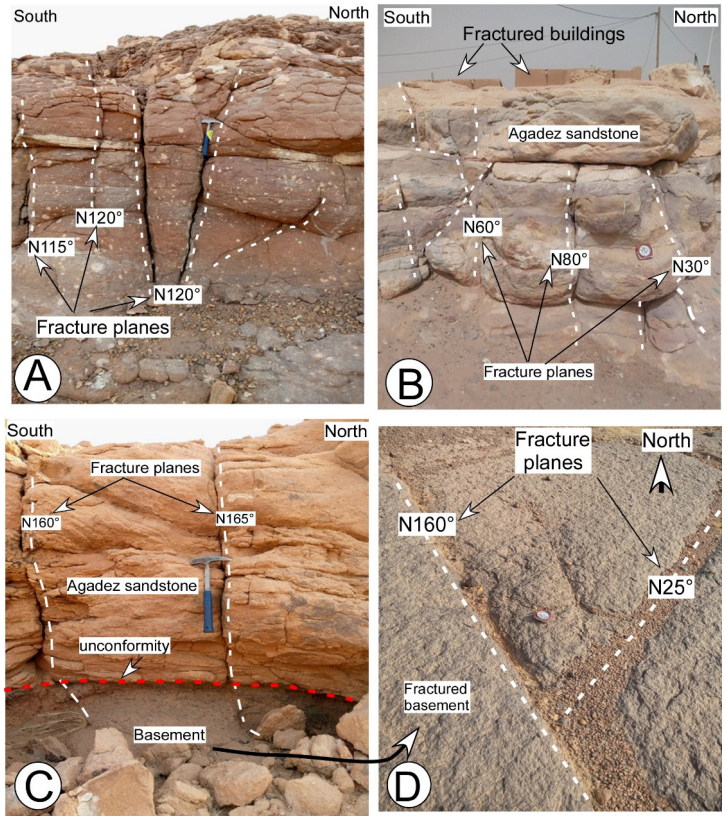

Figure 9. In situ photographies showing the narrow-relations between building fracturation and those affecting the underlying sandstones and basement. (A) Tchibbinnitan fractured sandstones, (B) buildings and their underlying fractured sandstones, (C and D) respectively Agadez sandstones and its underlying basement, all affected by the same directions of fractures.

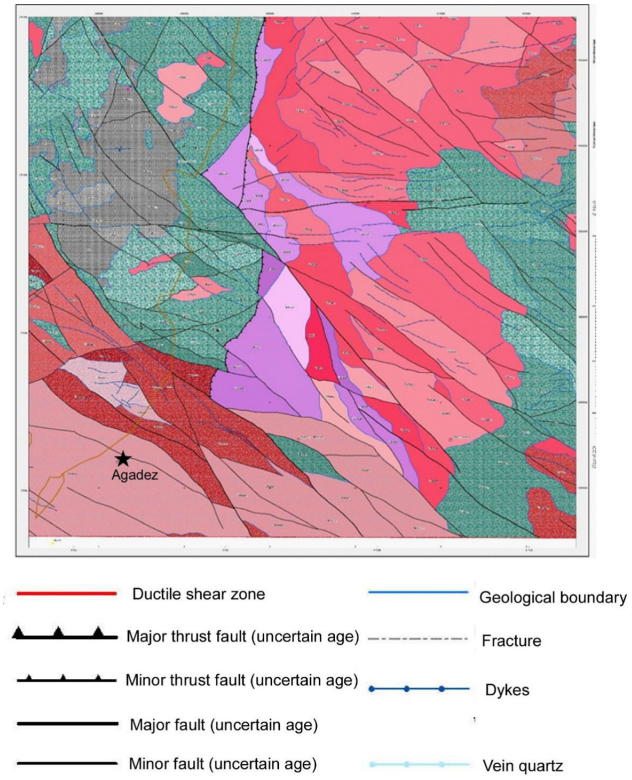

Figure 10. Interpretation of the geophysical map from Mag/Spectro and Mag/EM [15], showing the major directions of fractures affecting the crystalline basement of the Aïr, the Tim Mersoï basin sandstones and the Agadez city buildings.

Note: The original language is French.

Anthropogenic origins

The use of dynamite during the mining of sites such as the Somaïr, Cominak, Sonichar, and Imouraren projects are the anthropogenic activities that create seismic waves that can promote the fracturation of buildings in the city of Agadez. In addition, the vibrations of airplanes during take-off and landing would induce fracturation of the surrounding buildings. Thus, it is imperative to install seismic observation stations using portable seismometers to study fracturation related to seismic waves.

4. Conclusions

According to this study, out of 100 fractured buildings, about three (3) are at major risk of collapse, sixty-four (64) are at risk of fracturation and thirty-four (34) are at risk of cracking. The results also showed that the rheology of the materials strongly influences the fracturation of the building. Indeed, cement buildings fracture more easily than clay buildings.

The kinematic analysis showed that building fracturation has a higher propagation tendency according to the SE-NW direction (N135° on average) in the city of Agadez.

The origin of the fracturation of the buildings was attributed to seismic waves whose origins can be natural (tectonic) or anthropogenic (blasting at mining sites and aircraft vibrations).

4.1 Recommendations

Based on the causes of building fracturation identified by this study, the following recommendations can be made to avoid or reduce the fracturation risks:

- **For tectonic and geological causes**
  - to promote the construction of buildings in clay materials rather than in cement and concrete. Indeed, clay materials with a plastic rheology are less exposed to the fracturation,
  - to consider minor directions of fracture propagation for construction,
  - to study the geological and geotechnical characteristics of the soil before building,
- **For Anthropogenic effects**
  - to avoid the building along or around the fault zones and on basement with predominantly fractured rocks,
  - by acting on the power of the explosives, which should not exceed the energy required to fragment the rocks in the mine,
  - by relocating the airport so that the vibrating waves produced by the aircraft do not impact the social accommodations,
  - to avoid building in the high-vibrating zone (around airports) and or nearby mining sites.
- **For geotechnical measures**
  - the geotechnical standards of civil engineers should take into account the effects of seismic events,
  - for the buildings made from cement, respect the geotechnical construction standards (correct cement dosage and well-reinforced concrete).

4.2 Research Perspectives

In order to accurately determine the causes of the fracturation of buildings in the Agadez city, we aim, together with the mining operators on the one hand and the civil engineers on the other hand:

- to install at least three seismometers at specific locations to identify the seismic focus that is causing the building fracturation,
- to carry out the mechanical tests on the underlying formations (Agadez clay and sandstones) to understand their rheological properties before constructions.

Author Contributions

Baraou Idi Souley: Chief of Investigation, fieldworks, data analysis, cartography and writing manuscript leader,

Abdoulwahid Sani: Permanent assistant during fieldworks, data analysis and cartography operations,

Abdoul Wahab Djibo Maïga: Contributes for geophysical data acquisition (seismic and magnetic maps) and their interpretation,

Moussa Konaté: Research supervisor and permanent assistance during manuscript writing.

Conflict of Interest

No conflict of interest.

Funding

This research received no external funding.

Acknowledgments

We acknowledge the Regional director of Town planning and mayor of Agadez for their technical assistance during the identification works of the sectors more affected by building fracturation. We acknowledge also the Dean of Faculty of Sciences of Agadez University for the financial assistance and BSc students of Department of Geology (Agadez University) for their participation during the fieldworks.

References

[1] Bonnier, 1989. Agadez sandstones nappes. Ministry of Hydrolic-DRE. Project NER/86/001, Niger. (in French)

[2] Clermonté, J., Moussa, Y., Lang, J., et al., 1991. Paleozoic and Mesozoic basin in a strike-slip zone: The Tim Mersoi in the Arlit Region, in the western l'Aïr. Meeting Report of Sciences Academy, Paris 312, II, 1189-1195. (in French)

[3] Tauzin, P., 1981. Geological context of Uranium ore deposit in Eastern edge of Tim Mersoi sedimentary basin, intern report Minatome, Niger. pp. 15. (in French)

[4] COGEMA, 1977. Afasto geological map at 1/200 000 and explanatory notice. Direction of Mines and Geology, Niamey. pp. 31. (in French)

[5] Sani, A., Konaté, M., Karimou, D.H., et al., 2020. Polyphasic tectonic history of the N70° DASA Graben (northern, Niger). Global Journal of Earth and Environmental Science. 5(3), 58-72.

[6] Guiraud, R., Boureïma, O., Robert., J.P., 1981. Evidence of deformation revealing a shorteneing in the Mesozoic of Aïr peripheral (Niger). Meeting Report of Sciences Academy. 292(9), 753-756. (in French)

[7] Wahab, D.M.A., 2017. Location map of seismic focus on the African continent, OTICE Department, HANEA, Niger. (in French)

[8] Mamadou, M., 2016. Metallogenic system of Uranium ore deposit associated to Arlit fault Tim Mersoi basin, Niger [PhD thesis]. Lorraine: Lorraine University. p. 402. (in French)

[9] Wagani, I., Maman, S.B., Alhassane, I., 2019. Structural study of Akola uranium ore deposit and geotechnical risk related to the extracting method in the Cominak, La Revue Ivoirienne des Sciences et Technologie. 34, 230-246. (in French)

[10] Passchier, C.W., Trouw, R.A.J., 2005. Microtectonics (Second edition), Springer-Verlag: Berlin, Germany. pp. 371.

[11] De Paor, D.G., Gloria, E., 1987. Stratigraphic and structural consequences of fault reversal: An example from the Franklinian Basin, Ellesmere Island. Geology. 15(10), 948-949.
DOI: https://doi.org/10.1130/0091-7613(1987)15<948:SASCOF>2.0.CO;2

[12] Ball, E., 1980. An example of very consistent brittle deformation over a wide intracontinental area: The late Pan-African fracture system of the Tuareg and Nigerian shield. Tectonophysics. 16, 363-379.

[13] Liégeois, J.P., Latouche, L., Boughrara, M., et al., 2003. The LATEA metacraton (Central Hoggar, Tuareg shield, Algeria): Behaviour of an old passive margin during the Pan-African orogeny. Journal of African Earth Sciences. 37(3-4), 161-190.

[14] Aissa, D.E., Christian, M., 2017. Controls on gold deposits in Hoggar, Tuareg Shield (Southern Algeria). Journal of African Earth Sciences. 127, 136-145.

[15] PRDSM, 2005. Geophysic interpretation map of Aïr Mountains. Ministry of Mines and Industrial development, Niger. pp. 55. (in French)

[16] Genik, G.J., 2013. Regional framework, structural and petrolium aspect of rift basins in Niger, Chad and the Central African Republic (CRA). Tectonophysics. 213, 169-185.

[17] Guiraud, R., Bosworth, W., 1997. Senonian basin inversion and rejuvenation of rifting in African and Arabia: Synthesis and implications to plate-scale tectonics. Tectonophysics. 282, 39-82.

[18] Wilson, M., Guiraud, R., 1992. Magmatism and rifting in West and Central Africa, from Late Jurassic to recent times. Tectonophysics. 213, 203-225.

[19] Ahmed, Y., Konaté, M., Harouna, M., 2016. Tectono-magmatic reactivation of Téfidet Cretaceous

trough during Cenozoic (Aïr, Niger). Bulletin De La Societe Geologique De France. 187(2), 73-83.

[20] Konate, M., Yacouba, A., Moussa, H., 2019. Structural evolution of the Tefidet trough (East Aïr, Niger) in relation with the West African Cretaceous and Paleogene rifting and compression episodes. Comptes rendus - Geoscience. 351, 355-365. DOI: https://doi.org/10.1016/j.crte.2018.11.009

Appendix A1

Form of structural data **Site name…….**					
Station N°…..	**Latitude……...… Longitude……..……..** **Altitude……**				
Planes N°	**Direction**	**dip**	**Dipping sector**	**State of structure (crack, fracture fault?)**	**Type of building (from clay material, from cement?)**
1					
2					
3					
4					
5					
6					
7					
8					
9					
10					
11					
12					
13					
14					
15					
16					
17					
18					
19					
20					

Appendix A2

Sites	GPS Coordinates (Degree decimal)	
	Longitude	Latitude
Aéroport/Obitar1 (AO1)	7.99010	16.96467
Aéroport/Obitar2 (AO2)	7.98839	16.96846
Emair/Sabon Gari1 (ES1)	8.00276	16.97216
Emair/Sabon Gari2 (ES2)	8.00746	16.97509
Misrata1 (MIS1)	7.971305	16.94694
Misrata1 (MIS2)	7.953611	16.93472
Tadalanf/Alaghsass1 (AL1)	8.00444	16.990555
Tadalanf/Alaghsass2(AL2)	8.011805	17.008055
Katanga/Amarewat1 (KA1)	7.9857	16.97828
Katanga/Amarewat2 (KA2)	7.99021	16.97749
Amarewat Amdite1 (AA1)	7.99142	16.97699
Amarewat Amdite2 (AA2)	7.98885	16.97261
Dagamanet1 (Dag1)	7.96933	16.95983
Dagamanet1 (Dag1)	7.967777	16.96375
Dagamanet2 (Dag2)	7.96561	16.954666
Dagamanet2 (Dag2)	7.96919	16.95966
Sabon Gari1 (SG1)	8.00715	16.97709
Sabon Gari1 (SG1)	8.00408	16.97994
Sabon Gari2 (SG2)	8.00745	16.997705

Appendix/Supplementary materials available

Checklist is presented as stand-alone including simplified supplementary materials in the shape of appendix C. This table is the original creation of the author and all sources are acknowledged and appreciated for its contribution to knowledge and building maintenance. The checklist (table) covers 220 measured fracture planes on the buildings and has too much content (including direction, dips, dip sectors, state of fractures and type of affected building) to display herein. Please contact the journal editorial office if you require.

BILINGUAL PUBLISHING CO.
Pioneer of Global Academics Since 1984

Journal of Environmental & Earth Sciences
https://ojs.bilpublishing.com/index.php/jees

ARTICLE

Stormwater Quality Characteristics and Reuse Analysis of Different Underlying Surfaces at Wanzhou North Station

Shaochun Yuan[1,2] Ting Li[1] Qingwei Yang[1] Shun You[1] Tao He[1] Bo Lv[2,3*]

1. Key Laboratory of Hydraulic and Waterway Engineering of the Ministry of Education, Chongqing Jiaotong University, Chongqing, China
2. Chongqing Engineering Technology Research Center for Sponge City Construction, Chongqing, China
3. Chongqing Academy of Science and Technology, Chongqing, China

ARTICLE INFO

Article history
Received: 14 June 2022
Revised: 26 September 2022
Accepted: 28 September 2022
Published Online: 24 October 2022

Keywords:
Stormwater quality
Underlying surface
Recyclable rainfall
Stormwater utilization

ABSTRACT

In response to the water shortage in Wanzhou North Station (WNS), the authors investigated the stormwater quality characteristics with different underlying surfaces of WNS and carried out stormwater reuse analysis in conjunction with the InfoWorks ICM model. The results show that during heavy, torrential, and moderate rainfall, the road stormwater runoff has the highest concentrations of pollutants, with an average EMC (event mean concentration) value of 206 mg/L for COD. For the square runoff, the average EMC values of COD, SS, TN, and TP are 108 mg/L, 395 mg/L, 2.113 mg/L, and 0.128 mg/L, in comparison, the average EMC values of the corresponding indexes for the roof runoff are 65 mg/L, 212 mg/L, 1.449 mg/L, and 0.086 mg/L, respectively, demonstrating their potential for reuse. The R^2 (coefficient of determination) of SS and COD in both roof and square runoff is greater than 0.85, with a good correlation, indicating that SS removal is the key to stormwater purification. InfoWorks ICM analysis shows that the recyclable volume of rainwater from WNS in 2018 is 29,410 m^3, accounting for 61.8% of the total annual rainfall. This study is expected to provide an ideal reference for the stormwater management of public buildings in mountainous areas.

1. Introduction

Rapid urbanization has destroyed the original hydrological characteristics of the city, not only making the problem of surface pollution more prominent but also wasting a lot of rainwater resources [1-4]. Rainwater resource utilization is an effective way to relieve the pressure on water supply and drainage and improve the water environment, which can bring good environmental benefits and is one of the essential elements of sponge city construction [5-7]. A large number of studies have been carried out in China on stormwater utilization. Ouyang et al. [8] analyzed the rela-

*Corresponding Author:
Bo Lv,
Chongqing Engineering Technology Research Center for Sponge City Construction, Chongqing, 400020, China; Chongqing Academy of Science and Technology, Chongqing, China;
Email: haimiancq@163.com

DOI: https://doi.org/10.30564/jees.v4i2.4795

tionship between stormwater runoff pollutants from different underlying surfaces and the preceding dry period, rainfall amount, and rainfall intensity, and proposed that controlling initial rainwater and sweeping the subsurface can reduce runoff pollution. Yuan et al. [9] found that the correlation between SS and COD, TP, and ammonia nitrogen in rainwater runoff from different underlying surfaces in Xi'an is strong, and SS is a key factor affecting runoff water quality. In addition, there are cases in Beijing and Nanjing where roof and road surface rainwater has been used for greening and watering in public building areas and road washing after filtering treatment [10,11]. In general, current research on rainfall-runoff focuses on pollution control and treatment processes, with less emphasis on stormwater utilization demands and recyclable stormwater volumes.

As a pilot project of the sponge city program in Chongqing, the rainwater utilization rate goal in the Wanzhou District is ≥ 3%. Currently, rainwater resource utilization has become one of the priorities of energy-saving management in large public buildings [12]. Promoting a healthy water cycle and strengthening the construction of ecological sponge watersheds is the demand for water management, while rainwater resource utilization is also an important measure to strengthen the natural water cycle and social water cycle [13,14]. In this study, the rainfall amount and the rainfall duration of WNS are monitored in real-time to study the water quality characteristics of stormwater runoff from different underlying surfaces and the correlation between each pollutant, and the amount of recyclable rainwater is analyzed using the InfoWorks ICM model, to provide a reference for rainwater harvesting and utilization in large public buildings of mountainous cities.

2. Materials and Methods

2.1 Rainfall Monitoring

The rainfall amount in WNS was monitored in real-time by using the telemetry rain gauge. In this paper, three rainfall events (heavy rain, torrential rain, and moderate rain) within the regional catchment were selected for water quality testing, considering that the greater the rainfall, the greater the number of potential rainwater resources, and the rainfall characteristic parameters are shown in Table 1.

2.2 Sample Collection and Analysis

The stormwater water quality of three kinds of underlying surfaces such as roads, squares, and roofs was tested. Sampling points were located at the rainwater inspection well on the left rear side of the station, the square storm sewer, and the road rainwater inlet.

Water sample collection method: sampling every 5 min within the first 30 min after rainfall production flow, every 10 min within 30-60 min, and every 30 min after 60 min. The testing index includes SS, COD, TN, ammonia nitrogen, nitrate nitrogen, TP, etc. The analysis method refers to the "Water and Wastewater Monitoring Analysis Method (Fourth Edition)".

2.3 Data Processing and Analysis

Event mean concentration (EMC): The average concentration of pollutants discharged during the entire course of runoff from a field rainfall event is used because the runoff pollutant concentration is constantly changing during the rainfall process, i.e., EMC to characterize the pollution load of stormwater runoff [15]. Its calculation formula is:

$$EMC = \frac{\sum C_t Q_t \Delta t}{\sum Q_t \Delta t} = \frac{\sum C_t Vt}{\sum Vt}$$

Among them: Δt—the time interval of sampling collection (min); Vt—the amount of runoff rainwater in t period (m^3); Ct—concentration of runoff pollutants in t period (mg/L).

3. Results and Discussion

3.1 Change Law of Rainwater Runoff Water Quality

3.1.1 Road

As can be seen from Figure 1, in the three rainfall events, the concentration of major pollutants in road stormwater runoff rose to a high level at the beginning of the flow production, gradually decreased after 20 min and leveled off after 60 min. The SS concentration ranges from 10 mg/L to 2912 mg/L and EMC average value of 838 mg/L, COD concentration ranges from 7 mg/L to 570 mg/L, and EMC average value of 206 mg/L in the three rainfall events. This is due to the frequent vehicular and

Table 1. Characteristics of rainfall events.

Time	Rainfall amount/ (mm)	Rainfall duration /(min)	Maximum rainfall intensity/ (mm/min)	Average rainfall intensity/ (mm/min)	Preceding dry period/d
2018/07/30	41.5	255	0.8	0.16	17
2018/09/20	63.0	610	1.6	0.10	12
2019/10/07	18.0	225	0.3	0.08	8

pedestrian activities on the road, producing pollutants such as road material abrasives, garbage, and oil; on the other hand, the dry period before rain for both heavy and torrential rainfall events is more than 10 d, with a large accumulation of pollutants, resulting in poor road stormwater runoff water quality with high SS and COD content. Hou et al. [16] found that the water quality of runoff from Beijing ring road trunk roads exceeded the V standard of the Environmental Quality Standards for Surface Water (GB3838-2002), and the pollutants mainly came from the abrasion of wheels and road materials as well as atmospheric deposition and vehicle exhaust, which was consistent with this study.

TN ranges from 0.690 mg/L to 6.877 mg/L and EMC average value of 3.271 mg/L in the three rainfall events, which exceeds the surface water V standard, while ammonia nitrogen and nitrate nitrogen range from 0.050 mg/L to 1.192 mg/L and 0.230 mg/L to 2.683 mg/L, respectively, which means that organic nitrogen has a high proportion in TN, indicating a certain degree of organic pollution of rainwater. The peak pollutant concentrations of heavy rain, torrential rain, and moderate rain occurred at 15 min, 10 min, and 15 min, respectively, and the concentrations of COD, SS, and TN in the runoff at the beginning of the storm were significantly higher than those of heavy rain and moderate rain, which indicated that the runoff flushed the subsurface more strongly during the storm [17,18], making the peak pollution concentration forward. This shows that the road stormwater runoff is subjected to a higher level of pollution and is not suitable for recycling.

3.1.2 Square

From Figure 2, it can be seen that during the heavy rainfall and torrential rainfall events, the COD of the rainfall-runoff from the square reached the peak of 255 and 355 mg/L at 15 min and 10 min after the flow production, respectively, and the SS also reached the highest values of 801 and 1578 mg/L at this time; in the medium rain event, the COD reached the peak of 34 mg/L at 10 min after the flow production, and the SS reached the peak of 123 mg/L at 20 min after the flow production, it indicates that the organic matter mostly exists in the suspended state, which may be influenced by the construction dust on the right side of the square. There was a rise and then a decrease in TN and TP, which eventually leveled off, with the average EMC value of 2.113 mg/L and 0.128 mg/L respectively, and TN exceeded the surface water category V standard. The pollution level of the square rainfall runoff was significantly reduced after 20 min, the water samples were observed to be clearer when sampling and their EMC mean values of TN, ammonia nitrogen, nitrate nitrogen, TP, COD, and SS were reduced to 1.272, 0.188, 0.754, 0.098, 76, and 215 mg/L, while only COD exceeded the surface water category V standard. The main pollutants of the square rainwater runoff are COD and SS, and the quality of the collected rainwater can be greatly improved by the initial rainwater abandonment and ground sweeping.

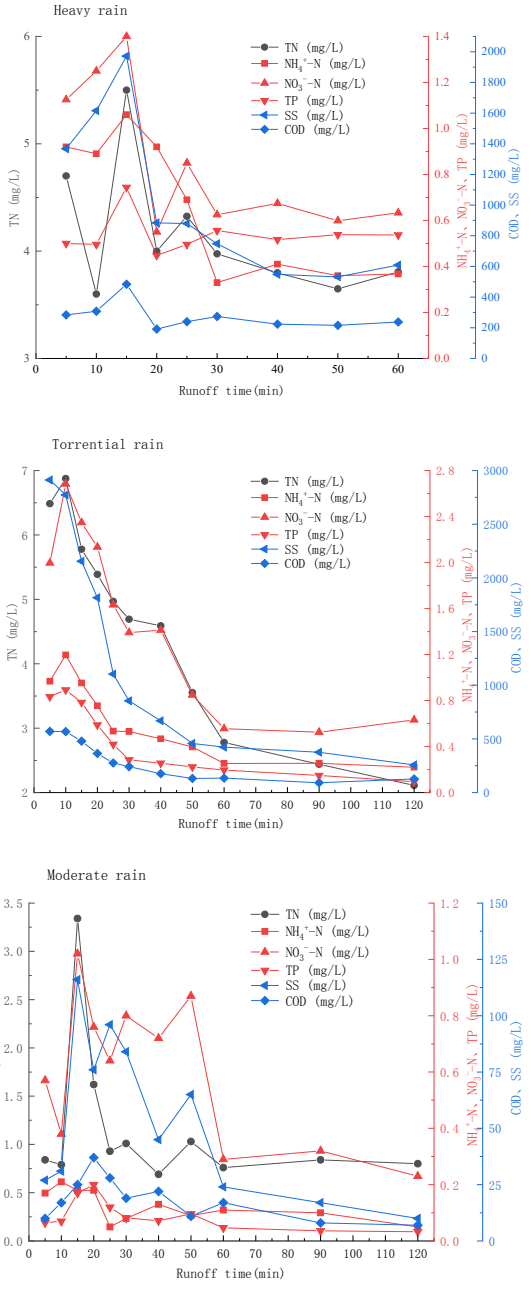

Figure 1. Variation curve of road stormwater runoff water quality.

It is not difficult to see that the water quality of the rainwater runoff in the moderate rain was significantly better than in the previous two rainfalls, which shows that with the gradual improvement of the construction of the WNS Sponge City, the runoff pollution in the Tianzi Lake

watershed has been alleviated. Considering the correlation between SS and COD, the concentration of pollutants can be further reduced by precipitation or clarification [18], so that the square rainwater has good reuse potential.

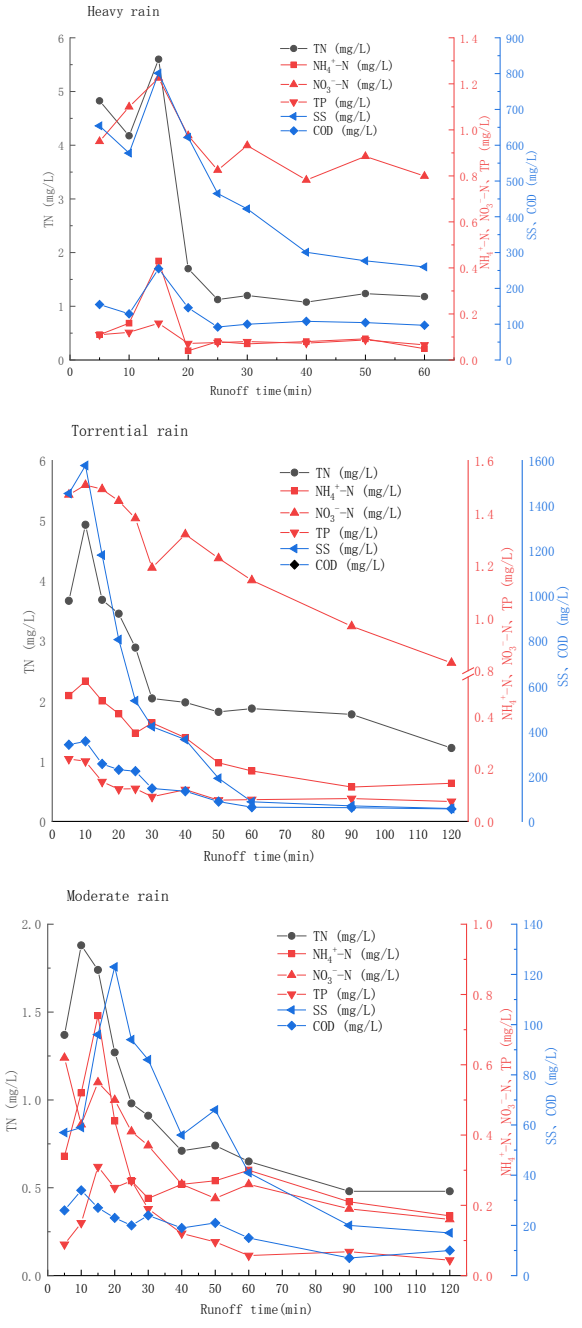

Figure 2. Variation curve of square stormwater runoff water quality.

3.1.3 Roof

In general, roof pollutants mainly come from atmospheric deposition and roofing materials [19,20], and the roof of the station house in this study is made of metal, which has minimal effect on runoff water quality. The mean EMC values of TN, ammonia nitrogen, nitrate nitrogen, TP, COD, and SS in roof rainwater runoff were 1.449, 0.201, 0.626, 0.086, 65, and 212 mg/L, respectively, which were significantly better than the road and square runoff water quality, and the main pollution indicators were still COD and SS.

From Figure 3, it can be seen that the TN and nitrate nitrogen concentrations fluctuated greatly in the three rainfall events, with the peak TN in heavy rain and heavy rain appearing at the beginning of the flow production, and the peak TN in medium rain appearing at 20 min of flow production. The peaks of TN, ammonia nitrogen, and nitrate nitrogen caused by heavy rain were higher than those of torrential rain and medium rain, while the peaks of SS, COD, and TP were lower than those of torrential rain but higher than those of medium rain, which may be due to the longer number of sunny days in the early part of heavy rain and the higher accumulation of NOx in the air. Yuan et al. [9] calculated the contribution of atmospheric drenching and subsurface scouring to pollutants and found that atmospheric drenching was the main source of rainwater ammonia nitrogen, and subsurface scouring was the main source of TP, SS, and COD, which indicated that the higher COD and SS were caused by stormwater flushing. With the gradual improvement of the supporting projects of WNS, the construction dust will gradually disappear. Comparing the runoff water quality of three rainfall events, it can be seen that the roof runoff water quality is gradually becoming better, and it can be predicted that soon the roof runoff water quality will be significantly better than the current stage, with good potential for recycling.

3.2 Analysis of Initial Scour Effect

The subsequent discussion focuses on stormwater from the square and the roof, as the reuse value of road stormwater was found to be low in combination with the process change characteristics of runoff water quality. In this paper, we evaluate the scour effect according to Geiger [21], and if the difference between the slope of the M(V) curve and the diagonal slope is greater than 0.2, the initial scour is considered to have occurred. During heavy and torrential rainfall events, the cumulative pollution load curves of TP, TN, ammonia nitrogen, and SS in the rainfall-runoff from the square and the roof are above the diagonal line, as shown in Figure 4 and Figure 5, indicating that a certain degree of initial scouring occurred, but the scouring effect of nitrate nitrogen was not obvious. The first flushing of TN in torrential rainfall events was more significant than that in heavy rainfall events, mainly because the dry

period before the rain was longer and the nitrogen content was higher due to atmospheric washing and surface scouring effects. The concentrations of ammonia and nitrate nitrogen in the rainfall runoff from the square were low, but the initial TN flushing effect was obvious, and it can be presumed that the initial flushing object was mainly organic nitrogen.

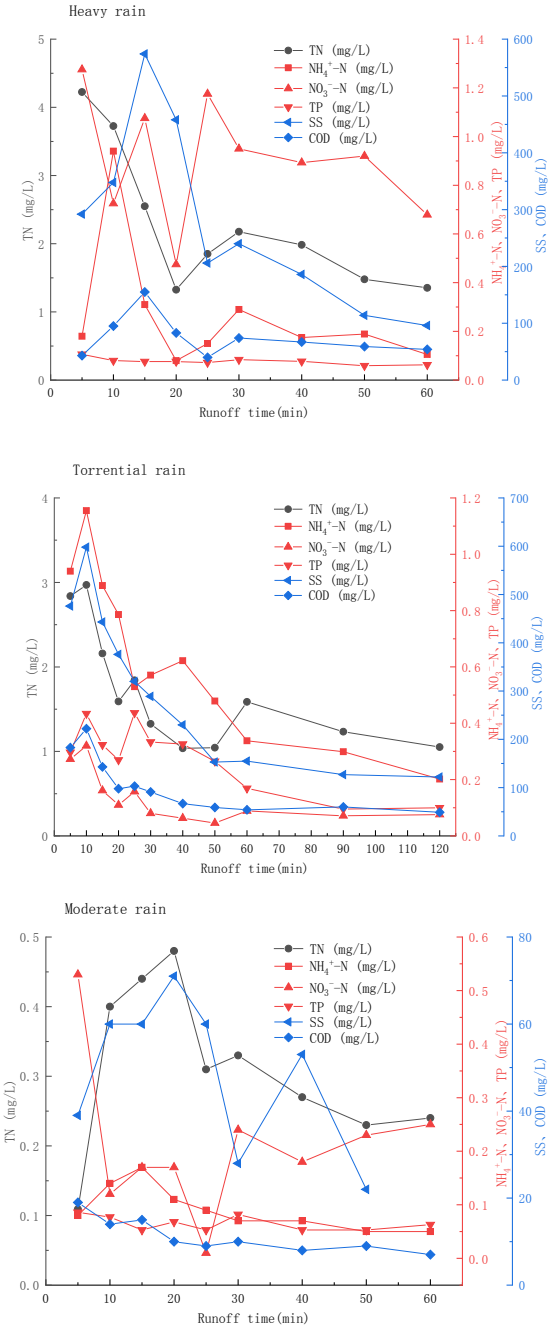

Figure 3. Variation curve of roof stormwater runoff water quality.

The first flushing of rainwater on the roof was not obvious, probably because, in the rainfall process, the slope of the roof is conducive to the collection of rainwater, but the metal roof is not easy to attach particles. The square, however, has a larger catchment area, is more significantly affected by human activities, has a larger accumulation of pollutants [22,23], and is prone to first flushing. The runoff water quality is influenced by the frequency of ground sweeping, human activities, rainfall amount, rainfall intensity, and the dry period before rain [24], which makes the rainfall-runoff scour curves of different underlying surfaces both similar and complex.

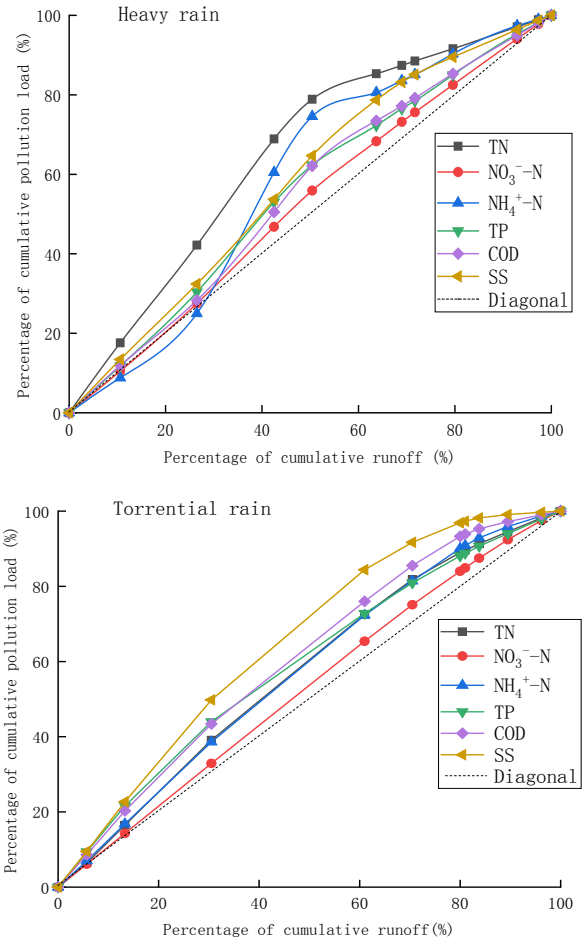

Figure 4. Cumulative distribution curves of square runoff pollution load.

3.3 Analysis of Runoff Pollutants

Identifying the source of pollutants is essential for runoff pollution reduction and stormwater resource utilization, so the source of pollutants was analyzed in conjunction with the coefficient of determination R^2 (see Table 2) between the indicators [25]. There was a good correlation between COD, ammonia nitrogen, nitrate nitrogen, TN, TP, and SS of the square runoff at the significance 0.01 level, and the R^2 values were all greater than 0.6, which can be presumed that COD and ammonia nitrogen of the

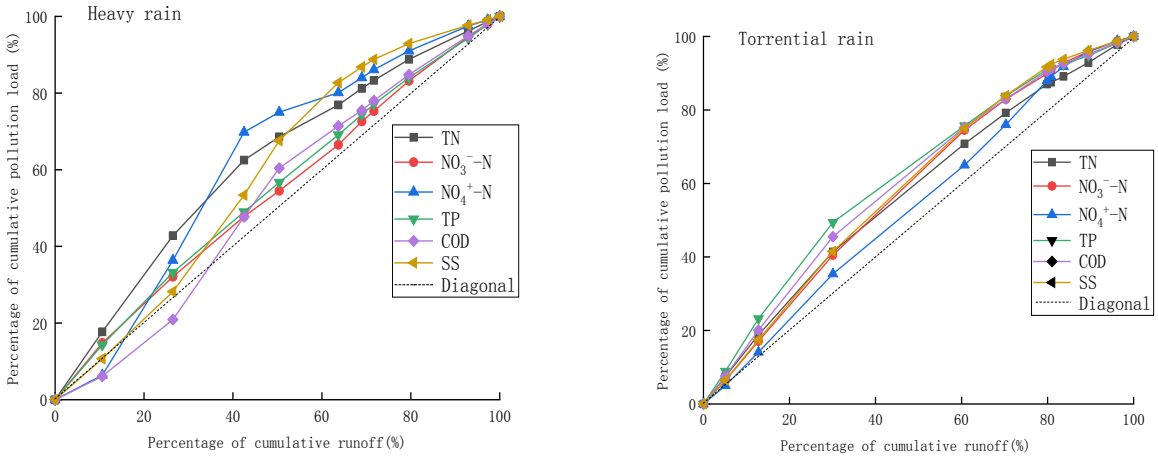

Figure 5. Cumulative distribution curves of roof runoff pollution load.

square were endowed in the particulate state and accumulated on the ground [23]; the R^2 values of SS and COD, ammonia nitrogen, nitrate nitrogen, TN, and TP were 0.95, 0.75, 0.70, 0.71, and 0.89, indicating that the effective removal of SS can effectively improve stormwater quality.

COD of roof runoff was well correlated with TP and SS, TP with SS at the significance 0.01 level, and their R^2 values were 0.87, 0.86, and 0.67, respectively, indicating that SS is homologous with COD and TP, which is consistent with the results obtained by Zhao et al. [22] studying the characteristics of pollutant changes in rainfall-runoff; while ammonia nitrogen was correlated with SS and TP, nitrate nitrogen with SS and COD. TN and TP have no significant correlation, and TN and SS have a weak correlation at the significance 0.05 level, which is significantly different from the correlation between the pollutant indicators of square runoff, probably because in the process of runoff generation and pooling, nitrogen is mainly dissolved in the rainwater in the dissolved state, and the amount attached to suspended matter is less.

3.4 Prediction of Recoverable Rainwater Amount

InfoWorks ICM was used to simulate the rainfall and its runoff process in WNS. The fixed PR Model was used for the flow production model of the roof and square, and the fixed runoff coefficient was taken as 0.9. Horton Infiltration Model was used for the flow production model of the green area. The SWMM model was used for the confluence model of each sub-bedding surface, and the system of St. Venant equations was used for the pipe cal-

Table 2. Linear correlation coefficients between the pollution of different underlying surfaces of rainfall runoff.

Underlying surface	Contaminant	Determination coefficients R^2					
		COD	NH_4^+-N	TN	TP	SS	NO_3^--N
Square	COD	1					
	NH_4^+-N	0.85**	1				
	TN	0.75**	0.67**	1			
	TP	0.96**	0.88**	0.76**	1		
	SS	0.95**	0.75**	0.71**	0.89**	1	
	NO_3^--N	0.79**	0.92**	0.62**	0.77**	0.70**	1
Roof	COD	1					
	NH_4^+-N	0.38	1				
	TN	0.38	0.52*	1			
	TP	0.87**	0.23	0.43	1		
	SS	0.86**	0.38	0.51*	0.67**	1	
	NO_3^--N	0.17	0.20	0.53*	0.41**	0.81	1

Note: *at the 0.05 level (two-tailed), ** at the 0.01 level (two-tailed), the correlation is significant; the coefficient of determination R^2 = the square of the correlation coefficient R.

culation.

The measured data of the September 20 rainstorm event were organized into the module format specified by ICM, with the rainfall calendar time set to 4 h and the initial rainfall volume abandoned at 5 mm, and the simulation yielded a late cumulative runoff volume of 2142 m^3. This means that the recoverable rainfall volume for this rainfall event is 2142 m^3, which is 73.4% of the total rainfall volume. The analysis showed that the accumulated rainfall days of WNS in 2018 were 125 d and the total rainfall amount was 1028 mm, and continuous rainfall simulation was performed by inputting the measured 5 min rainfall data of that year, which resulted in the recoverable rainfall amount of 29410 m^3, accounting for 61.8% of the total rainfall amount of that year. It can be seen that WNS can recycle a large amount of rainwater, because the main pollution index of the roof and square rainwater runoff for SS and COD, can be combined with the site topography conditions set rain gardens, bio-retention facilities, permeable paving, storage ponds and other green facilities to detain and purify stormwater, to achieve the dual effect of runoff pollution reduction and stormwater recycling.

3.5 Benefits Analysis

Stormwater reuse is conducive to relieving water supply pressure, reducing pollution of receiving water bodies, and improving the ecological environment. According to the idea of local consumption, rainwater can be considered for watering the square, roads, and green areas of WNS [26]. The water demand is measured according to the area of the square, green space, and road, combined with relevant standards, see Table 3 for details. InfoWorks ICM analysis shows that the recoverable water is 29,410 m^3/a, accounting for 40.4% of the miscellaneous water demand of WNS. If the water price is 4 yuan/m^3, the annual water cost can be saved by 117,600 yuan.

Table 3. Forecast of miscellaneous water demand of WNS.

Use	Water quota L/(m^2·d)	Service area/(m^2)	Annual water consumption/(m^3)
Square	2.5	31300	28560
Afforestation	2.0	3724	2718
Road	2.5	45435	41458
footing	6.5	80459	72736

Rainwater utilization is one of the important tasks of urban stormwater management [27], which can promote the effect of total annual runoff control, enhance social awareness of water conservation, make people feel the environmental enhancement brought by sponge city construction, and is of great significance to enhance the well-being of the public, with significant social benefits.

4. Conclusions

(1) The average EMC values of SS, COD, TN, and TP in road stormwater runoff are 1,228, 293, 4.425, and 0.496 mg/L, respectively. While the road runoff is not suitable for harvesting and reuse, the water quality of square and roof runoff is considerably better, with contaminants mainly in the form of SS and COD (i.e., 581 and 159 mg/L for square runoff, 293 and 92 mg/L for roof runoff). The TN and TP of rainwater runoff in the latter period are close to the regulatory standards for water reuse, which means less treatment is required and therefore a lower overall cost for rainwater utilization.

(2) The TN and TP of the square and roof runoff have different degrees of initial scouring, and the determination coefficients R^2 of SS and COD are all greater than 0.85, which shows a strong correlation, indicating that the reduction of suspended solids is critical for rainwater reuse.

(3) Using InfoWorks ICM simulation, it is concluded that the annual recyclable rainfall of WNS is 29,410 m^3, accounting for 40.4% of its miscellaneous water demand. Rainwater harvesting and reuse can alleviate flooding in urban areas and reduce water consumption. As one of the emerging practices for water conservation, it is expected to play an important role in sustainable urban planning and construction.

Conflict of Interest

There is no conflict of interest.

Funding

The authors are grateful for the financial support provided by the National Natural Science Foundation of Chongqing (cstc2020jcyj-msxmX1000).

References

[1] Hou, J.W., Mao, H.X., Li, J.P., et al., 2019. Spatial simulation of the ecological processes of stormwater for sponge cities. Journal of Environmental Management. 232, 574-583.
DOI: https://doi.org/10.1016/j.jenvman.2018.11.111

[2] Zhu, Zh.H., Chen, X.H., 2017. Evaluating the effects of low impact development practices on urban flooding under different rainfall intensities. Water (Basel). 7(9), 548.
DOI: https://doi.org/10.3390/w9070548

[3] Jiang, Y., Zevenbergen, Ch., Ma, Y.Ch., 2018. Urban pluvial flooding and stormwater management: A con-

temporary review of China's challenges and "sponge cities" strategy. Environmental Science & Policy. 80, 132-143.
DOI: https://doi.org/10.1016/j.envsci.2017.11.016

[4] Sulej-Suchomska, A.M., Przybyłowski, P., Polkowska, Ż., 2021. Potential toxic effects of airport runoff water samples on the environment. Sustainability (Basel, Switzerland). 13(13), 7490.
DOI: https://doi.org/10.3390/su13137490

[5] Li, Q., Wang, F., Yu, Y., et al., 2019. Comprehensive performance evaluation of LID practices for the sponge city construction: A case study in Guangxi, China. Journal of Environmental Management. 231, 10-20.
DOI: https://doi.org/10.1016/j.jenvman.2018.10.024

[6] Song, J., Han, M., Kim, T., et al., 2009. Rainwater harvesting as a sustainable water supply option in Banda Aceh. Desalination. 1(248), 233-240.
DOI: https://doi.org/10.1016/j.desal.2008.05.060

[7] Zhang, X.Q., Hu, M.Ch., 2014. Effectiveness of rainwater harvesting in runoff volume reduction in a planned industrial park, China. Water Resources Management. 3(28), 671-682.
DOI: https://doi.org/10.1007/s11269-013-0507-9

[8] Ouyang, W., Wang, W., Hao, F.H., et al., 2010. Pollution characterization of urban stormwater runoff on different underlying surfaces conditions in Beijing. China Environmental Science. 9(30), 1249-1256.

[9] Chen, H.Q., Lin, Y., Yuan, H.L., 2011. Analysis of quality variation of rainwater in Xi'an. Journal of Xi'an University of Architecture & Technology. 3(43), 391-395.
DOI: https://doi.org/10.3969/j.issn.1006-7930.2011.03.015

[10] Cheng, Y.N., Wang, R.J., 2018. A novel stormwater management system for urban roads in China based on local conditions. Sustainable Cities and Society. 39, 163-171.
DOI: https://doi.org/10.1016/j.scs.2017.09.001

[11] Xu, H.Zh., 2020. Environmental optimization design of rainwater utilization system in large sports venues under the influence of ocean climate. Journal of Coastal Research. sp1(104), 887-890.
DOI: https://doi.org/10.2112/JCR-SI104-152.1

[12] Peng, J., Zhang, X.M., Zhang, Y.H., 2018. Study on combining flood control with rainwater utilization of airports in China. IOP conference series. Earth and Environmental Science. 1(191), 12133.
DOI: https://doi.org/10.1088/1755-1315/191/1/012133

[13] Liu, H., Jia, Y.W., Niu, C.W., 2017. "Sponge city" concept helps solve China's urban water problems. Environmental Earth Sciences. 14(76), 1-5.
DOI: https://doi.org/10.1007/s12665-017-6652-3

[14] Xu, Y.Sh., Shen, Sh.L., Lai, Y., et al., 2018. Design of sponge city: Lessons learnt from an ancient drainage system in Ganzhou, China. Journal of Hydrology (Amsterdam). 563, 900-908.
DOI: https://doi.org/10.1016/j.jhydrol.2018.06.075

[15] Lee, J.Y., Kim, H., Kim, Y., et al., 2011. Characteristics of the event mean concentration (EMC) from rainfall runoff on an urban highway. Environmental Pollution. 4(159), 884-888.
DOI: https://doi.org/10.1016/j.envpol.2010.12.022

[16] Hou, P.Q., Ren, Y.F., Wang, X.K., et al., 2012. Research on evaluation of water quality of Beijing urban stormwater runoff. Environmental Science. 1(33), 71-75.

[17] Ma, Y.W., Wan, J.Q., Ma, Y., 2011. Characterization of rainfall runoff pollution transportation in different underlying surface of Dongguan City. China Environmental Science. 12(31), 1983-1990.

[18] Tang, W.F., Hu, Y.B., He, X.W., et al., 2017. Research on pollution characteristics of rainwater runoff water quality based on the traditional development mode in urban area of Huainan. Environmental Engineering. 2(35), 53-58.
DOI: https://doi.org/10.13205/j.hjgc.201702012

[19] Lee, J.Y., Bak, G., Han, M., 2012. Quality of roof-harvested rainwater—Comparison of different roofing materials. Environmental Pollution. 162, 422-429.
DOI: https://doi.org/10.1016/j.envpol.2011.12.005

[20] Mao, J., Xia, B.Y., Zhou, Y., et al., 2021. Effect of roof materials and weather patterns on the quality of harvested rainwater in Shanghai, China. Journal of Cleaner Production. 279, 123419.
DOI: https://doi.org/10.1016/j.jclepro.2020.123419

[21] Wang, H.Y., Liu, M., Liu, Q.M., et al., 2006. First flush effect of urban stormwater runoff and management of runoff pollutant. Advances in Water Science. 2(17), 181-185.
DOI: https://doi.org/10.3321/j.issn:1001-6791.2006.02.006

[22] Zhao, X.J., Wang, Sh.P., Yu, H., et al., 2019. Analysis on characteristics of rainfall runoff pollutants flush of typical underlying surfaces in Tianjin central city. Environmental Engineering. 7(37), 34-87.
DOI: https://doi.org/10.13205/j.hjgc.201907007

[23] Xu, Y.J., Gong, Y.M., Bi, J.P., et al., 2020. Analysis of rainwater runoff pollution characteristics of various typical underlying surfaces in Ningbo. Environmental Science. 07(41), 3275-3284.

[24] Huang, J.L., Tu, Zh.H., Du, P.F., et al., 2009. Comparative study on characteristics of urban rainfall

runoff from two urban lawn catchments in Macau and Xiamen. Environmental Science. 12(30), 3514-3521.

[25] Wu, M.Sh., Li, S.M., Zhang, W.Q., et al., 2020. Pollution characteristics and control strategies of runoff in Tianjin Binhai Lingang industrial park. Chinese Journal of Environmental Engineering. 12(14), 3435-3446.

[26] Ma, X., Xue, X., González-Mejía, A., et al., 2015. Sustainable water systems for the city of tomorrow—A conceptual framework. Sustainability. 7(9), 12071-12105.
DOI: https://doi.org/10.3390/su70912071

[27] Huang, J.H., Duan, T.T., 2017. Comparative study on sponge city development in China and integrated stormwater management in Canada: A case study of Toronto. Water Resources Protection. 5(33), 5-12.
DOI: https://doi.org/10.3880/j.issn.1004-6933.2017.05.002

BILINGUAL PUBLISHING CO.
Pioneer of Global Academics Since 1984

Journal of Environmental & Earth Sciences
https://ojs.bilpublishing.com/index.php/jees

ARTICLE

Projected Rainfall Intensity Duration Frequency Relationships under Climate Change: A Case Study of Thane City

S. S. Pujari* **A. S. Wayal**

Veermata Jijabai Technological Institute, Civil and Environmental Engineering Department, Mumbai, Maharashtra, India

ARTICLE INFO

Article history
Received: 21 August 2022
Revised: 23 September 2022
Accepted: 30 September 2022
Published Online: 19 October 2022

Keywords:
Climate change
Rainfall analysis
Projected IDF relationships
IDF curves
Thane city

ABSTRACT

Climate change is the most important factor to increase in short-duration high-intensity rainfall and consequent flooding. Intensity-Duration-Frequency (IDF) curves are commonly used tools in Stormwater design, so a method to derive future IDF curves including climate change effects could be necessary for mainstreaming climate change information into storm water planning. The objective of the present study is to define a mechanism to reflect the effect of climate change on the projected rainfall IDF relationships. For this, the continuously observed hourly rainfall data from 1969 to 2018 were divided into five subgroups. Then the IDF curve of each subgroup is defined. The rainfall intensity for the next 30 years was then estimated using a linear regression model. The obtained result indicates that for the same duration and for the same return period, the rainfall intensity is likely to increase over time: 17% (2019-2028), 25% (2029-2038) and 32% (2039-2048). However, the findings presented in this paper will be useful for local authorities and decision makers in terms of improving stormwater design and future flood damage will be avoided.

1. Introduction

An increase in the occurrences of heavy rainfall events and high tide indicates the risk of flooding in many coastal cities. The annual economical expenditure on flooding is much higher than the other annual disasters [1]. Flooding in urban areas now become a major concern and poses a challenge to the urban planner [2]. The rainfall Intensity-Duration-Frequency (IDF) relationships are essential for stormwater design and planning [3]. Accurate and recent rainfall analysis is an important device for water-related system design [4]. The first step of hydraulic design in the stormwater drainage system is to construct IDF curve [5]. The rainfall IDF relationship gives information about location rainfall characteristics. The rainfall IDF relationships provide logic to find out the intensity of rainfall for a particular duration and return period [6]. The three essential

*Corresponding Author:
S. S. Pujari,
Veermata Jijabai Technological Institute, Civil and Environmental Engineering Department, Mumbai, Maharashtra, India;
Email: sspujari_p18@ci.vjti.ac.in

DOI: https://doi.org/10.30564/jees.v4i2.4995

rainfall depths, that is, R_1^{10} (1 h, 10-year rainfall depth), R_{24}^{10} (24 h, 10-year rainfall depth), and R_1^{100} (1 h, 100-year rainfall depth) used to derive IDF formula for any United States location [7,8]. Ram Babu has studied rainfall data of 42 rain gauge stations all over India and developed IDF equations and nomographs [9]. Kothyari and Garde have studied rainfall data of 78 rain gauge stations all over India and developed IDF equation using rainfall depth R_{24}^2 (24 h, 2-year rainfall depth) [10]. The IDF curves for Abha region in Saudi Arabia were established using Gumbel, Log normal and Log Pearson Type III distribution frequency analysis techniques for different return periods [11].

Thane city situated near to creek and heavy rainfall coincides with high tide then the risk flooding increases. Therefore, to avoid flood risk proper knowledge of IDF curves is required. Zope has studied 40 years of rainfall data from Santacruz rain gauge station and developed IDF relationships by using Gumbel's method [12]. Further it is felt that, IDF curves need to be updated as per the change of climate effect for a given area [13].

The present paper aims to perform statistical analysis of rainfall data to define projected IDF relationships by using the linear regression model, which reflects the changing trend in rainfall intensity.

2. Study Area

Thane is a metropolitan city in Maharashtra, India. It is placed on the North-East of Salsette Island and shares a boundary connecting to Mumbai city (Figure 1). The city placed at 19° 10' 19" and 19° 14' 56" North and 72° 55' 50" and 73° 00' 32" East have an area of 127 km^2 [2,14]. The population of Thane city is 1890000 according to the 2011 census and ranked 15th most populated city in India.

The population of Thane city increases due to industrialization, urbanization and city connecting to Mumbai. Thane city has roadside drains and minor nallas (streams) discharging stormwater into major nallas or directly into creek. On 26th July 2005 in Thane created unpredictable situation due to extreme rainfall coinciding with the highest tide level [16]. Due to urbanization and city situated near to creek experiencing flood risk, especially at heavy rainfall, high tide. Now every year the trend of flooding in Thane city is increasing. The minor flooding problem is water entering the basement of few buildings for short duration and major problem is flooding the area for several days. It leads to relocation of population, damage to infrastructure services and risk of epidemics [16]. Hence, considering the city's importance and risk of flooding, knowledge of proper rainfall intensity is necessary.

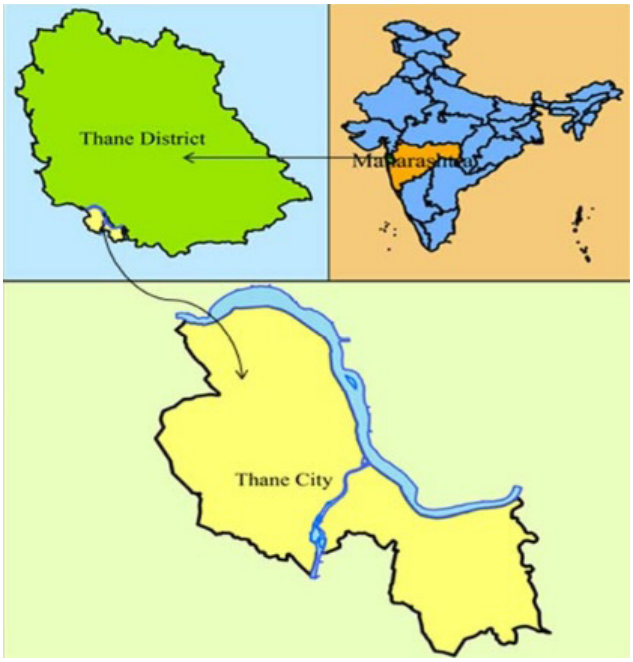

Figure 1. Location map of Thane City, India.

Source: [15].

3. Data Used in the Analysis

Collected continuously observed hourly rainfall data from 1969 to 2018 for Santacruz rain gauge station from India Meteorological Department (IMD). Thane Municipal Corporation (TMC) helped to collect rainfall data.

4. Methodology

Firstly, the IDF curve was constructed by Ram Babu's equation, Kothyari and Garde's equation and then Gumbel EV-I distribution equation by using hourly rainfall data from 1969 to 2018. Each IDF curve constructed was compared for a return period of 5 years return period and then an appropriate method for projection was selected based on the results of rainfall intensity and previous studies. Secondly, 50 years of hourly rainfall data were divided into 5 subgroups and IDF curves were developed for each subgroup according to the chosen method. After that, the projected rainfall intensity for different duration and different return periods was found for the next 30 years using linear regression model. The rainfall IDF relationships are found using the method described below.

4.1 IDF Curves by Ram Babu Equation

Ram Babu in 1979 studied the available data from 42 rain gauge stations across India and then after analyzing

the rainfall data came up with the IDF formula and nomographs [9]. The general form of IDF equation written as,

$$I = \frac{KT^a}{(t+b)^n} \quad (1)$$

where, I is the rainfall intensity (cm/hr.), T is the return period (years), t is the storm duration (hours) and K, a, b & n are constants depending on geographical location developed for 42 rain gauge stations. Thane city area comes under western zone. The values of K, a, b and n are taken as 7.787, 0.2087, 0.5 and 0.8908 respectively for analysis of rainfall [17].

4.2 IDF Curves by Kothyari and Garde's Equation

Kothyari and Garde studied 80 rain gauge stations across India in 1992 with data available at that time and then provided an empirical equation [10]. The empirical equation developed for the Indian zones is as follows:

$$i_t^T = c\frac{T^{0.20}}{t^{0.71}}\left(R_{24}^2\right)^{0.33} \quad (2)$$

where, i_t^T=maximum rainfall intensity (mm/hr.) for T years return period and t hour duration, C=constant depends on Geographical zones of India proposed by them are given in Table 1 and R_{24}^2= depth of precipitation for 2 years returns period 24-hour duration (mm). From Figure 2, Thane city comes in western zone, the value of C taken as 8.3 for analysis of rainfall.

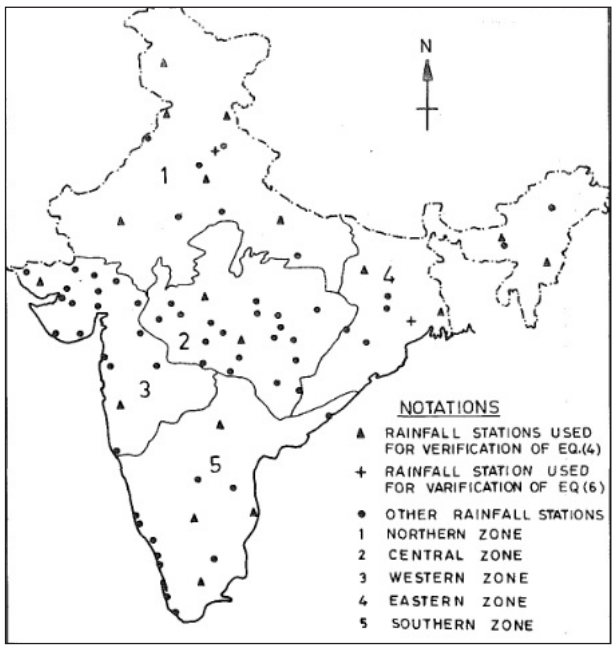

Figure 2. Location of rain gauge stations and zonal boundaries in India.

Source: [10].

Table 1. C values for geographical zones of India.

Zones	Zones in Figure 1	Value of C
North Zone	1	8
East Zone	4	9.1
Center Zone	2	7.7
West Zone	3	8.3
South Zone	5	7.1

Source: [10]

4.3 IDF Curves by Gumbel Extreme Value Type-I Distribution (EV-I) Method

Gumbel's EV-I distribution method is mainly used for short duration rainfall data analysis [17]. Also, Gumbel's EV-I method is used for flood analysis. This method is comparatively simple and used to calculate maximum rainfall depth [11]. Zope studied rainfall data from 1969 to 2008 for the Santa Cruz rain gauge station and in 2012 developed a rainfall IDF relationship using Gumbel's EV-I method [12].

In this method, the hourly observed rainfall data were used to compute the maximum rainfall depth (X) and the statistical variables, (arithmetic mean and standard deviation) for each duration (1, 2, …., 24 hours) [11]. Frequency of precipitation X_T (in mm) for each duration having the specified return period T (year) is given by Equation (4) as below [18].

$$x_T = \bar{x} + ks \quad (3)$$

where, $\bar{X}$ is the mean, S is the standard deviation and k is the Gumbel's Frequency factor for return period T.

Frequency factor is calculated for all the selected return periods based on selected distribution. Gumbel's frequency factor is given by the following equation:

$$k = \left(\frac{\sqrt{6}}{\pi}\right)\left\{0.577^2 + ln\left[1n\left(\frac{T}{T-1}\right)\right]\right\} \quad (4)$$

4.4 Linear Regression Method

Linear regression method is used for predicting future values based on previous values. This method is mostly used for climate prediction, business and many more [19]. The linear regression has the relationship between the dependent variable and another changing variable known as the independent variable. The linear regression is calculated by following equation [20].

$$Y = A + BX \quad (5)$$

Here, Y = Dependent variable;
X = Independent variable;
A, B = Regression parameters.

5. Results and Discussion

5.1 Comparisons of IDF Relationships

In the present study, some empirical relationships were used to derive IDF curves, especially for the Indian region by Indian researchers. From Equation (1), the rainfall intensity was determined for different durations and different return periods. Accordingly, the developed IDF curve by Ram Babu equation is shown in Figure 3. From Equation (2), the rainfall intensity is defined using the value of R (mean annual rainfall) for different durations and different return periods. The developed IDF curves by Kothyari & Garde's equation for the Santacruz rain gauge station are shown in Figure 4. From Equation (3), the rainfall intensity is determined for the different duration and for different return periods and developed IDF curves by Gumbel's EV-I method is shown in Figure 5. Similarly, comparing the IDF curves for 5-year return periods using different methods was shown in Figure 6. The results obtained indicate that the rainfall intensity for 1-hour duration is 55.23 mm/hr. according to Rambabu's equation while it is 64.8 mm/hr. according to Kothyari and Garde's equation and 74.8 mm based on the observed data by Gumbel's EV-I method. Hence, as time progresses more and more information is available and empirical relationships may change or used constant may change for the various regions. From above results, the rainfall intensities estimated by Gumbel's EV-I method are higher for the same duration and same return period than the Rambabu's and Kothyari & Garde's empirical equation. Goel and his associates concluded in 2007 that Gumbel's EV-I approach was most commonly utilized for analyzing short duration rainfall data [17]. Zope and his associates evaluated rainfall for the same Santacruz rain gauge station in 2012 and determined that the Gumbel EV-I approach would be suitable for analyzing short-duration rainfall data [12]. So, in present study Gumbel's EV-I method was selected for projected rainfall IDF relationships analysis.

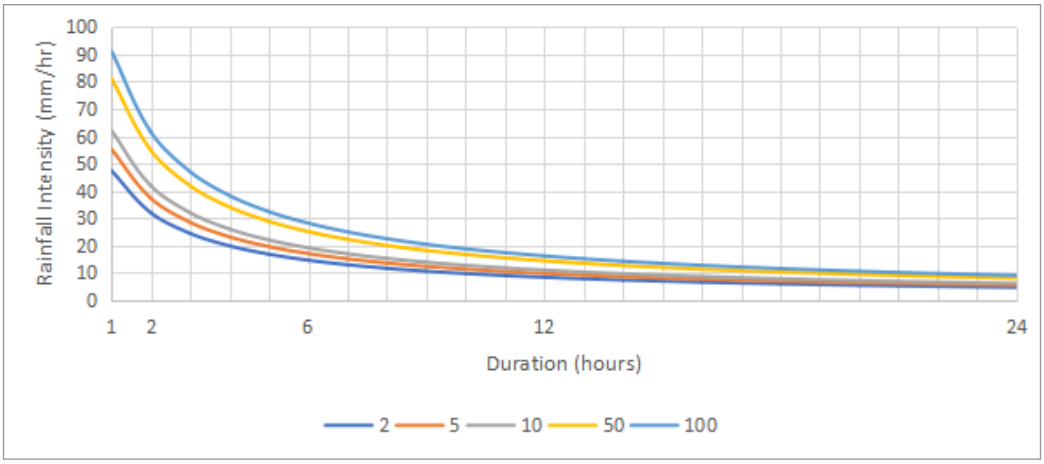

Figure 3. IDF curves by Ram Babu's equation.

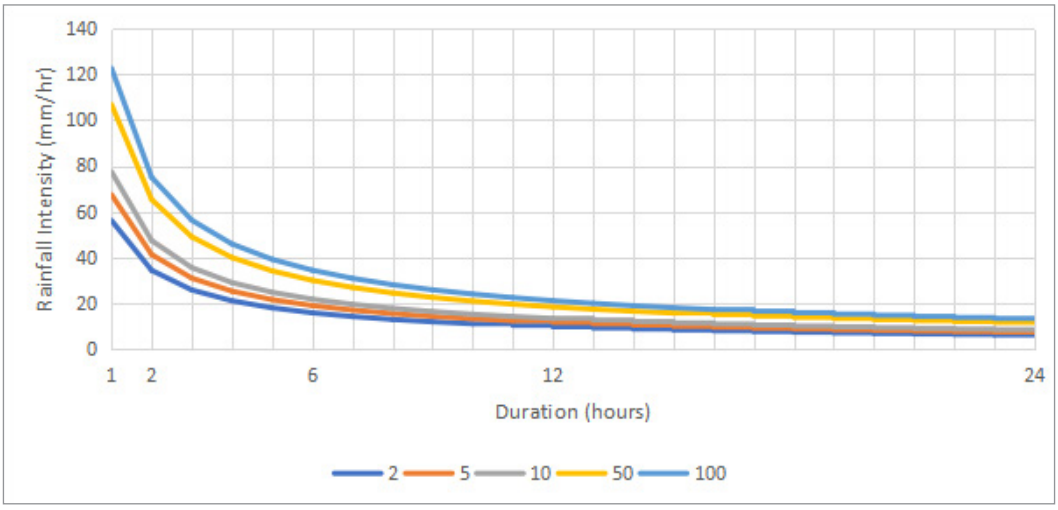

Figure 4. IDF curves by Kothyari & Garde's equation.

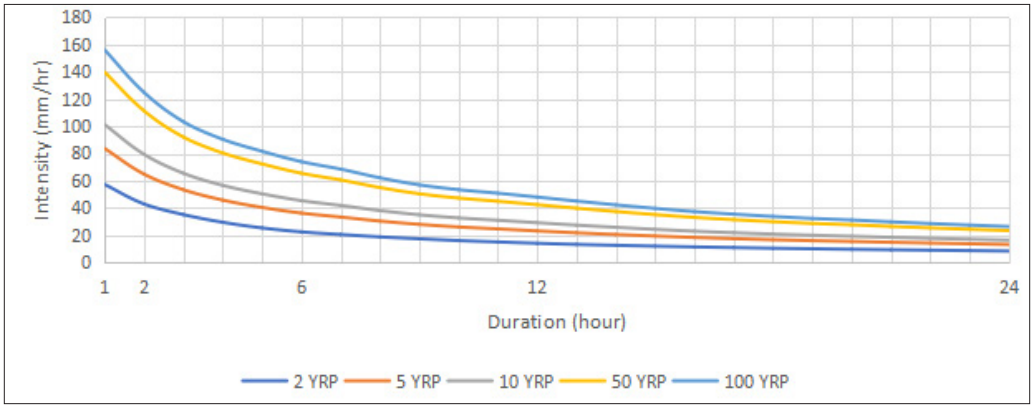

Figure 5. IDF curves by Gumbel's EV-I method.

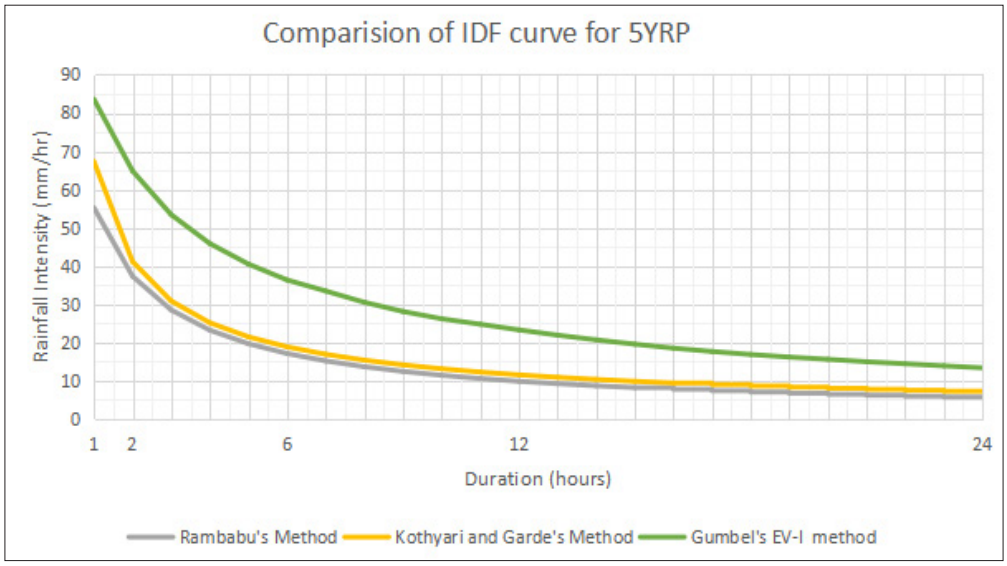

Figure 6. Comparisons IDF curves for 5 years return period.

5.2 Projecting IDF Relationships for Next 30 Years

Central Public Health & Environmental Engineering Organization (CPHEEO) guidelines recommend 30-year life expectancy for urban infrastructure [21]. Therefore, the estimated IDF relationship developed in the present study is limited to the next 30 years.

The updated IDF relationships must include in new storm water system and in existing storm water system as design criteria [13]. For rainfall intensity projection, 50 years of rainfall data were divided into 5 subgroups of 10-year periods and then the corresponding IDF relationship was developed for each sub-group period by Gumbel's EV-I method. The rainfall IDF relationships for each sub-group are shown in Table 2, Table 3, Table 4, Table 5 and Table 6 respectively.

The rainfall intensities for each sub-group period

Table 2. IDF relationships for sub-group period 1969 to 1978.

Period	Duration (hour)	Rainfall Intensity (mm/hr.)				
		2	5	10	50	100
1969-1978	1	52.79	68.57	79.05	102.06	111.80
	2	37.69	48.43	55.56	71.22	77.85
	6	19.95	25.50	29.18	37.27	40.70
	12	13.57	18.05	21.02	27.54	30.31
	24	8.45	11.43	13.40	17.73	19.56

Table 3. IDF relationships for sub-group period 1979 to 1988.

Period	Duration (hour)	Rainfall Intensity (mm/hr.)				
		2	5	10	50	100
1979-1988	1	48.38	57.48	63.52	76.78	82.40
	2	36.37	43.21	47.75	57.72	61.94
	6	19.53	22.38	24.27	28.42	30.18
	12	11.92	14.41	16.07	19.71	21.25
	24	7.75	9.18	10.13	12.21	13.09

Table 4. IDF relationships for sub-group period 1989 to 1998.

Period	Duration (hour)	Rainfall Intensity (mm/hr.)				
		2	5	10	50	100
1989-1998	1	71.53	103.50	124.72	171.32	191.05
	2	60.43	88.34	106.86	147.53	164.76
	6	28.44	40.76	48.93	66.88	74.48
	12	15.71	22.24	26.57	36.08	40.11
	24	9.10	12.03	13.97	18.24	20.04

Table 5. IDF relationships for sub-group period 1999 to 2008.

Period	Duration (hour)	Rainfall Intensity (mm/hr.)				
		2	5	10	50	100
1999-2008	1	64.91	103.40	128.95	185.05	208.81
	2	45.07	75.43	95.57	139.81	158.55
	6	27.28	52.00	68.40	104.42	119.67
	12	18.20	34.91	46.00	70.36	80.67
	24	10.30	19.28	24.24	38.33	43.87

Table 6. IDF relationships for sub-group period 2009 to 2018.

Period	Duration (hour)	Rainfall Intensity (mm/hr.)				
		2	5	10	50	100
2009-2018	1	50.97	71.53	85.18	115.16	127.85
	2	38.90	55.77	66.96	91.55	101.96
	6	19.93	28.77	34.64	47.53	52.98
	12	13.05	19.22	23.32	32.32	36.14
	24	7.64	11.12	13.44	18.51	20.66

for the 1-hour duration with different return periods are shown in Table 7. Each sub-group for the same location, for the same duration and same return period gets different intensities of rainfall. Hence, there is non-stationarity in the IDF relationships, and relationships cannot be held fix. Therefore, the linear regression method is used to access changing trend in rainfall intensity.

In this method, the 1-hour time rainfall intensity for the same return period from each sub-group is plotted. Then, using a linear regression model, the changing trend in rainfall intensity was estimated for different return periods. Linear regression equation obtained for 2 years, 5 years, 10 years, 50 years and 100 years return period are shown in Figure 7, Figure 8, Figure 9, Figure 10 and Figure 11 respectively can be used to calculate rainfall intensities for the next 30 years of each sub-group period (2019 to 2028), (2029 to 2038) and (2039 to 2048) for the same duration and same return period.

Table 7. Sub-groupwise rainfall intensity for return period.

Sub-group Period	Rainfall Intensity (mm/hr.)				
	2	**5**	**10**	**50**	**100**
1969 - 1978	52.79	68.57	79.05	102.06	111.80
1979 - 1988	48.38	57.48	63.52	76.78	82.40
1989 - 1998	71.53	103.50	124.72	171.32	191.05
1999 - 2008	64.91	103.40	128.95	185.05	208.81
2009 - 2018	50.97	71.53	85.18	115.16	127.85

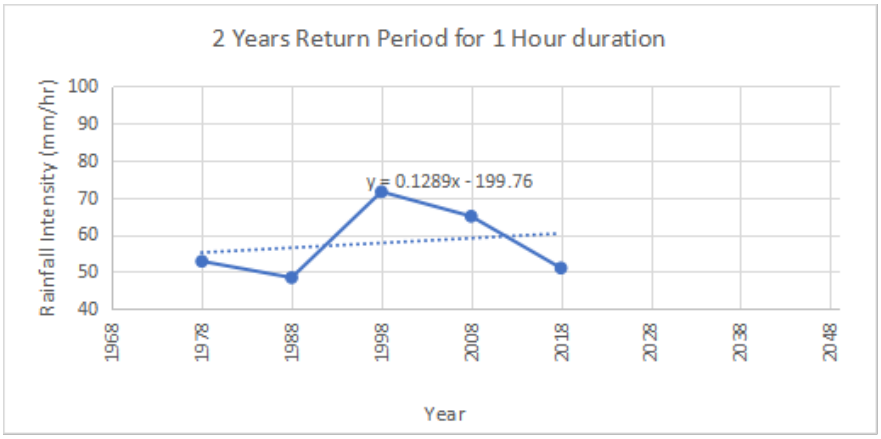

Figure 7. Linear equation for 2-year return period.

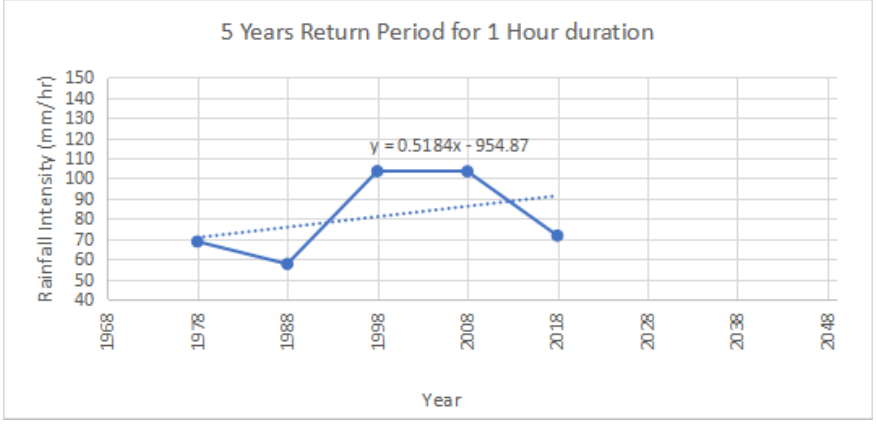

Figure 8. Linear equation for 5-year return period

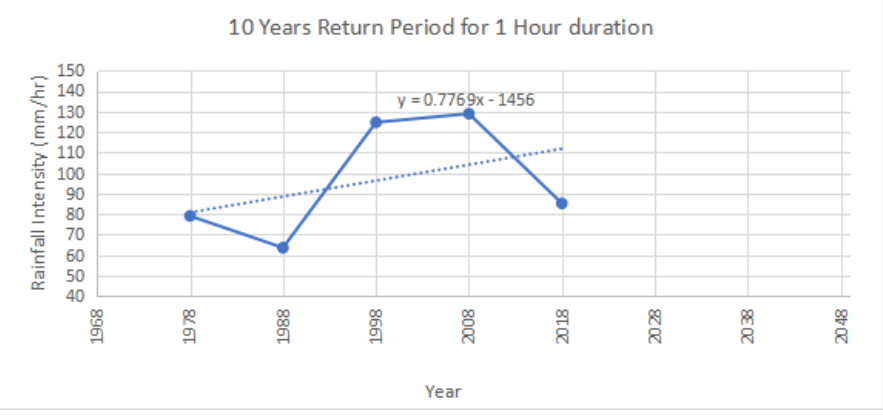

Figure 9. Linear equation for 10-year return period.

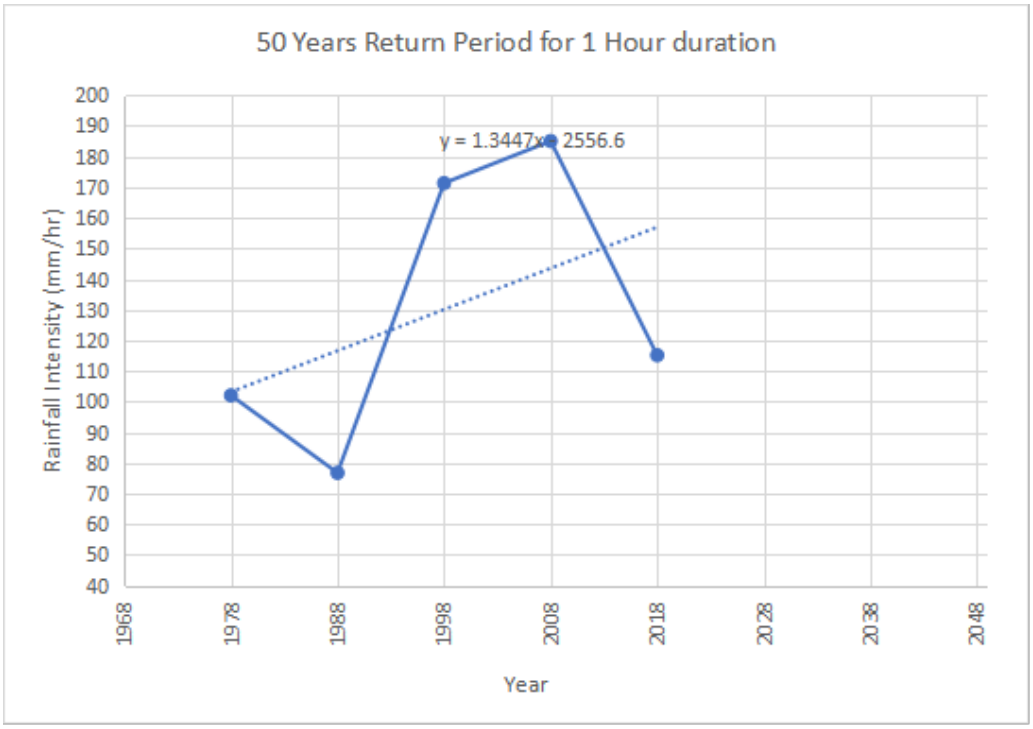

Figure 10. Linear equation for 50-year return period.

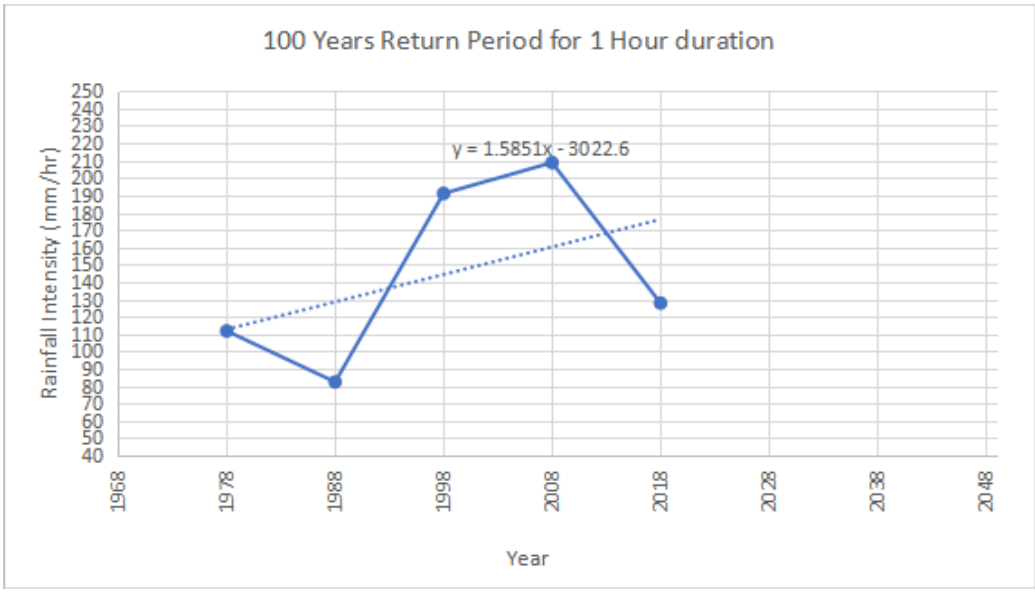

Figure 11. Linear equation for 100-year return period.

Rainfall intensities for predicted future are estimated by obtained linear equation each sub-group period (2019 to 2028), (2029 to 2038) and (2039 to 2048) are shown in Table 8, From Table 8 the result of this analysis indicates that the changing trend of rainfall intensity for the various durations and different return periods are likely to increase over time: 17% in (2019 to 2028), 25% in (2029 to 2038), and 32% in (2039 to 2048) with respect to Gumbel's EV-I method Rainfall IDF relationships. Similarly, results indicate that, for each projected sub-group period the defined average changing trend of rainfall intensity compared to the IDF relationship predicted by Gumbel's EV-I method will be the same for all duration and all return periods. Hence, projected IDF curve for the next 30 years is shown in Figure 12.

Table 8. Trend of increase projected rainfall intensities relationships.

Sub-group Period	Rainfall Intensity (mm/hr.)					Increase trend of rainfall intensity (%)					Average Increase Trend (%)
	2	5	10	50	100	2	5	10	50	100	
1969 - 2018	57.3	83.6	101.1	139.5	155.7						
2019 - 2028	61.6	96.3	119.6	170.5	192	1.08	1.15	1.18	1.22	1.23	**1.17**
2029 - 2038	62.9	101.5	127.3	183.9	207.8	1.10	1.21	1.26	1.32	1.33	**1.25**
2039 - 2048	64.2	106.7	135.1	197.3	223.7	1.12	1.28	1.34	1.42	1.44	**1.32**

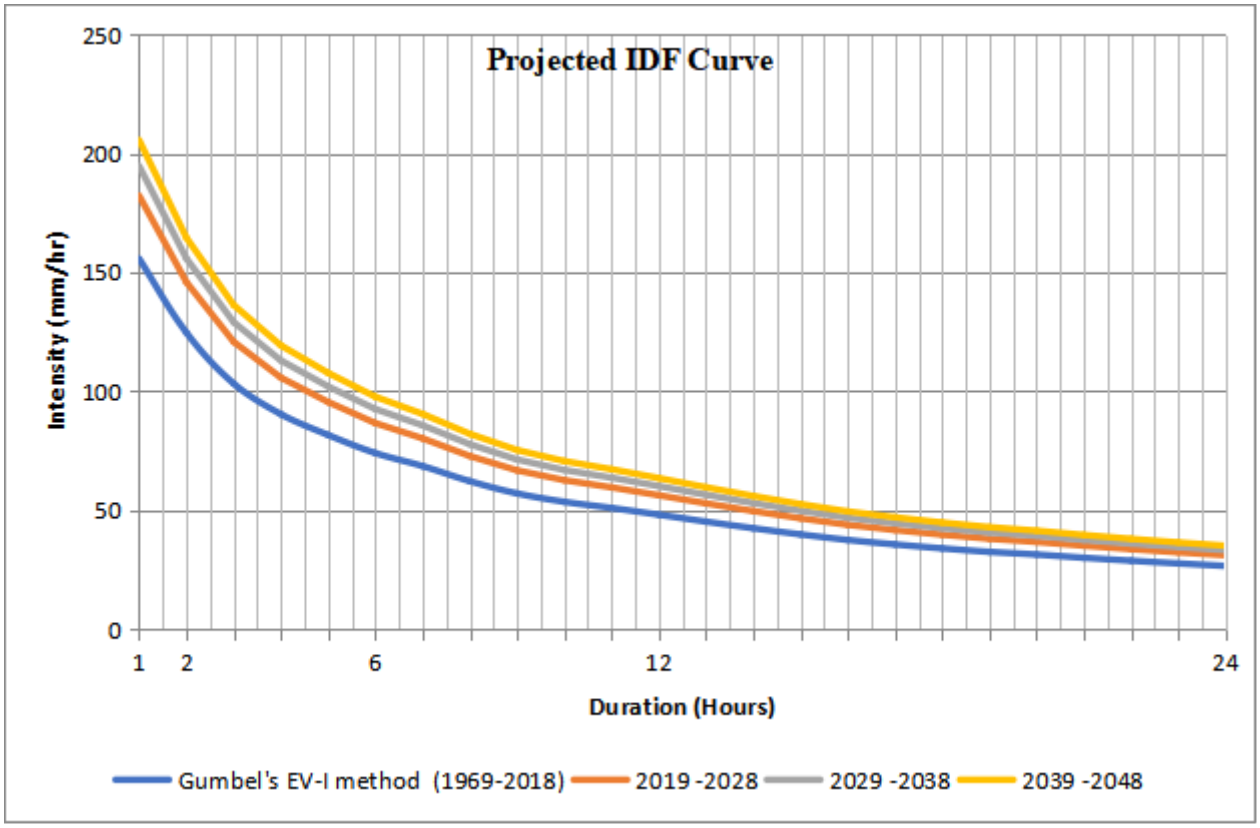

Figure 12. Projected IDF curves for 100 years return period.

In a drainage system, the storm return period is determined using risk analyses and economic evaluations (probability of damage, loss of life, etc., in case of failure) [22]. A significantly longer return time is used to build minor dams and airport drains (100 years and above), where there is a significant risk of life in case of failure, but a 2 or 5-year return period is used to construct urban roadside drains where the cost of failure is small.

Rainfall intensity for a return period of 100 years is shown by the IDF curve produced by Gumbel's EV-I method to be 155.7 mm/h. However, the July 2005 rainfall record for Thane indicates an intensity of 190 mm/hr. Therefore, the projected rainfall IDF curve would have a rainfall intensity of 223.7 mm/hr. during the coming 30 years (2019-2048) with a return period of 100 years. Which displays favorable outcomes in comparison to earlier Thane city rainfall records. In light of the changing hydrologic conditions witnessed on July 26th, 2005 in Thane, comparing the results with projected IDF curves reveals better outcomes.

6. Conclusions

Climate change is likely to increase the risk of flooding in cities with an increase in extreme rainfall events. Storm water planning requires an IDF relationship with climate change impacts. The result indicates that, as time progresses more and more information available and empirical relationships may change or used constant may change for the various regions. Even today Thane city still uses IDF relationships developed based on the empirical equa-

tion, even increases the evidence of heavy rainfall events and repetitive waterlogging in the city. The suggested mechanism for developing IDF relationship incorporating climate change in the present study can be helpful in new storm water design and in improving the existing drainage system. Additionally, IDF curves must be adjusted on a regular basis in order to take climate change's effects on rainfall and the resulting changes in design discharge into account. The technique used to estimate the changing trend of rainfall intensity gives good results in climate change conditions and shows the higher intensities of rainfall indicate the design would be safer to avoid flooding in the future.

Conflict of Interest

Authors declare no conflict of interests.

Acknowledgment

The authors are thanking the staff of Thane Municipal Corporation and IMD Pune for providing data related for this research.

References

[1] Shahapure, S.S., Eldho, T.I., Rao, E.P., 2011. Flood simulation in an urban catchment of Navi Mumbai City with detention pond and tidal effect using FEM, GIS, and remote sensing. Journal of Waterway, Port, Costal, Ocean Engineering. 137(6), 286-299. DOI: https://doi.org/10.1061/(ASCE)0733-9429(1983)109:12(1603)

[2] Chacko, R., Kulkarni, A.T., Eldho, T.I., 2012. Urban coastal flood inundation modelling: A case study of Thane City, India. ISH Journal of Hydraulic Engineering. 18(3), 194-203. DOI: https://doi.org/10.1080/09715010.2012.721187

[3] Zope, P.E., Eldho, T.I., Jothiprakash, V., 2016. Development of rainfall intensity duration frequency curves for Mumbai City, India. Journal of Water Resource and Protection. 8, 756-765. DOI: http://dx.doi.org/10.4236/jwarp.2016.87061

[4] Dourte, D., Shukla, S., Singh, P., et al., 2013. Rainfall intensity-duration-frequency relationships for Andhra Pradesh, India: Changing rainfall patterns and implications for runoff and groundwater recharge. Journal of Hydrologic Engineering. 18(3), 324-330. DOI: https://doi.org/10.1061/(ASCE)HE.1943-5584.0000625

[5] Chawathe, S.D., Fadanvis, S.S., Goel, V.V., 1977. Rainfall analysis for the design of storm sewers in Bombay. The Institution of Engineers (India) Journal-EN. 58, 14-20.

[6] Chin, D.A., 2019. Relative performance of intensity-duration-frequency function. Journal of Hydrologic Engineering. 24(4), 04019006. DOI: https://doi.org/10.1061/(ASCE)HE.1943-5584.0001767

[7] Bell, F.C., 1969. Generalized rainfall-duration-frequency relationships. Journal of Hydraulic Division. 95, 311-327.

[8] Chen, C.L., 1983. Rainfall intensity-duration-frequency formulas. Journal of Hydraulic Engineering. 109, 1603-1621. DOI: https://doi.org/10.1061/(ASCE)0733-9429(1992)118:2(323)

[9] Babu, R., Tejwani, K.K., Agrawal, M.C., et al., 1979. Rainfall intensity-duration-return periodequations and nomographs of India, Dehradun: CSWCRTI, ICAR.

[10] Kothyari, U.C., Garde, R.J., 1992. Rainfall intensity-duration-frequency formula for India. Journal of Hydraulic Engineering. 118, 323-336. DOI: https://doi.org/10.1061/(ASCE)0733-9429(1992)118:2(323)

[11] Al-anazi, K.K., El-Sebaie, I.H., 2013. Development of intensity-duration-frequency relationships for Abha city in Saudi Arabia. International Journal of Computational Engineering Research. 3(10), 58-65.

[12] Zope, P.E., Eldho, T.I., Jothiprakash, V., 2012. Study of spatio-temporal varaitions of rainfall pattern in Mumbai City, India. Journal of Environmental Research and Development. 6(3), 545-553.

[13] Yiping, G., 2006. Updating rainfall IDF relationships to maintain urban drainage design standards. Journal of Hydrologic Engineering. 11, 506-509. DOI: https://doi.org/10.1061/(ASCE)1084-0699(2006)11:5(506)

[14] CDP, 2005. City Development Plan of Thane Municipal Corporation.

[15] Waghmare, J.S., 2017. GIS for urban air & noise pollution mapping - A Case study of Thane City, India. Population & Environment Bulletin. 13(4). Available from: https://iipsindia.ac.in/sites/default/files/project_report/Volume-13-No-4-2017.pdf

[16] Hariyali Team, 2006. Project report on repetitive water logging in Thane city: Engineering solutions and Environmental management plan. I & II.

[17] Goel, N.K., Sarkar, S., 2007. Regional rainfall intensity-duration-frequency relationship. NTPC Sponsored Training Course on Design Flood Analyses for Hydropower Projects, 2007 Aug 20-25, IIT Roorkee.

[18] Ibrahim, E.H., 2011. Developing rainfall intensi-

ty-duration-frequency relationship for two regions in Saudi Arabia. Journal of King Saud University-Engineering Science. 24, 131-140.
DOI: https://doi.org/10.1016/j.jksues.2011.06.001

[19] Sreehari, E., Ghantasala, P., 2019. Climate changes prediction using simple linear regression. Journal of Computational and Theoretical Nanoscience. 16, 1-4.
DOI: https://doi.org/10.1166/jctn.2019.7785

[20] Jain, S.K., Kumar, V., 2012. Trend analysis of rainfall and temperature data for India. Current Science. 102(1), 37-49.

[21] CPHEEO, 2019. Manual of Storm Water Drainage System, New Delhi: Government of India [Internet]. Available from: http://cpheeo.gov.in/cms/manual-on-storm-water-drainage-systems---2019.php

[22] Mirhosseini, G., Srivastava, P., Stefanova, L., 2013. The impact of climate change on rainfall Intensity-Duration-Frequency (IDF) curves in Alabama. Regional Environmental Change. 13, 25-33.
DOI: https://doi.org/10.1007/s10113-012-0375-5

BILINGUAL
PUBLISHING CO.
Pioneer of Global Academics Since 1984

Tel.:+65 65881289
E-mail: contact@bilpublishing.com
Website:ojs.bilpublishing.com

2661-3190
02
9 772661 319227